ISSN 0352-9045

Informacije MIDEM

Journal of Microelectronics,
Electronic Components and Materials
Vol. 52, No. 3(2022), September 20022

Revija za mikroelektroniko,
elektronske sestavne dele in materiale
letnik 52, številka 2(2022), September 2022

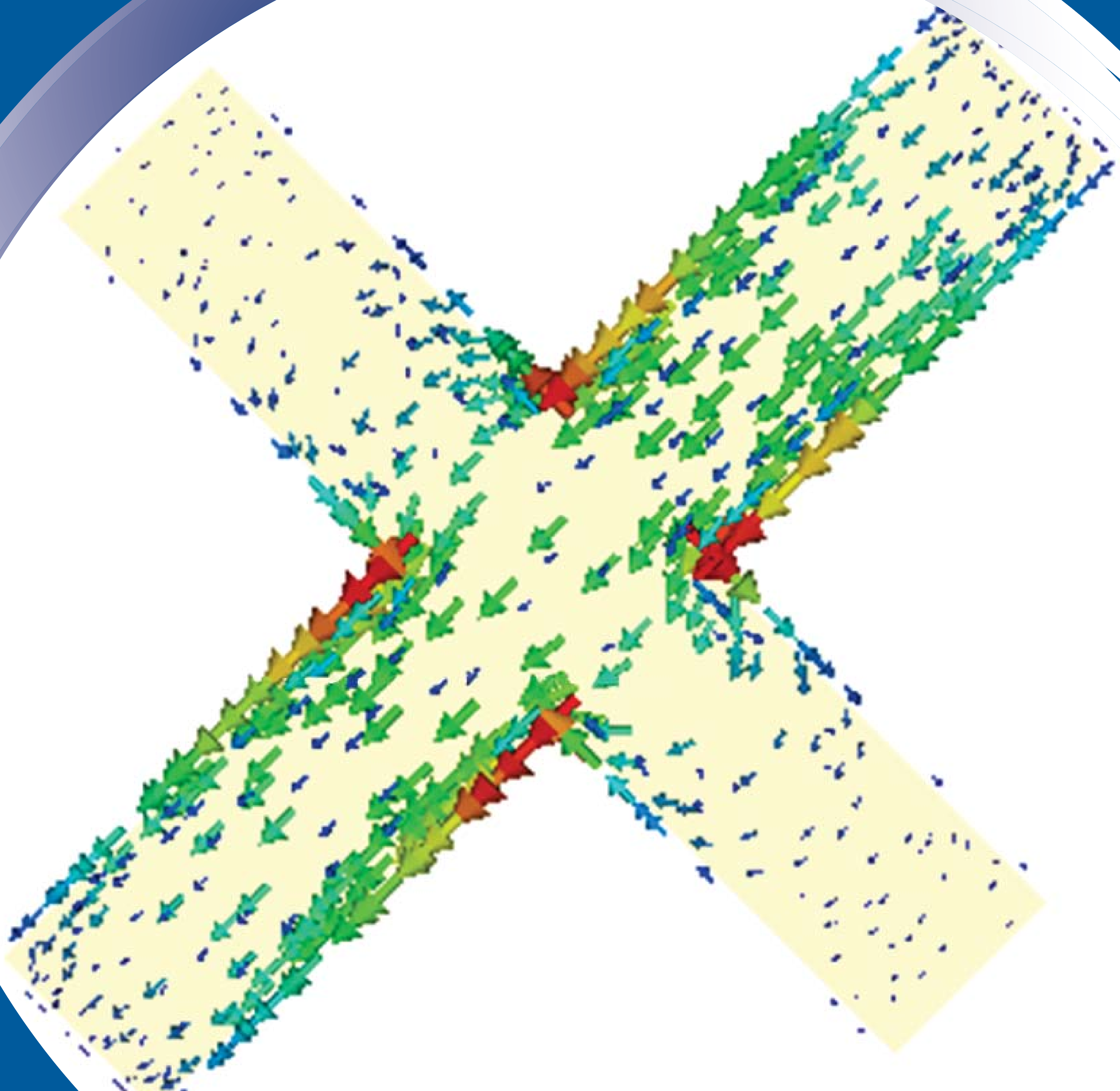

UDK 621.3:(53+54+621+66)(05)(497.1)=00 ISSN 0352-9045

Informacije MIDEM *3-2022*

Journal of Microelectronics, Electronic Components and Materials

VOLUME 52, NO. 3(183), LJUBLJANA, SEPTEMBER 2022 | LETNIK 52, NO. 3(183), LJUBLJANA, SEPTEMBER 2022

Published quarterly (March, June, September, December) by Society for Microelectronics, Electronic Components and Materials - MIDEM. Copyright © 2022. All rights reserved. | Revija izhaja trimesečno (marec, junij, september, december). Izdaja Strokovno društvo za mikroelektroniko, elektronske sestavne dele in materiale – Društvo MIDEM. Copyright © 2022. Vse pravice pridržane.

Headquarters | Naslov uredništva
Uredništvo Informacije MIDEM
MIDEM pri MIKROIKS
Stegne 11, 1521 Ljubljana, Slovenia
T. +386 (0)1 513 37 68
F. + 386 (0)1 513 37 71
E. info@midem-drustvo.si
www.midem-drustvo.si

Annual subscription rate is 160 EUR, separate issue is 40 EUR. MIDEM members and Society sponsors receive current issues for free. Scientific Council for Technical Sciences of Slovenian Research Agency has recognized Informacije MIDEM as scientific Journal for microelectronics, electronic components and materials. Publishing of the Journal is cofinanced by Slovenian Research Agency and by Society sponsors. Scientific and professional papers published in the journal are indexed and abstracted in COBISS and INSPEC databases. The Journal is indexed by ISI® for Sci Search®, Research Alert® and Material Science Citation Index™. |
Letna naročnina je 160 EUR, cena posamezne številke pa 40 EUR. Člani in sponzorji MIDEM prejemajo posamezne številke brezplačno. Znanstveni svet za tehnične vede je podal pozitivno mnenje o reviji kot znanstveno-strokovni reviji za mikroelektroniko, elektronske sestavne dele in materiale. Izdajo revije sofinancirajo ARRS in sponzorji društva. Znanstveno-strokovne prispevke objavljene v Informacijah MIDEM zajemamo v podatkovne baze COBISS in INSPEC. Prispevke iz revije zajema ISI® v naslednje svoje produkte: Sci Search®, Research Alert® in Materials Science Citation Index™.

Design | Oblikovanje: Snežana Madić Lešnik; Printed by | tisk: Biro M, Ljubljana; Circulation | Naklada: 1000 issues | izvodov; Slovenia Taxe Percue | Poštnina plačana pri pošti 1102 Ljubljana

Content | Vsebina

Original scientific paper

https://doi.org/10.33180/InfMIDEM2022.301

Informacije MIDEM
Journal of Microelectronics,
Electronic Components and Materials
Vol. 52, No. 3(2022), 147 – 157

Water Pollution Level Detection using Patch Antenna Measurements at Microwave Frequencies

Sobha Uday A[1], *Swaroop Sahoo*[2], *Steffy Benny*[2]

[1]*Department of Electronics and Communication Engineering, Central University of Karnataka, Kalaburagi, Karnataka, India*
[2]*Department of Electrical Engineering, Indian Institute of Technology Palakkad (IIT Palakkad), Kerala, India*

Abstract: This work aims at demonstrating a new technique of determining the pollution levels in water by detecting the change in resonant frequency of simple patch antenna while immersed in water (distilled and solutions). The technique is based on the principle that resonance frequency of patch antenna is dependent on the effective dielectric constant of microstrip substrate and the surrounding fluid. An antenna immersed in water has a different resonance frequency than that in air because of the change in effective dielectric constant. Similarly, antenna immersed in salt solutions has a different resonance frequency than that of distilled water. A rectangular patch antenna resonating at 7.65 GHz is designed and operated in air, water and different salt solutions of varying concentration. The resonance frequency shift magnitude is 0.1 to 1 GHz for NaCl solution of 1 to 4 N. However, the resonance frequency shift magnitude for ferric nitrate, potassium chloride, potassium nitrate solutions are 0.5 to 2 GHz for concentration range 0.1 to 1 N. In addition, the frequency shift for acetone mixed with water in proportion of 5 to 25% is determined to in the range 1.3 - 1.5 GHz. Similar studies are performed with antenna immersed in water collected from various sources in Kerala, India. A complimentary theoretical study has been performed to determine the dielectric constant of water with different concentrations of sodium chloride. The calculated values have been used in a simulation software to simulate the shift in resonant frequency when an antenna is immersed in water.

Keywords: microwave; antenna; pollution; dielectric constant; water

Zaznavanje ravni onesnaženosti vode s pomočjo meritev s krpičasto anteno na mikrovalovnih frekvencah

Izvleček: amen tega dela je prikazati novo tehniko določanja stopnje onesnaženosti vode z zaznavanjem spremembe resonančne frekvence preproste krpičaste antene, ko je potopljena v vodo (destilirano in raztopine). Tehnika temelji na načelu, da je resonančna frekvenca krpičaste antene odvisna od efektivne dielektrične konstante mikropasovne podlage in okoliške tekočine. Antena, potopljena v vodo, ima zaradi spremembe efektivne dielektrične konstante drugačno resonančno frekvenco kot antena v zraku. Podobno ima antena, potopljena v raztopino soli, drugačno resonančno frekvenco kot antena v destilirani vodi. Pravokotna krpičasta antena, ki resonira pri frekvenci 7,65 GHz, je zasnovana in deluje v zraku, vodi in različnih raztopinah soli z različno koncentracijo. Premik resonančne frekvence za raztopino NaCl od 1 do 4 N je 0,1 do 1 GHz. Premik resonančne frekvence za raztopine železovega nitrata, kalijevega klorida in kalijevega nitrata je od 0,5 do 2 GHz za koncentracije od 0,1 do 1 N. Poleg tega je frekvenčni premik za aceton, pomešan z vodo v razmerju 5 do 25 %, določen v območju 1,3 do 1,5 GHz. Podobne študije so opravljene z anteno, potopljeno v vodo, zbrano iz različnih virov v Kerali v Indiji. Izvedena je bila dopolnilna teoretična študija za določitev dielektrične konstante vode z različnimi koncentracijami natrijevega klorida. Izračunane vrednosti so bile uporabljene v simulacijski programski opremi za simulacijo premika resonančne frekvence, ko je antena potopljena v vodo.

Ključne besede: mikrovalovi; antena; onesnaženje; dielektrična konstanta; voda

---

** Corresponding Author's e-mail: swaroop@iitpkd.ac.in*

How to cite:
S. Uday et al., "Water Pollution Level Detection using Patch Antenna Measurements at Microwave Frequencies", Inf. Midem-J. Microelectron. Electron. Compon. Mater., Vol. 52, No. 3(2022), pp. 147–157

1 Introduction

Among the various types of environmental pollutions, air pollution and water pollution are the most dangerous types. Pollution of water and air make them a health hazard even though they are imperative for life. Water pollution primarily leads to various diseases like cholera, diarrhoea, dysentery, hepatitis A, typhoid, and polio as per reports by the World Health Organization (WHO) [1]. The main types of water pollutants are inorganic, organic and biological [2]. Organic and inorganic pollutants are usually byproducts (that have been released into the river) from factories. Organic pollutants are alcoholic, ketonic, amino compounds while inorganic pollutants are sulphates, chlorides, carbonates, etc [3]. On the other hand, biological pollutants develop due to the decay of various types of plants, algae, dead animals etc. in water. The guideline concentrations for some chemicals in water are given in Table 1 [4].

Table 1: Sample guideline concentrations as per WHO of chemical substances in water

Substance	Guideline concentration (mg/l)
Acrylamide	0.0005
Alachlor	0.1
Aldicarb	0.01
Aldrin and dieldrin	0.00003
Aluminum	0.9
Antimony	0.02
Arsenic	0.01
Nitrates	50
Benzene	0.01
Sodium	50
Vinyl chloride	0.0003

It can be observed from table 1 that the guideline concentrations of chemicals in water are primarily less than 0.1 mg/l. Thus, even small amounts of contaminants in water are harmful to human beings and should be easily detectable. Thus, it is necessary that the methods of determining contamination levels are cost effective, easily deployable, sensitive and accessible for all.

The established methods of determining pollution levels are UV-Vis measurements, mass spectrometry and electrochemical sensors like ion-sensitive electrodes sensors [5]. UV-Vis spectrometry works on the principle of determining the intensity of light absorbed by the polluted water sample in comparison to the intensity of light absorbed by a reference sample. The process of determining light absorbed by reference sample and calibration are necessary. This technique is prone to difficulties because all pollutants in water may not absorb light of wavelengths in the range of 190-850 nm [5]. Mass spectrometry involves the conversion of molecules to ions and determination of the mass-to-charge ratio (m/z) in a sample. The accurate measurement of the molecular weight of constituents in sample makes this multistep process very complicated [6].

Heavy metals can be detected using multiple electrode techniques. The electrode interacts with the water sample producing an electrical signal which can be detected based on amperometric, voltammetric, and potentiometric method [5][7][8]. However, these electrodes have to be fabricated using very complex process to maintain their sensitivity.

Along with the above-mentioned detection techniques various kinds of sensors are also used for detection of pollutants. Primary sensor for detecting pollution are fibretics sensors, lab-on-chip sensors [9], biosensors and EM sensors [7][10]. Among the above-mentioned sensors, electrochemical sensors using solid state devices are better suited for use in wireless network. In addition to that, polymer lab chip-based systems involve the integration of the sample preparation, reaction and measurement on a small chip that reduces the time taken for pollutant detection in a conventional lab. However, various performance parameters related to the minimum quantity that can be detected, reaction and response time depend on the sensor fabrication methods and kind of sensors [11][12].

Microwave sensors have already been used for determination of pollutants presence in water. However, Korostynska et. al., used interdigitated electrodes (IDE) for microwave detection for detection of pollutants [Olga 13]. The IDE sensor was used to measure the change in S_{11} parameter i.e., reflection coefficient to monitor water quality on a real-time basis. It was clearly observed that the S_{11} of the IDE changed when operated in air, deionized water, tap water as well as other pollutants like CuCl, KCl and $MnCl_2$.

In addition to the above-mentioned measurement of changes in chemical and physical properties, dielectric constant variation of water at microwave frequencies is also another property that can be used for detection of presence of pollutants and their quantification. The determination of complex dielectric constant of water with various ionic compounds/solutes has been initially done in 1947 by J. B. Hasted et. al., using waveguide technology at three different microwave frequencies [14]. Lawrence A. Klein et. al., (1977), worked on an advanced permittivity model for sea water that is valid at L and S-band [15]. Further to this research work, Hans J. Liebe et. al. (1991), worked on determining a complex dielectric constant model for water based on Debye's and double Debye's equation [16] that is valid upto 1 THz.

U. Raveendranath et. al. (1995), worked on estimating the contamination level in water at microwave frequencies by measuring complex dielectric constant of polluted water in the microwave frequency band using a waveguide cavity [3]. For this work the water sample is filled in a capillary tube which is then put inside a waveguide cavity. The dielectric constant measurements are performed based on the variation in Q-factor and resonant frequency.

Ahmad H Abdelgwad et. al. (2014), worked on the use of microwave measurements for estimation of pollution levels in water present in underground pipelines [17]. The estimation is based on the comparison of dielectric constant of pure and the polluted water. This technique is based on modelling done by Cole-Cole model [18]. It can be easily observed that microwave measurement techniques have been used for determination of dielectric constant of water, mix of water and salts, mix of water and soil as well as water with various contaminants.

The novelty of this work is to determine the feasibility of using microstrip antennas (either rectangular or of various layouts) for detection of pollutants and their level in polluted water. This is because microstrip antennas are easy to fabricate and are really cheap due to which this method would be a good complementary technique along with the above mentioned sensor based systems. This study involves determining the shift in resonant frequency of a microstrip patch antenna that is immersed in water with different chemicals of varying concentrations. This change in concentration, modify the dielectric constant of water which in turn changes the resonant frequency of patch antenna. The resonant frequency is determined by measuring S_{11} parameter or reflection coefficient of antenna. The resonance frequency shift is different for different salt solutions and also varies with quantity of salt dissolved in water.

In addition, this study involves the theoretical analysis of variation in complex dielectric constant of water with change in frequency as well as concentration of NaCl. This theoretical study has been discussed in Section 2 where the Debye model-based variation of dielectric constant (with change in microwave frequency) of distilled water, water mixed with sodium chloride (NaCl) has been used. Next the design and electrical characteristics of the simple antenna used in this study are also discussed in Section 3. Section 4 presents the relationship between resonant frequency and dielectric constant of water. Section 5 discusses the details of the experimental results involving various salts solutions and shift in the resonant frequency of antenna when dipped in these salt solutions and acetone. The salts used are NaCl, potassium chloride, ferric nitrate and potassium nitrate. The change in the complex permittivity for the artificially prepared contaminated water can be used for determining the impact of the pollutants on permittivity of water which in turn affects the resonant frequency of antennas. This section also gives a detailed analysis of the measurements. The conclusions are given in Section 6.

2 Theory of dielectric constant of distilled water and water mixed with solute

For this analysis it is very important to be able to theoretically determine the dielectric constant behavior of water with change in frequency from 1-10 GHz. Therefore, the initial part of the study involves the theoretical understanding and simulation of the variation of dielectric constant of water and NaCl solution in the microwave frequency range of 1-10 GHz. The Debye relaxation model for dielectric and Debye model for water with NaCl are discussed here along with the results of simulations [12][13].

2.1 Debye relaxation model

Debye relaxation model is used in this study to simulate the dielectric constant of water for a range of frequencies and is called the first order Debye model [19]:

$$\varepsilon = \varepsilon_{high} + \frac{\varepsilon_{st} - \varepsilon_{high}}{1 + j\omega\tau} \tag{1}$$

where, ε_{st} represents the static dielectric constant at static frequency and ε_{high} represents the infinite frequency dielectric constant. The real and imaginary parts of the dielectric constant can be written as equation (2):

$$\varepsilon' + j\varepsilon'' = \left(\varepsilon_{high} + \frac{\varepsilon_{st} - \varepsilon_{high}}{1 + (\omega\tau)^2}\right) + j\left(\frac{\varepsilon_{st} - \varepsilon_{high}}{1 + (\omega\tau)^2}\omega\tau + \frac{\sigma_s}{\varepsilon_0}\right) \tag{2}$$

Where σ_s is the static conductivity, the relaxation time τ is related to the relaxation frequency f_c by equation (3):

$$f_c = \frac{1}{2\pi\tau} \tag{3}$$

The impact of static conductivity i.e., σ_s has to be included in the Debye model because of the movement of group of ions as a result of regular electric field. The above model is the basic model used for simulating the dielectric constant variation at microwave frequencies. The static dielectric constant of water is 80.1. The dielectric constant of distilled water is simulated in the frequency range of 1 to 10 GHz and the results are shown in Figure 1. The permittivity of water decreases from 78.1 at 1 GHz to 60 at 10 GHz. Thus, the dielectric constant of water is seen to follow a non-linear trend of decreasing from 1 to 4 GHz and then a linear trend from 4 to 10 GHz.

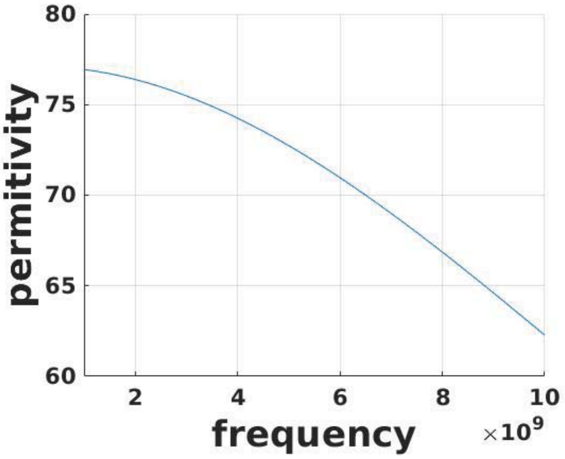

Figure 1: Dielectric constant of distilled water with frequency

2.2 Dielectric constant variation due to change in NaCl concentration and temperature

The analysis in the previous sub-section does not consider variation in the amount of solute and temperature. It has to be noted that dissolving solute in water as well as temperature variation of water result in significant change in the dielectric constant of water. To determine the dielectric constant and dielectric loss of NaCl solution, modified Debye's equation has to be used [19][20]. The variables that depend on change in concentration of solute and temperature are static dielectric constant, ε_{st} and relaxation time τ while the dielectric constant at high frequency ε_{high} is a constant value of 4.9. The equations for ε_s and τ are given by (4) and (5)

$$\varepsilon_{st}(T,N) = \varepsilon_{st}(T,0)\,a(N) \tag{4}$$

$$2\pi\tau(T,N) = 2\pi\tau(T,0)\,b(N,T) \tag{5}$$

where T is water temperature in °C ranging $0 \le T \le 40$ and N is normality of the solution ranging $0 \le N \le 4$. The terms *a(N)* and *b(N, T)* are given by (6) and (7)

$$a(N) = 1.02551N + 5.151\times10^{-2}N^2 - 6.889\times10^{-3}N^3 \tag{6}$$

$$\begin{gathered} b(N,T) = 0.1463\times10^{-2}NT\times1.000 - 0.04896 - \\ - 002967N^2 + 5.644\times10^{-3}N^3 \end{gathered} \tag{7}$$

The expression for ε_S *(T, N)* is given below in equation (8)

$$\begin{gathered} \varepsilon_{st}(T,0) = 87.74 - 0.40008T + 9.398\times \\ \times\,10^{-4}T^2 + 1.410\times10^{-6}T^3 \end{gathered} \tag{8}$$

Relaxation time is determined by using equation (9)

$$\begin{gathered} 2\pi\tau(T,0) = 1.1109\times10^{-1} - 3.824\times10^{-12}T + \\ + 6.938\times10^{-14}T^2 - 5.096\times10^{-16}T^3 \end{gathered} \tag{9}$$

The ionic conductivity of NaCl solution is given by equation (10)

$$\begin{gathered} \sigma_{NaCl} = N\big[10.394 - 2.3776N + 0.68258N^2 - \\ -0.13538N^3 + 1.0086\times10^{-2}N^4\big] \end{gathered} \tag{10}$$

The temperature T is assumed to be 25°C in all the above equations. The equations (4) to (10) are used along with equations (1-3) to compute dielectric constant and loss of NaCl solution. The parameters such as ε_{high}, ε_{St}, τ and σ_{NaCl} are obtained by varying the normality of the solution from 0 N to 4 N and the calculated parameters ε_s and τ are given in Table 2. The parameters in Table 2, are used for further calculation of dielectric constant and loss variation with frequency as shown in Figure 2 and Figure 3.

The relative permittivity of the NaCl solution is observed to decrease from 77 to 28 for 1 GHz as the NaCl concentration is increased from 0 to 4 N. Similarly, as the concentration of the NaCl in the solution increases from 0 to 4 N the relative permittivity decreases from 67 to 25 at 7 GHz. Thus, there is a significant variation in dielectric constant for small change in concentration of NaCl. The frequency dependency can be observed from Figure 2 where it can be noted that dielectric constant decreases at the rate of 5/5 GHz for concentration 0 N while it reduces at the rate of 5/10 GHz for concentration 4 N.

Table 2: Debye's parameters for NaCl Solution

Normality	ε_S	τ(ps)	σ
0	78.3474	8.0994	0
1	61.8569	7.8045	8.5737
2	50.1994	7.3032	14.8949
3	40.1364	6.8699	19.6984
4	28.4295	6.7788	22.8903

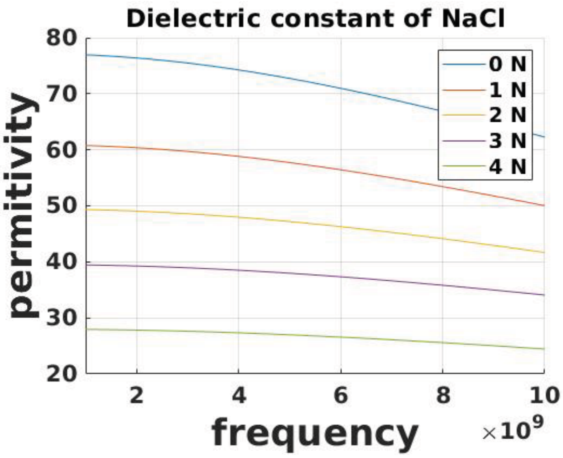

Figure 2: Dielectric constant of NaCl solution for various concentration of NaCl

From Figure 3 it can be observed that the dielectric loss for NaCl solution increases from 80 to 205 at 1 GHz as the concentration of NaCl in the solution increases from 1 N to 4 N. It can also be observed that the dielectric loss is inversely proportional to frequency. However, the rate of decrease reduces as the NaCl concentration is reduced from 4 N to 1 N. For NaCl concentration at 1 N the permittivity decreases from 80 at 1 GHz to 40 at 10 GHz while the dielectric loss reduces from 200 at 1 GHz to 50 at 10 GHz. This is because in the Debye's equation for dielectric loss the first term is dependent on frequency while the second term is independent of frequency.

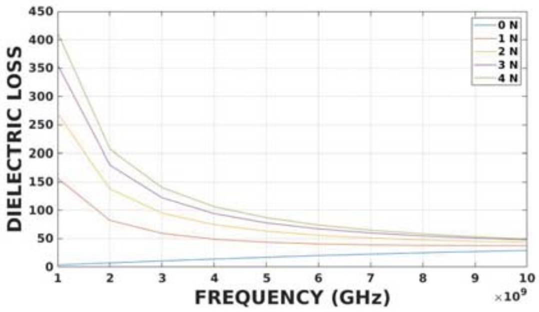

Figure 3: Dielectric loss of NaCl solution

3 Antenna design and measurements

As discussed in Section 1 the sensor for this study is a microstrip patch antenna that operates at 5.3 GHz and 7.5 GHz i.e., it resonated at frequencies of 5.3 and 7.5 GHz. This has been designed using FR4 substrate having permittivity of 4.4 based on theory given in Balanis, 2005 [21] using High Frequency Structure Simulator (HFSS) [22] and is shown in Figure 4. The resonant frequency is determined based on s_{11} parameters shown in Figure 5. The design parameters are given in Table 3. The design layout and the simulation of S_{11} parameter of the antenna are given in Figure 4 and Figure 5, respectively.

Table 3: Design parameters for rectangular patch antenna in air

Frequency (f)	7.5 GHz
Substrate thickness (h)	1.6 cm
Substrate dielectric constant (ε_r)	4.4
Patch width (W)	2.15 cm
Effective dielectric constant of the substrate (ε_{eff})	3.48
Patch length (L)	1.74 cm
Feed inset (y_0)	4.1 cm
Feedline width (w)	2 cm

The reflection coefficient of the antenna (S_{11}) is given by Figure 5 and is approximately -27.5 dB at 7.65 GHz, respectively.

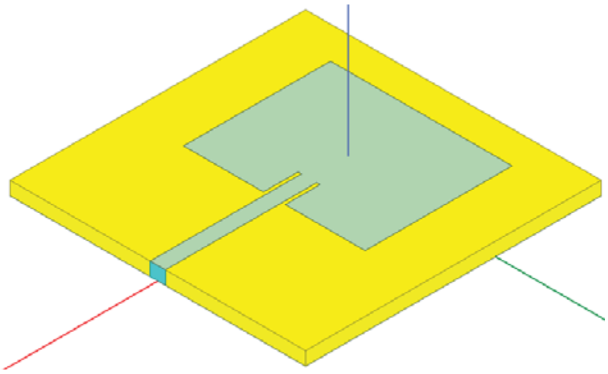

Figure 4: Antenna design

The antenna fabricated using the design is depicted in Figure 6 and shows the top view along with 50 ohm SMA connector. The antenna has been tested using

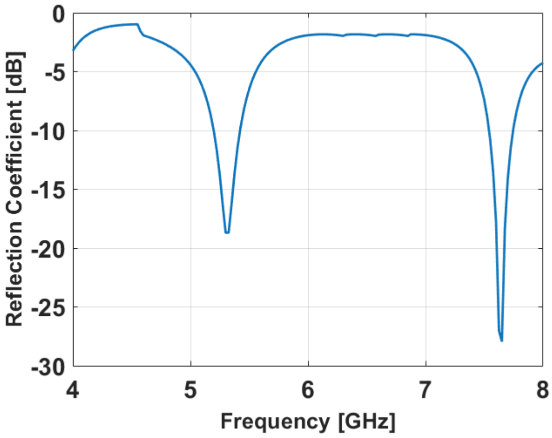

Figure 5: Reflection Coefficient (S11) of designed patch antenna

RHODE & SCHWARZ ZNB8 vector network analyzer (VNA) that can be calibrated and operated from 100 MHz to 8 GHz.

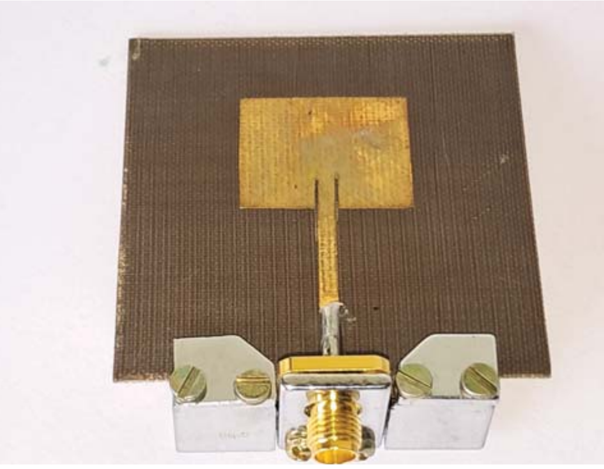

Figure 6: Fabricated antenna

The S_{11} parameter for the antenna is measured using VNA and is shown in Figure 10. It shows that the S_{11} parameter has a dip of -5 dB at 4.8 GHz while there is a dip of -18 dB at 7.65 GHz. The resonant frequency at 7.65 GHz matches well for both the simulation and measurement while the dip at 5.3 GHz has shifted to 4.8 GHz. This is because the simulations were performed without the SMA connector.

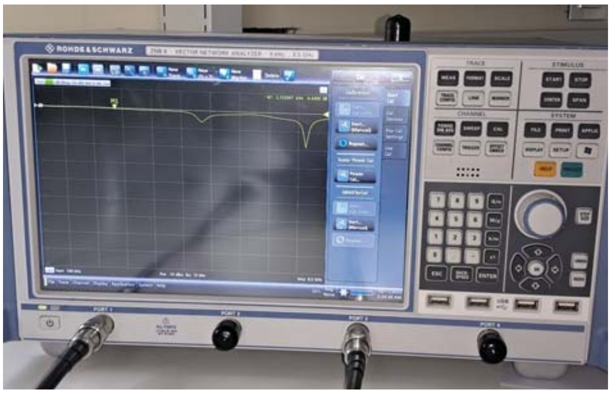

Figure 7: Testing of fabricated patch antenna

4 Resonance frequency and dielectric constant

As already discussed in Section 1 the shift in the resonance frequency of antenna due to immersion in water is used as the technique for pollution level estimation. Therefore, a mathematical method has been used to study the impact of variation of effective dielectric constant of antenna on its resonance frequency when immersed in water. The resonance frequency and effective dielectric constant are related as in equation (11) [15].

$$f_0 = \frac{c}{\sqrt{\varepsilon_{eff}}\, l_{eff}} \tag{11}$$

where f_0 is the resonant frequency, l_{eff} is the effective length and ε_{eff} is the effective dielectric constant. Effective dielectric constant is a function of the dielectric constant of the substrate used for the antenna and the dielectric constant of the environment in which the antenna is supposed to be operating i.e., $\varepsilon_{eff} = f(\varepsilon_r, \varepsilon_{dielectric})$. For the measurement, the microstrip patch antenna is immersed in water sample that in turn results in the interaction of the near field of the antenna with the medium. Thus, the electrical characteristics of the antenna change with respect to the dielectric constant of the material. This results in shifting of the resonant frequency. A polynomial relating shifted resonant frequency and effective dielectric constant was determined. The following process is followed to determine the polynomial:

Based on equation (11), the shifted resonant frequency is used to determine the effective dielectric constant.

From the obtained results, a graph has been plotted using MATLAB curve fit tool to determine a relation between the effective dielectric constant and frequency shift.

The polynomial relation of resonant frequency and the ε_{eff} is given by equation (12)

$$f_0 = p_1\varepsilon_{eff}^3 + p_2\varepsilon_{eff}^2 + p_3\varepsilon_{eff} + p_4 \tag{12}$$

where f_0 is the measured resonant frequency shift when the antenna is immersed in water of varying dielectric constant and the coefficients p_1 = - 3.802 e-5, p_2 = 0.00566, p_3 = - 0.2699 and p_4 = 5.283 which are obtained after the curve fit. The results are shown in Figure 8.

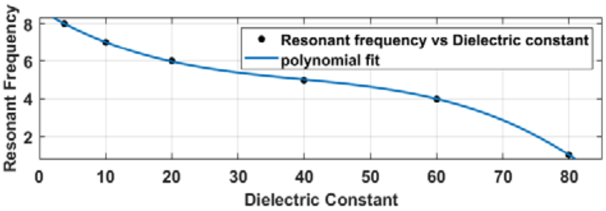

Figure 8: Resonance frequency vs dielectric constant

Thus, if the dielectric constant is in the range of 20-50 the resonant frequency will be in the range of 4-6 GHz.

5 Experiment for resonant frequency measurement and verification

The resonance frequency of antenna in water or solutions of salts is determined for various salts and for acetone. The detailed explanations of the experiment are given in the sub-sections.

5.1 Various salts

The resonance frequency of antenna is determined by dipping the antenna in solutions of sodium chloride, potassium chloride, ferric nitrate and potassium nitrate. Similarly, the measurement of resonant frequency of antenna with change in concentration of salt which in turn results in change of dielectric constant of water is explained here. The experimental setup is shown in Figure 9, which includes the designed patch antenna, water sample to be tested and a vector network analyzer (VNA). The VNA has been used to measure the reflection coefficient for the frequency range of 4 GHz to 8 GHz when the antenna is immersed in the water samples.

5.1.1 Sodium chloride

Solutions of NaCl and water with concentration varying from 1 N to 3 N have been prepared and the antenna has been immersed in water. The S_{11} parameter has been measured for distilled water as well as solution of each normality and the results are shown in Figure 10. For this work the resonant frequency in air at 7.65 GHz has been taken as the reference and its shift with change in dielectric constant is used for the analysis.

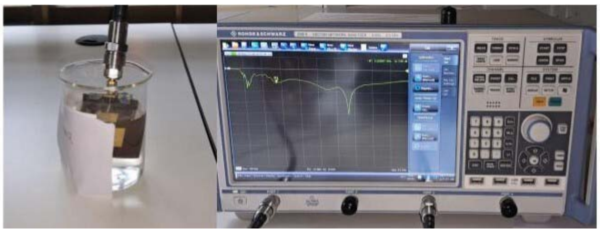

Figure 9: Measurement of dielectric constant using designed patch antenna

It can be observed from Figure 10 that the resonant frequency at 7.65 GHz shifts to the left (reduces) as the dielectric constant changes due to the increase in NaCl concentration. The NaCl solution with 1N concentration has a resonance frequency of approximately 7.2 GHz while the solutions with concentration 2N and 3N have resonance frequency at 7.1 and 6.9 GHz. Thus, there is a clear reduction in the resonant frequency of 7.65 GHz.

To verify these results, a simulation study has been performed in HFSS where the model of the antenna is simulated and is immersed in water and the S_{11} parameter values have been determined for distilled water and water with NaCl with proportion of 1-4 N as shown in Figure 11.

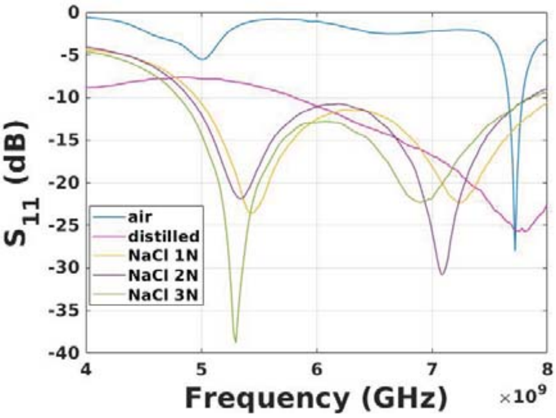

Figure 10: S_{11} parameters for antenna in air and water with various levels of NaCl

However, the simulations showed sensitivity to just the distilled water and NaCl solution with normality 3 N due to which other normality value S_{11} are not presented in this result. By comparing the simulation and measurement results it is very clear that the S_{11} parameters match very well for distilled water and NaCl solution with normality 3 N. It can be observed that the resonance dip is at 7.55 GHz for distilled water for the measurements and the simulation. In addition, it can also be observed that the dip corresponding to 5.2 GHz is not present in the simulations.

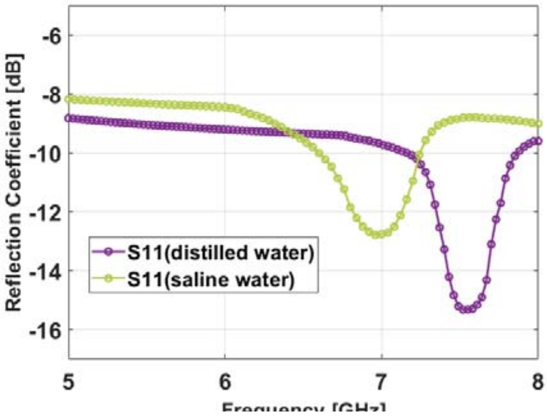

Figure 11: S11 parameters for antenna in air and water with various levels of NaCl

To conduct an in-depth study, the shift in resonance frequency for NaCl solutions is represented as a frequency shift magnitude i.e., the difference between the resonance frequency in air and in water samples. The resonant frequency shift magnitude for various concentrations have been determined and have been presented in Figure 12. The frequency shift magnitude is in the range of 0.4 to 0.9 GHz for the NaCl concentration range of 1-4 N. It can be observed that there is a linear relationship between the NaCl concentration 1-4 N and frequency shift magnitude. The impact of salt concentration on the resonant frequency shift magnitude is studied further where the concentration is varied from 0.1 to 1 N for some of the salts considered in this study. The frequency shift magnitude is from 0.1 to 0.4 GHz for the given concentration range as shown in Figure 13.

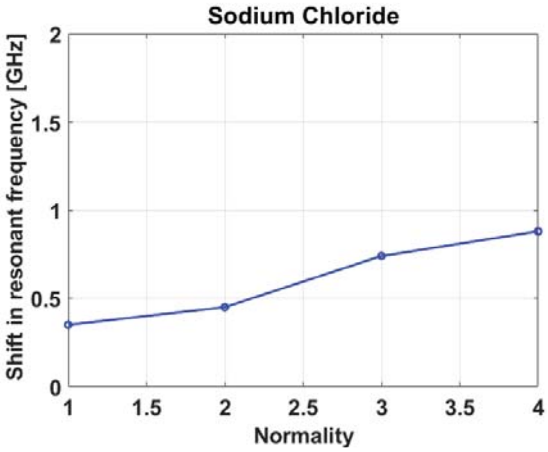

Figure 12: Resonant frequency shift magnitude for NaCl solution of normality 1-4 N

5.1.2 Ferric nitrate, potassium chloride, potassium nitrate

In addition to NaCl solution, the resonance frequency shift magnitude experiments were repeated for various other salt solutions. Solutions used for the testing were made using ferric nitrate, potassium chloride and potassium nitrate with normalities of 0.1, 0.25, 0.6 and 1 N. The resonance frequency was again observed to shift to a lower frequency. The frequency shift magnitude with the change in salt concentration is shown in Figure 13. It can be observed that the values of the frequency shifts are in the range of 1.8 to 1.9 GHz for potassium chloride, 1.4 to 1.7 GHz for potassium nitrate and 0.8 to 1.6 GHz for ferric nitrate.

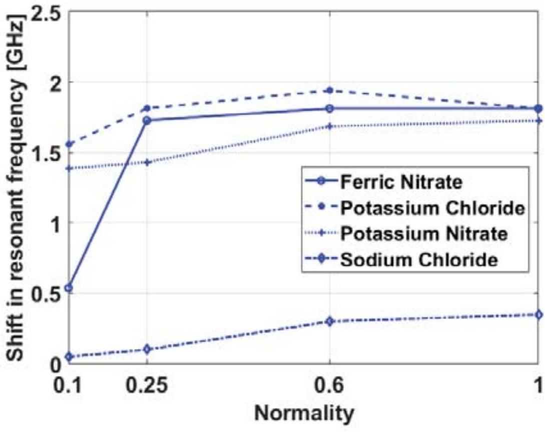

Figure 13: Resonant frequency shift for ferric nitrate, potassium nitrate and potassium chloride for normality 0.1 to 1 N

It can also be observed that the frequency shift magnitude increases as the salt concentration increases. However, it has to be noted that the resonant frequency shift magnitude in NaCl, potassium nitrate and potassium chloride solutions are almost linear in the 0.1 to 1 N range but the shift magnitude for ferric nitrate is slightly non-linear. An important analysis is the repeatability of the shifted resonance frequency for multiple measurements using the same antenna for same solutions. For this analysis the mean (shown in red) and standard deviation (shown in blue) of the resonance frequency shift magnitude are shown in Figure 14. It can be observed that the mean values of the frequency shifts magnitude are in the range of 1.8 to 2 GHz for potassium chloride, 1.4 to 1.7 GHz for potassium nitrate and 0.8 to 1.6 GHz for ferric nitrate. The standard deviation of the frequency shift is in the range of 0.1 to 0.4 GHz. The trend followed by the mean value of the frequency shift magnitude are same as that of the measurements shown in Figure 13.

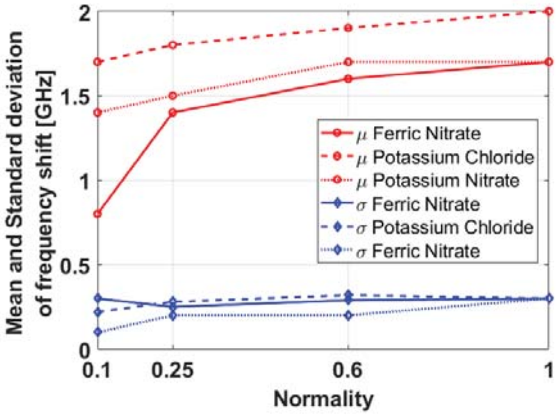

Figure 14: Resonant frequency shift mean (red) and standard deviation (blue) for like ferric nitrate, potassium nitrate and potassium chloride of normality 0.1 to 1 N

There are various observations from these measurements. The frequency shift magnitude increases with increase in salt concentration. The frequency shift magnitude is least for NaCl in this study while it is highest for potassium chloride. Thus, the sensitivity of simple patch antenna resonance frequency is highest for potassium chloride and least for NaCl. All these observations show that this rectangular patch antenna resonance frequency is sensitive to changes in salt concentration as well as to certain type of salts. Some salts have more impact on the antenna resonance frequency shift magnitude than others. Thus, the antenna is very sensitive to small quantities of those salt and can be used for detection of very small amounts of the salt. Therefore, a new design has to be tried to check sensitivity for various salts and chemicals.

5.2 Acetone

The resonant frequency shift analysis was also performed for acetone concentration in terms of volume percentage being varied from 5% to 20% with a step size of 5% to observe the shift in resonant frequency. 5% acetone shows a resonance frequency of 6.3 GHz while 25% acetone shows resonance frequency of 6.1 GHz. From the Figure 15 it can be observed that the frequency shift is not that significant but the magnitude of the reflection coefficient is varying to a great extent. The reflection coefficient is below -10 dB for frequency range from 5.7 to 7 GHz for all concentrations of acetone. The shift in the 10% acetone water mix is not shown over here because the shifted S_{11} response overlaps with the 15% response. The observations in Figure 15 show that the antenna is not very sensitive to changes in concentration of acetone. This is shown from the minimal shift in the resonant frequency with change in concentration from 5 to 25%. Thus, this antenna is not very suitable for detection of very small variation in acetone.

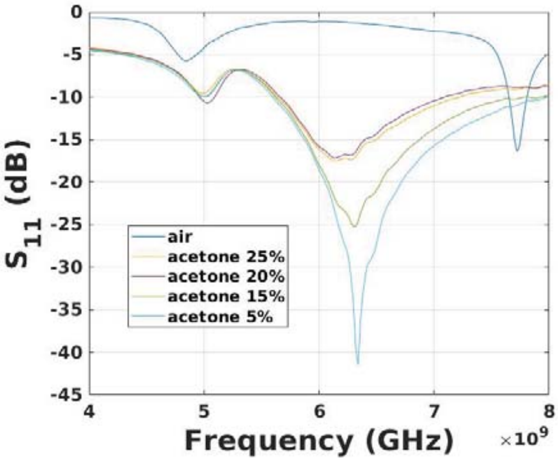

Figure 15: Resonant frequency shift for acetone solution with concentration varying from 5% to 25%

5.3 Resonant frequency shifts due to water from various sources

Implementation and testing of this proposed research technique on actual water samples can provide a lot of practical information on the operational implementation. Therefore, to test the effectiveness of this antenna-based measurement technique, water samples have been collected around IIT Palakkad from various water sources. The water sources i.e., wells and ponds are located as per the map shown in Figure 16. The top figure shows map of the general area from where water samples have been collected. The map also shows the location of IIT Palakkad in the bottom left corner. The location of two of the wells are shown by the blue dots in the bottom two figures of Figure 16. The water samples thus collected have been tested to check the resonant frequency shift magnitude based on S_{11} parameter measurements when antenna was immersed in water. S_{11} parameter measurements in Figure 17 show that the resonant frequency of antenna in water from pond and well4 is approximately 7.3 and 7.4 GHz while the resonant frequency for well3 and well2 is 6.2 and 5.8 GHz, respectively.

A chemical analysis using UV-Vis spectrometer was also performed to determine the level of pollutants in the water sources. The measurements based on the spectrum showed the presence of fluorides. It was observed that level of fluorides was more in well2 and well3 which showed the most shifted resonant frequency at 6.2 and 5.8 GHz.

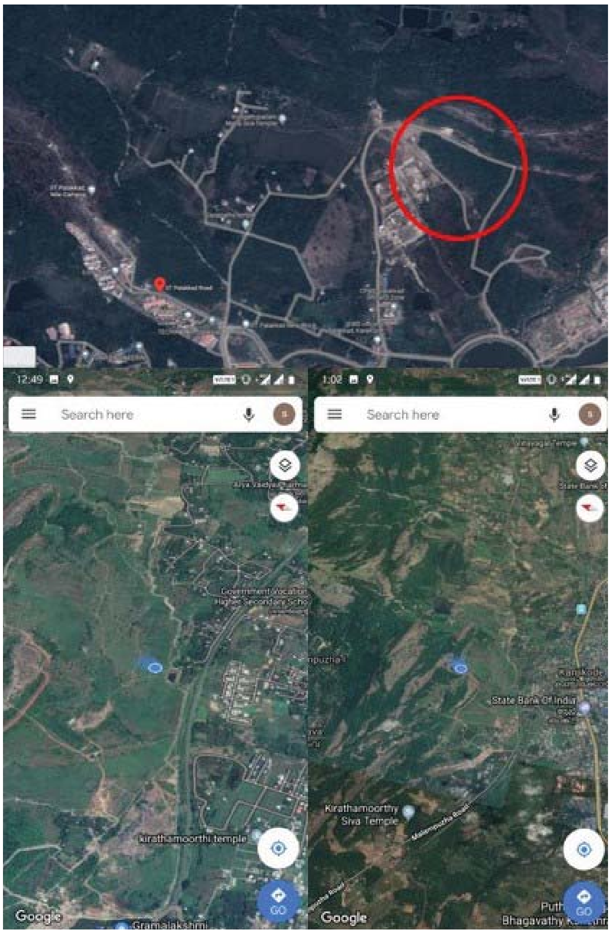

Figure 16: The top figure shows the area near IIT Palakkad where the wells and ponds are located. The bottom two figures show the location of two of the wells under study

The exact amount of fluorides was not determined accurately. From this analysis it is established that the antenna measurement system is able to detect the pollutant levels.

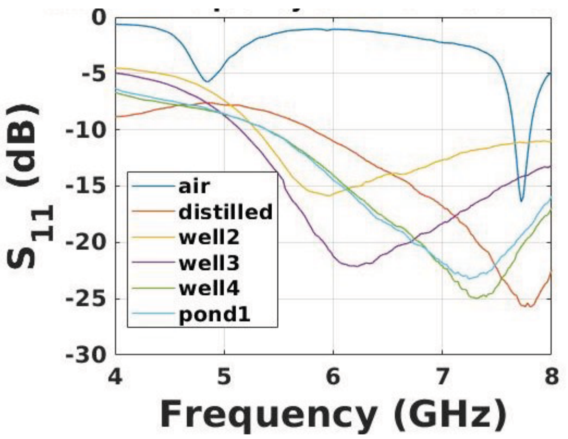

Figure 17: The resonant frequencies for various pollutants present in multiple water sources

Qualitatively low concentration of pollutants shift the resonant frequency of antenna by a fraction of a gigahertz while high concentration reduces the resonant frequency by one to two gigahertz.

6 Summary and conclusion

This study focuses on determining the feasibility of using microstrip antennas (either rectangular or of various layouts) for detection of pollutants and their level in polluted water. The technique is based on the principle that resonance frequency of patch antenna is dependent on the dielectric constant of the microstrip substrate as well as the surrounding fluid. Antenna immersed in water has a different resonance frequency than that of antenna in air because of the change in effective dielectric constant. Thus, there is a shift in the resonance frequency and this shift is related to the dielectric constant of the antenna material as well as the surrounding mixture/solution of salt. To determine the change in dielectric constant of water with frequency and salinity, a simulation-based study has been performed for frequency range 1 to 10 GHz. It has been observed that the dielectric constant of distilled water reduces from 81 to 61 as the frequency is increased from 1 to 10 GHz. Similarly, as the NaCl concentration is increased from 1N to 4N, the dielectric constant reduces to the range of 63 to 31.

For this study an antenna has been designed to operate at 7.65 GHz in air. This antenna is immersed in distilled water as well as in solutions of NaCl, ferric nitrate, potassium nitrate and potassium chloride. A clear shift in resonance frequency dip is observed for antenna immersed in water and various solutions in comparison to the resonance dip in air. For NaCl, the frequency shift magnitude is in the range of 0.4 to 0.9 GHz for concentration range of 1-4 N and 0.1 to 0.4 GHz for frequency range of 0.1 to 1 N. It can also be observed that there is a linear relationship between NaCl concentration and frequency shift magnitude. The frequency shift magnitude is higher at 0.8 to 2 GHz for other salt solutions with concentration 0.1 to 1 N. Similarly, a measurement analysis is performed to determine the shift in resonant frequency when the antenna is immersed in acetone of various level concentrations. It has been observed that resonance frequency shift magnitude is approximately 1.3 to 1.5 GHz. In addition to the above-mentioned tests, the shift in resonant frequency is also determined for water collected from various sources near IIT Palakkad. It has been observed that water from various sources containing various levels of fluorides result in varied frequency shift magnitude.

This whole analysis has clearly shown that a simple patch antenna with a rectangular layout is sensitive to changes in dielectric constant of water which in turn is sensitive to changes in the proportion of salt in water. This antenna is sensitive to small changes in salt concentration of certain types i.e., ferric nitrate, potassium nitrate and potassium chloride. Thus, the sensitivity of the antenna is very high for some of the salts. Antennas can be designed and fabricated for detecting a particular number of polluting agents. Thus, in a multi sensor system for water quality monitoring system a number of antennas can be used for various kinds of pollutants. Thus, antenna resonant frequency measurement systems can complement the present sensor-based techniques to develop an integrated system that is easy to deploy, accurate and cost effective to maintain.

7 Acknowledgments

The authors would like to acknowledge that the research has been conducted at IIT Palakkad and with the active support of IIT Palakkad.

8 Conflict of interest

The authors of this document do not have any Conflict of Interest (COI) in this paper

9 References

1. WHO Newsroom. (2019, June 14). Drinking Water [Online]. Available: https://www.who.int/news-room/fact-sheets/detail/drinking-water#:~:text=Contaminated%20water%20and%20poor%20sanitation,individuals%20to%20preventable%20health%20risks.

2. S. M. Haslam, River pollution — an ecological perspective, Belhaven Press, CBS Publishers, Delhi, India, 2009.
3. M. K. T and U. Raveendranath, “Microwave technique for water pollution study,” Journal of Microwave power and Electromagnetic Energy, vol. 30, pp. 187-195, 1995.
4. World Health Organisation “Guidelines for drinking water quality,” 4th edition, 2017.
5. O. Korostynska, A. Mason and A. I. Al-Shamma’a, “Monitoring Pollutants in Wastewater: Traditional Lab Based versus Modern Real-Time Approaches,” in Smart Sensors for Real-Time Water Quality Monitoring, vol. 3, S. C. Mukhopadhyay, A. Mason, Springer, 2013, pp. 1-24.
6. R. Rosen, “Mass spectrometry for monitoring micropollutants in water,” Current Opinion in Biotechnology, vol. 18, pp. 246–25, 2007.
7. S. A. Jaywant and K. M. Arif, “A comprehensive review of microfluidic water quality monitoring sensors”, *Sensors*, vol. 19, no. 21, pp. 1-37, 2019.
8. W.H. Lee, Y. Seo, P. L. Bishop, “Characteristics of a cobalt-based phosphate microelectrode for in situ monitoring of phosphate and its biological application,” Sensors and Actuators B: Chemical vol. 137, pp. 121–128, 2009.
9. A. Jang, Z. Zou, K. K. Lee, C. H. Ahn & P. L. Bishop, “State-of-the-art lab chip sensors for environmental water monitoring,” Measurement Science and Technology, vol. 22, no. 3, pp. 1-18, 2011.
10. L. Manjakkal et al., “Connected Sensors, Innovative Sensor Deployment, and Intelligent Data Analysis for Online Water Quality Monitoring,” in IEEE Internet of Things Journal, vol. 8, no. 18, pp. 13805-13824, 15 Sept.15, 2021, https://doi.org/10.1109/JIOT.2021.3081772.
11. C. Sicard, C. Glen, B. Aubie, D. Wallace, S. Jahanshahi-Anbuhi, K. Pennings, G. Daigger, R. Pelton, J. D. Brennan, C. D. M. Filipe, “Tools for water quality monitoring and mapping using paper-based sensors and cell phones,” Water Res. , vol. 70, pp. 360–369, 2015.
12. I. Yaroshenko, D. Kirsanov, M. Marjanovic, P. A. Lieberzeit, O. Korostynska, A. Mason, I. Frau, A. Legin, “Real-Time Water Quality Monitoring with Chemical Sensors,” Sensors, vol. 20, no. 12, pages 1-34, 2020.
13. O. Korostynska, A. Mason, A. Al-Shamma. “Flexible Microwave Sensors for Realtime Analysis of Water Contaminants,” Journal of Electromagnetic Waves and Applications, vol. 27, pp. 2075-2089, 2013. https://doi.org/10.1080/09205071.2013.832393.
14. J. B. Hasted, D. M. Ritson and C. H. Collie, “Dielectric properties of Aqueous Ionic Solutions,” The journal of chemical physics, vol. 16, 1947.
15. L. Klein and C. T. Swift, “An Improved Model for the Dielectric Constant of Sea Water at Microwave Frequencies,” IEEE Journal of Oceanic Engineering, vol. 2, pp. 104 – 111, 1977.
16. Hans J. Liebe, H. J. Liebe, G. A. Hufford and T. Manabe, “A Model for the Complex Permittivity of Water at Frequencies below 1 THz,” International Journal of Infrared and Millimeter Waves, vol. 12, pp. 659–675, 1991.
17. A. H. Abdelgwad, T. M. Said and A. M. Gody, “Microwave Detection of Water Pollution in Underground Pipelines,” International Journal on Wireless and Microwave Technologies, vol. 3, pp. 1-15, 2014.
18. K. Cole and R. Cole, “Dispersion and absorption in dielectrics I. Alternating current characteristics,” J. Chem. Phys., vol. 9, pp. 341– 52, 1941.
19. R. Somaraju and J. Trumpf, “Frequency, Temperature and Salinity Variation of the Permittivity of Seawater,” in IEEE Transactions on Antennas and Propagation, vol. 54, no. 11, pp. 3441-3448, Nov. 2006, https://doi.org/10.1109/TAP.2006.884290.
20. P. Debye, Polar Molecules, Dover, 1929.
21. C. A. Balanis, Antenna Theory Analysis and Design, New Jersey: A john Wiley & Sons, 2005.
22. University of Maryland. (2019, June 14). HFSSv10UserGuide [Online]. Available: http://anlage.umd.edu/HFSSv10UserGuide.pdf

Arrived: 07. 02. 2022
Accepted: 12. 07. 2022

Original scientific paper
https://doi.org/10.33180/InfMIDEM2022.302

Informacije MIDEM
Journal of Microelectronics,
Electronic Components and Materials
Vol. 52, No. 3(2022), 159 – 167

Dual-Band X-Shaped Absorber Design for Sensor Applications

Alparslan Cinar[1, 2], *S. Cumhur Basaran*[2]

[1]*Elmali Vocational School, Akdeniz University, Antalya, Turkey*
[2]*Department of Electrical-Electronics Engineering, Akdeniz University, Antalya, Turkey*

Abstract: This study presents a compact absorber design with an X-shaped resonator (XSR) in the S-band region. The proposed design offers single or dual-band absorption peaks, depending on whether the arm lengths of the resonator are symmetrical or asymmetrical. Prototype fabrications of the absorber, whose numerical design was carried out using CST Microwave Studio, were also measured for verification. Based on the simulated and measured results, the proposed absorber exhibited over 93% absorption spectra with relatively narrow bandwidth characteristics desired, especially for sensor applications. It also provided cross-polarized reflections of less than 0.08 at the frequencies of interest. In addition, the absorption frequency changes depending on the dielectric constant and thickness variations of the sensing layer placed on the absorber were obtained numerically and experimentally to investigate the sensing performance of a dual-band configuration of the absorber. In addition, the same analyzes and measurements were carried out again for two separate single-band split-ring resonator (SRR)-based absorbers designed in this study, and their sensing performances were compared with the dual-band X-shaped absorber's (XSA) performance. As a result, it was found that the proposed XSA was more sensitive than the SRR-based absorber (SRRA), considering the comparison results.

Keywords: Dual-band absorber; SRR-based absorber; sensor-based absorber; X-shaped absorber

Zasnova dvopasovnega absorberja v obliki X za senzorske aplikacije

Izvleček: Študija predstavlja kompaktno zasnovo absorberja z resonatorjem v obliki črke X (XSR) v območju pasu S. Predlagana zasnova ponuja eno- ali dvopasovne absorpcijske vrhove, odvisno od tega, ali so dolžine rok resonatorja simetrične ali asimetrične. Za preverjanje smo izmerili tudi prototipne izdelave absorberja, katerega numerična zasnova je bila izvedena s programom CST Microwave Studio. Na podlagi simuliranih in izmerjenih rezultatov je predlagani absorber pokazal več kot 93-odstotni absorpcijski spekter z relativno ozko pasovno širino, ki je zaželena zlasti za senzorske aplikacije. Zagotovil je tudi navzkrižno polarizirane odboje, manjše od 0,08 pri želenih frekvencah. Poleg tega so bile numerično in eksperimentalno pridobljene spremembe absorpcijske frekvence v odvisnosti od dielektrične konstante in spremembe debeline senzorske plasti, nameščene na absorber, da bi raziskali senzorsko zmogljivost dvopasovne konfiguracije absorberja. Poleg tega so bile iste analize in meritve ponovno opravljene za dva ločena enopasovna absorberja na osnovi deljenega obročnega resonatorja (SRR), zasnovana v tej študiji, in njune zmogljivosti zaznavanja so bile primerjane z zmogljivostjo dvopasovnega absorberja v obliki črke X (XSA). Na podlagi rezultatov primerjave je bilo ugotovljeno, da je predlagani XSA občutljivejši od absorberja na osnovi SRR (SRRA).

Ključne besede: dvopasovni absorber; absorber na osnovi SRR; absorber na osnovi senzorja; absorber v obliki črke X

** Corresponding Author's e-mail: alparslancinar@akdeniz.edu.tr*

1 Introduction

Resonator-based electromagnetic wave absorbers have been a popular research topic since 2008, when metamaterials were first considered in absorber structures [1]. Thanks to possessing the capability of high absorption rate, resonator-based absorbers are used in a wide variety of applications such as energy harvest [2], amplitude modulation [3], switching [4], stealth technology [5, 6], solar energy [7], and EMI/EMC [8]. One of the application areas where resonator-based absorbers are used extensively is sensors. Sensor-based absorbers are used to detect physical parameters such

How to cite:
A. Cinar et al., "Dual-Band X-Shaped Absorber Design for Sensor Applications", Inf. Midem-J. Microelectron. Electron. Compon. Mater., Vol. 52, No. 3(2022), pp. 159–167

as pressure, temperature, density and determine the electromagnetic properties of materials under test (MUT). In practical applications, they are expected to have physical properties such as ease of manufacture, compactness, reusability, low cost, and electrical properties such as high sensitivity and quality factor. Many absorber designs of various types and specifications that can meet the principal requirements of the sensor applications have been reported in the literature [9-20]. In most of these studies, SRRs have been used as the primary absorbing structure, allowing high selectivity and quality factors due to their inherent resonant characteristic [10-16]. On the other hand, flower-shaped surrounded with the circular ring in [17] and swastika-shaped resonators in [18] have been considered absorbing elements for sensor applications. Similarly, microstructure metamaterial and substrate integrated waveguide cavity resonators have been employed in [19] and [20], respectively.

This study proposes a novel compact absorber design based on an XSR for the S-band frequency region and investigates its sensor performance. Considering the resonator-based absorbers reported in the literature, the most prominent feature of the proposed design is its simple structure consisting of only one resonator placed on a one-layer substrate. Moreover, the proposed design offers to control the transition between single and dual-band absorption characteristics. The XSR on the single top layer is configured such that the central axes of the two arms coincide at the center of the resonator, dividing both arms in half. When the XSR is symmetrical, a single band frequency response is obtained depending on its arm lengths. When an offset is created between the arm lengths, a dual-band frequency response is achieved thanks to this asymmetric structure, and the absorption frequencies of both bands can be tuned by controlling the offset value. The resonator structure with various dimensions has been analyzed, and corresponding absorption characteristics and surface current density at the respective frequencies are presented in this paper. In addition, two different prototypes, symmetrical and non-symmetrical, were fabricated, and then their absorption characteristics were measured to verify the numerical design.

On the other hand, considering the absorption characteristics, the proposed absorber exhibits a relatively narrow bandwidth performance, which is desired especially for sensor applications. In this context, to evaluate the sensor performance of the proposed absorber, the change in the absorption frequency depends on the dielectric constant and thickness variation of a test material placed on the asymmetric absorber structure providing dual-band absorption peaks at 3.12 and 3.52 GHz was investigated. Also, the proposed absorber's sensitivity of frequency shift was compared to two different SRRAs offering single band absorption peaks at 3.12 GHz and 3.52 GHz, respectively, to support the sensor performance. According to the analysis and measurement results, it was observed that the sensitivity of the proposed absorber was higher than the compared absorbers. In addition to the high sensitivity, its simple and compact structure providing dual-band absorption make the proposed design an important candidate that can be used for sensor applications.

2 Numerical design and experimental setup

Schematic views and design parameters of the proposed absorber configuration are depicted in Fig. 1. As seen, the top plate of the absorber is composed of a copper XSR having a thickness of 0.035 mm and an estimated conductivity of 5.8×10^7 S/m. The copper resonator is printed on a Rogers TMM4 substrate having dielectric permittivity (ε_r) of 4.5 and loss tangent (tan δ) of 0.002. The other side of the substrate is fully covered with the same copper material and is set as the ground plane of the absorber. Herein, the volume of Rogers TMM4 substrate is $L_s \times W_s \times h$, where L_s, W_s, and h are 72.136, 34.036, and 0.76 (all in mm), respectively. On the other hand, l_1, l_2, and w stand for design parameters of the XSR structure, as can be seen in Fig. 1. The w value of 4 mm is also fixed in the design.

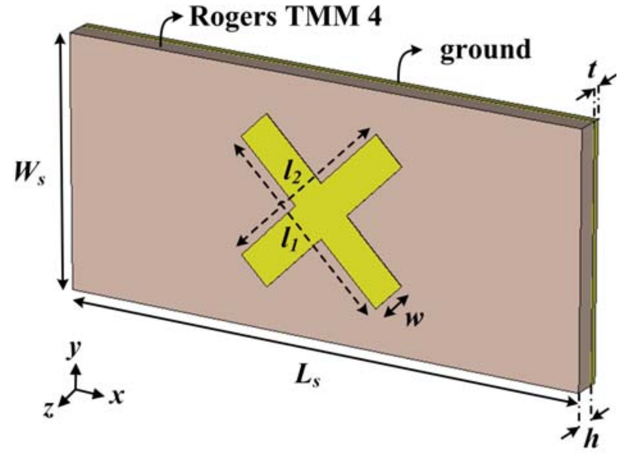

Figure 1: The schematic view and design parameters of the absorber structures.

The absorber's design and numerical analyses were conducted using CST microwave studio (MWS) based on the finite element method. The simulation setup of the absorber is illustrated in Fig. 2(a). Here it is seen that the sidewalls of the waveguide lying on the z-axis are modeled as perfect electrical conductor boundaries ($E_t = 0$). For the excitation purpose, two ends of the waveguide are terminated with input and output ports. Also, the absorber is excited by the TE_{10} mode waveguide port, where electric field vector *E*, magnetic field vector *H*, and propagation vector *k* are along the *y*, *x* and, *z*-axis, respectively. Four prototypes of different sizes were fabricated and measured to verify the numerical design. The λ/4 spacer with a sample prototype and photographs of the measurement setup are shown in Fig. 2(b) and 2(c), respectively. The reflection and transmission coefficient measurements of each prototype placed in the λ/4 spacer were performed using the S-band WR284 waveguide connected to the Agilent Fieldfox N9926A vector network analyzer.

The relationship between the size of the proposed geometry and the resonant frequency has been explained in formula (1).

$$l = \frac{c}{2f\sqrt{\varepsilon_e}} \tag{1}$$

Where *l* is the length of each XSR's arms, *c* is the speed of light, *f* is operating frequency, and ε_e is the effective permittivity of XSR. And also, the effective permittivity of XSR has been calculated using the following equation:

$$\varepsilon_e = \frac{\varepsilon_r + 1}{2} + \frac{\varepsilon_r - 1}{2}\frac{1}{\sqrt{1 + 12\frac{h}{w}}} \tag{2}$$

Where ε_r is the dielectric permittivity of the substrate of XSA, *h* is the thickness of the substrate of XSA and *w* is the width of any of XSR's arms [21].

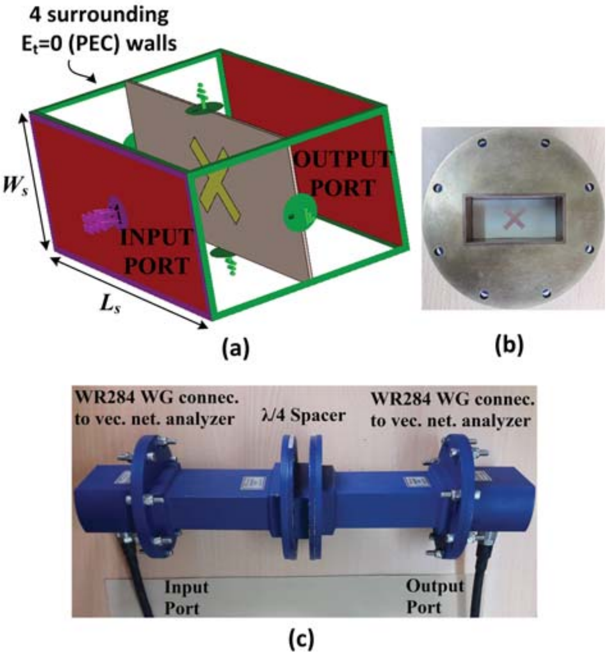

Figure 2: (a) The schematic views of the simulation setup. (b) The picture of λ/4 spacer with a sample prototype. (c) The photograph of the measurement setup.

3 Simulation and measurement results

Based on the design parameters and using the numerical and experimental setups, as explained in the previous section, the symmetrical and asymmetrical configurations of the proposed absorber have been simulated and measured. The simulated and measured absorptions characteristics have been computed using the following equation:

$$absorption = 1 - |S_{11}|^2 - |S_{21}|^2 \tag{3}$$

Where S_{11} and S_{21} parameters denote reflectance and transmittance, respectively, since the bottom face of the structure is completely covered with the ground plane, the transmittance is set as zero. Fig. 3(a) and (b) show the proposed design's simulated and measured absorption spectra for symmetrical and asymmetrical

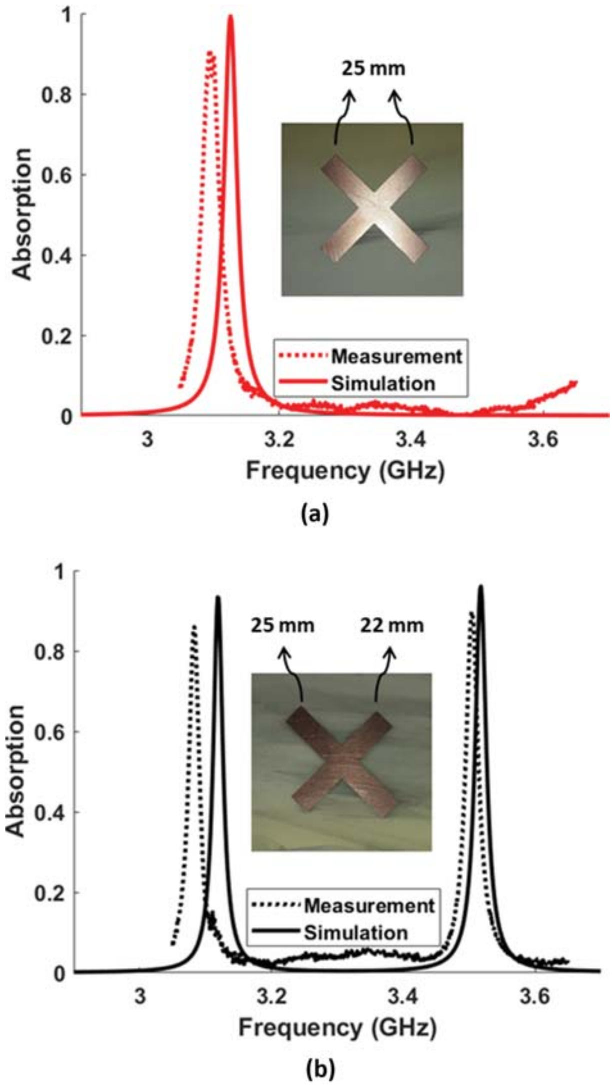

Figure 3: Simulation and measurement absorption characteristics for (a) symmetrical configuration and (b) unsymmetrical configuration.

configurations, respectively. As seen from the figures, the absorber with the symmetrical resonator ($l_1 = l_2 = 25$ mm) offers a single-band absorption peak at 3.13 GHz. On the other hand, the asymmetrical resonator ($l_1 = 22$, $l_2 = 25$ mm) provides dual-band absorption peaks at 3.12 GHz and 3.52 GHz. In addition, over 90% absorption peak levels are observed for all of the respective frequencies.

Since it is known that cross-polarized reflection can occur in asymmetrical structures, the cross-polarized reflection of the dual-band absorber has also been analyzed in this study. In this analysis process, as computation of the cross-polarized reflection is impossible in a rectangular waveguide, a free-space super-cell periodic array has been formed in the CST Studio Suite with two Floquet modes as reported in [22]. For applying the super-cell array, periodic boundary conditions (PBCs) have been imposed at the boundaries of a super-cell, as shown in Fig. 4(a). Also, the mirror image effect of the waveguide PEC walls has been taken into account in the simulator. As a result, the simulator has calculated co- and cross-polarized reflections for the free-space arrays. The absorption spectra have been computed using the formula (4) obtained from Reference [22].

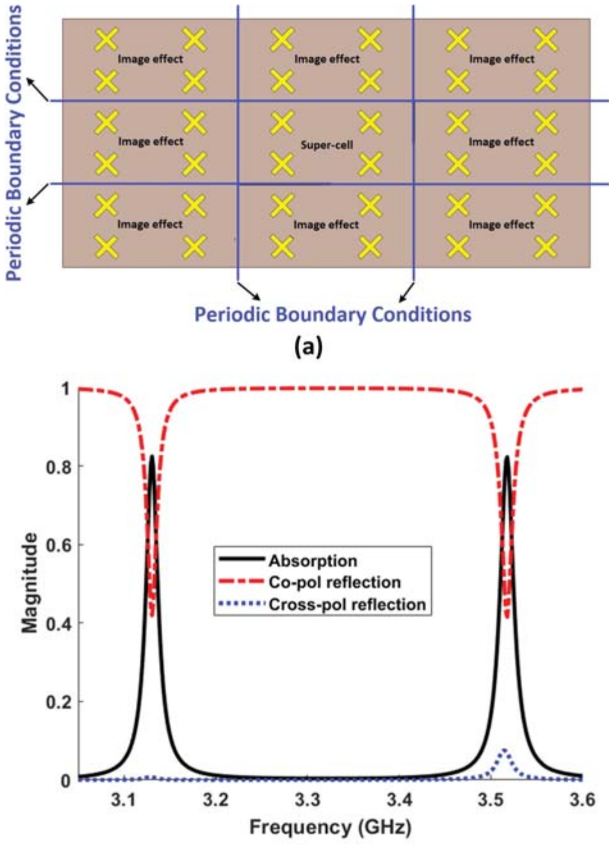

(a)

(b)

Figure 4: (a) Super-cell structure for dual-band absorber. (b) Absorption result regarding cross-polarized reflection, co- and cross-polarized reflections of dual-band absorber for the super-cell array.

$$absorption = 1 - \left|S_{11(co-)}\right|^2 - \left|S_{11(cross-)}\right|^2 \tag{4}$$

Herein, the transmittance is zero due to the presence of the metal ground plane of the absorber structure. According to the calculation, absorption levels of more than 0.8 can be achieved at both frequencies, as shown in Fig. 4(b).

Moreover, we have investigated the surface current density distributions at the related frequencies to support the proposed design's behavior. The simulated current density distributions on both resonator and ground plane of the proposed absorber design at the absorption peaks' frequencies are illustrated in Fig. 5(a) and 5(b), respectively. Herein, the surface currents on the XSR flow through the long arm at the lower frequency mode and flow through the shorter arm at the higher frequency mode. Those surface currents flow uniformly in the related arm of the resonator, and vertical surface currents at the edges of the corresponding arm exhibit the electric dipole resonance behavior. Also, the surface currents flowing at the ground plane in the opposite direction to the currents at the resonator reveal circulation current, which indicates the presence of magnetic dipole.

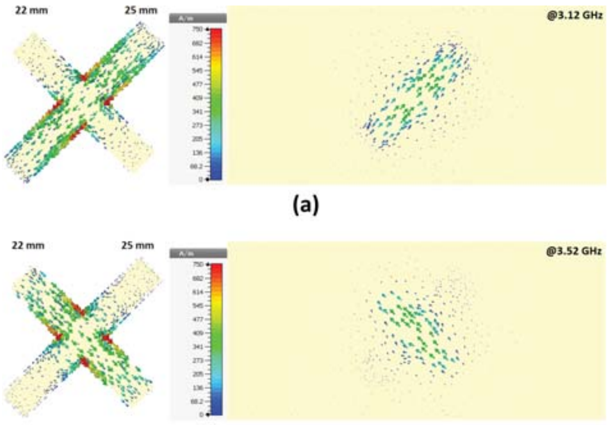

(a)

(b)

Figure 5: Surface current distributions on XSR and ground plane at 180° phase angle for (a) at 3.12 GHz and (b) at 3.52 GHz.

4 Sensing performance of the proposed absorber

The sensing performance of the XSA has also been investigated in this study for sensor applications. For this purpose, the sensitivity of the change in the absorption frequency depending on the dielectric constant (ε_s) and thickness (h_s) variations of a dielectric material placed on the absorber and called the sensing layer has been observed numerically and experimentally. In addition, the same analyzes and measurements have been carried out for the SRRs designed in this study, and their sensing performances have been compared. A typical structure used for the sensitivity analysis of the XSA is shown in Fig. 6. Before presenting the numerical and experimental results obtained, the effect of the sensitivity layer on the absorption frequency is analyzed analytically, considering Fig. 6.

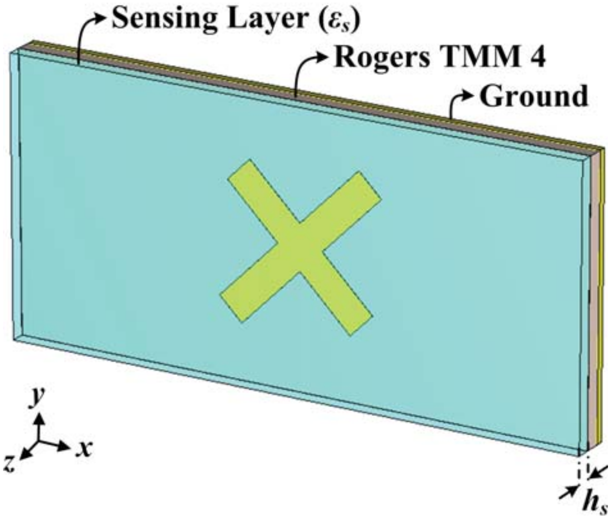

Figure 6: Schematic view of the absorber with the added sensing layer.

As known, the resonant frequency (f_0) can be defined as the following expression;

$$f_0 = \frac{1}{2\pi\sqrt{L_{Total}C_{Total}}} \tag{5}$$

Where L_{Total} and C_{Total} denote total inductance and capacitance of the structure, respectively. Since it is independent of the dielectric property and thickness of the sensing layer, the inductance value does not change [23]. The equivalent total capacitance of the structure consisting of three connected capacitors in series can be obtained using the equation (6). Herein, C_{Abs}, C_{Sen}, and C_{Air} represent the capacitance of the absorber, sensing layer, and air; also, their capacitances can be defined as in equations (7), (8), and (9), respectively. Herein, ε_r and ε_s represent permittivity of the absorber and sensing layer, while h and h_s denote their thickness.

$$\frac{1}{C_{Total}} = \frac{1}{C_{Abs}} + \frac{1}{C_{Sen}} + \frac{1}{C_{Air}} \tag{6}$$

$$C_{Abs} = \frac{\varepsilon_r \varepsilon_0 A}{h} \tag{7}$$

$$C_{Sen} = \frac{\varepsilon_S \varepsilon_0 A}{h_s} \tag{8}$$

$$C_{Air} = \frac{\varepsilon_0 A}{d - h_s} \tag{9}$$

Substituting (7-9) into (6), we can write the total equivalent capacitance as in (10), where d is the entire thickness of the air and sensitivity layer. Here, an air gap of an optimum thickness (d-h_s) is defined on the sensitivity layer for a more realistic calculation of the capacitance value. It is stated that this air gap is at least λ/4 in Electromagnetics Solver based on the finite element method [24]. In this context, the frequency range of the WR284 waveguide is 2.6 to 3.95 GHz. The quarter wavelength of 2.6 GHz of lower frequency is 28.85 mm, and the air gap thickness d is chosen at this value.

$$C_{Total} = \frac{\varepsilon_r \varepsilon_s \varepsilon_0 A}{\varepsilon_r h_s + \varepsilon_s h + \varepsilon_r \varepsilon_s \left(d - h_s\right)} \tag{10}$$

According to equation (10), as the dielectric constant and the thickness of the sensitivity layer increase, the total capacitance also increases, and thus the resonance frequency decreases.

4.1 Simulation and measurement results

To observe the sensing performance of the XSA, its dual-band configuration introduced in the previous section (see Fig. 3(b)) has been analyzed and measured again by placing different sensing layers on it. In these processes, copper-free pure dielectric Rogers RO3006 with the dielectric constant of 6.15 and RO3010 with the dielectric constant of 10.2 materials have been used as sensing layers. Also, the thicknesses of the materials are 0.64 and 1.28 mm.

Fig. 7 and 8 show the simulated and measured absorption characteristics for two different dielectrics constant (6.15 and 10.2) and thickness (0.64 and 1.28 mm) of the sensing layer, respectively. As seen, the simulation and measurement results are in perfect agreement except for slight frequency shifts, probably due to fabrication prototypes and measurement errors. The simulation and measurement results show that the absorber offers dual-band absorption at 3.12 and 3.52 GHz without a sensing layer with very narrow bandwidths. When the sensing layer's permittivity increases, the absorption frequencies shift to lower values, as shown in Fig. 7.

Similarly, when the thickness of the sensing layer is increased, the absorption frequencies move downward, as shown in Fig. 8.

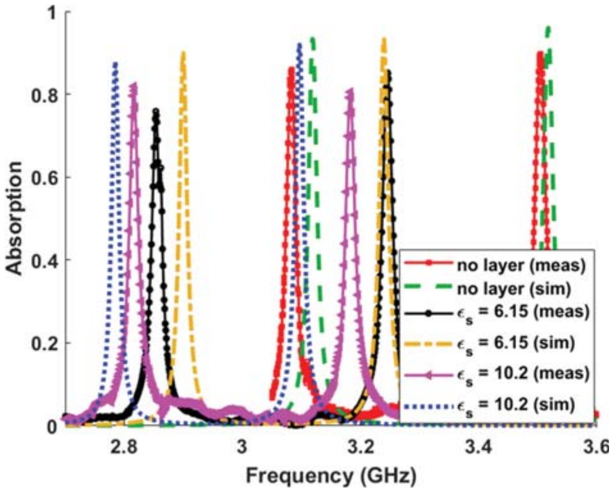

Figure 7: Simulation and measurement results for the different dielectric constant of the sensing layer with 0.64 mm thickness for dual-band absorber.

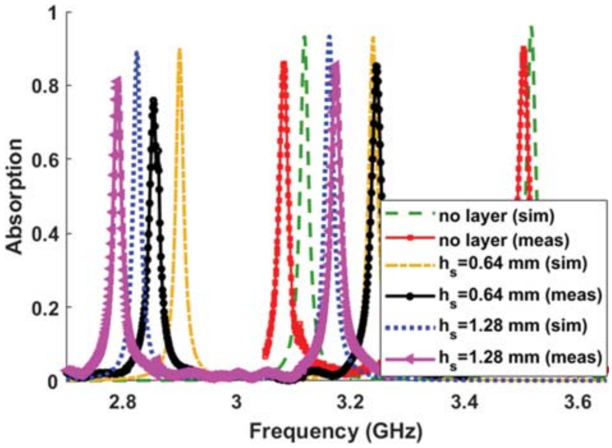

Figure 8: Simulation and measurement results for the different thicknesses of the sensing layer (h_s) with ε_s of 6.15 for the dual-band absorber.

4.2 Performance comparison of the X-shaped and the SRR-based absorbers

In this section, the sensing performance of the dual-band XSA is compared with two separate single-band SRRAs, namely SRR$_{low}$ and SRR$_{up}$ operate in the lower (3.12 GHz) and upper (3.52 GHz) bands of the XSA. Prototype fabrications of the absorbers designed in this study were also performed. Configuration, design parameters, a sample prototype, and configuration with sensing layer are depicted in Fig. 9. The analysis and measurements conducted for the XSA in the previous section are repeated for each SRRA, and the results are illustrated in Fig. 10. As seen from the simulation results in Fig. 10 (a) and (b), the SRR$_{low}$ absorber operates at 3.12 GHz, and SRR$_{up}$ operates at 3.52 GHz without sensing layers. On the other hand, when the permittivities of the sensing layer placed on the absorbers are increased, the absorption frequencies shift to the lower value for both SRRAs.

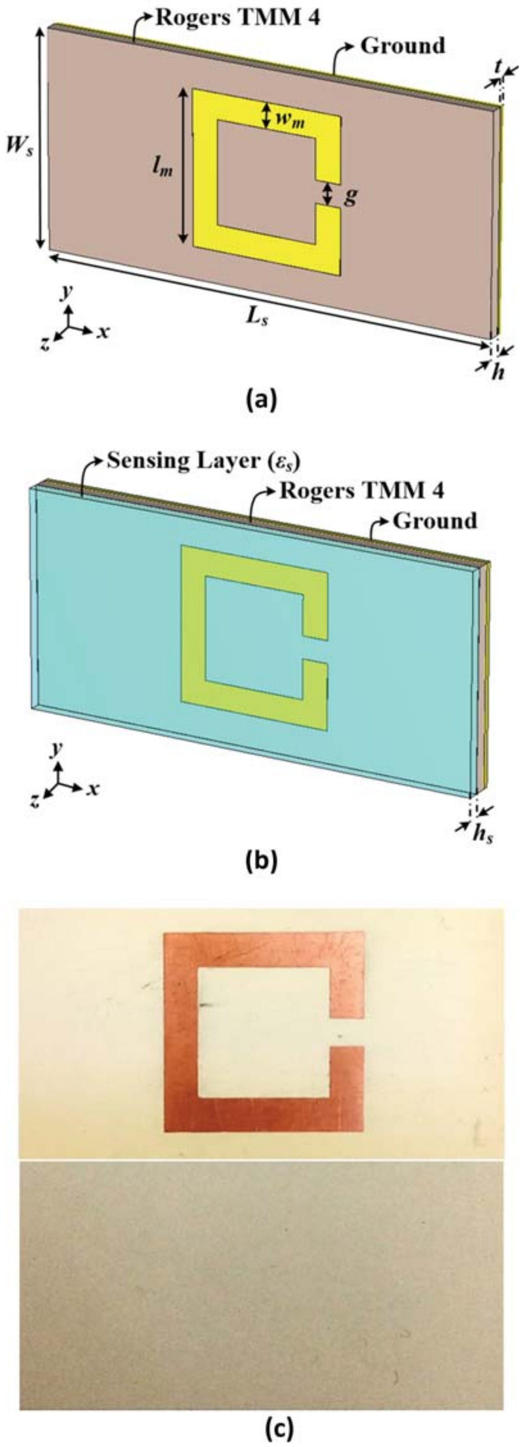

Figure 9: (a) The schematic views and design parameters of the SRRA (l_m=24, w_m =4 and g=3.5 for SRR$_{low}$ and l_m=22, w_m=4 and g=4 for SRR$_{up}$, all in mm). (b) SRRA with sensing layer. (c) Prototype samples of the SRRA and sensing layer.

The simulated and measured absorption frequencies of the absorbers with and without the sensing layers are given in Table 1, comparatively. Herein, f_0 and f_s denote absorption frequencies without and with the sensing layer, respectively. The frequency shifts in the table are calculated using the following equation.

$$\% freq\,shift = \frac{f_0 - f_s}{f_0} \times 100 \qquad (11)$$

Based on the frequency shift values given in the table, it is found that the sensing performance is higher in both frequency bands than SRRAs.

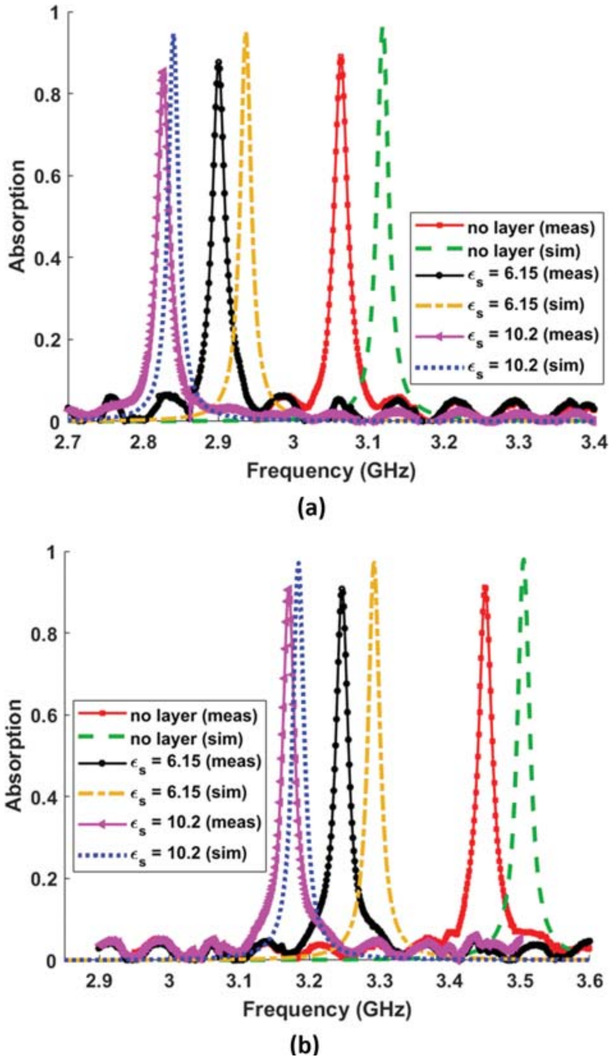

(a)

(b)

Figure 10: Simulation and measurement results for the different dielectric constant of the sensing layer for (a) SRR_{low} and (b) SRR_{up}.

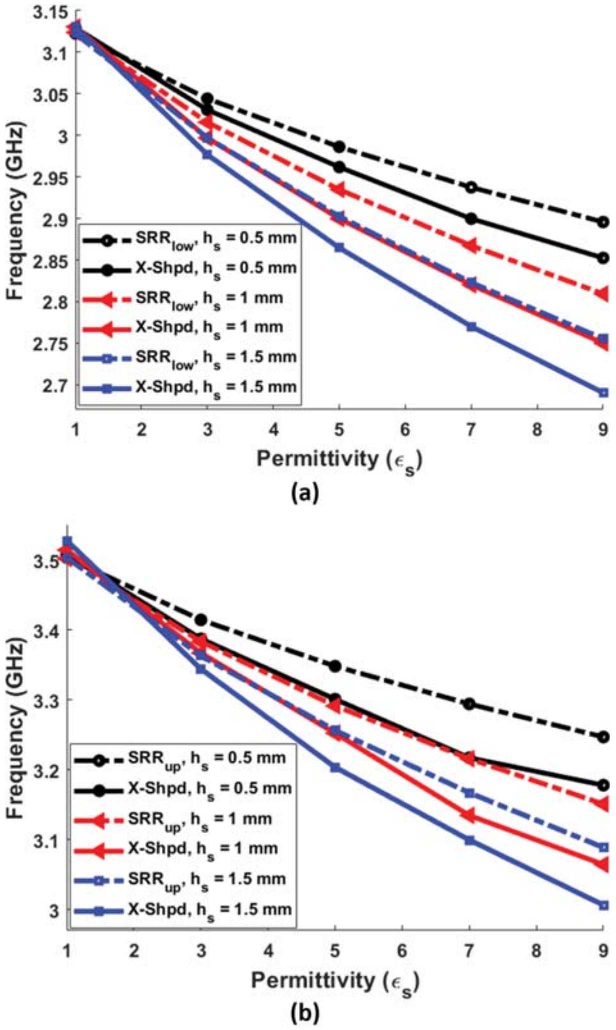

(a)

(b)

Figure 11: Characteristics of the change in the absorption frequency obtained in the simulation environment depending on various thickness (h_s) and dielectric constant (ε_s) values in the (a) lower band and (b) upper band.

Table 1: Numerical and experimental results for the proposed and SRRAs.

Structure	Sensing Layer	Simulation		Measurement	
		f_s (GHz)	freq shift (%)	f_s (GHz)	freq shift (%)
Proposed Absorber	No Layer	3.12 3.52	—	3.08 3.5	—
SRRlow		3.12	—	3.06	—
SRRup		3.52	—	3.45	—
Proposed Absorber	Rogers RO3006	2.90 3.24	7.05 7.95	2.85 3.25	7.47 7.14
SRRlow		2.94	5.80	2.90	5.23
SRRup		3.29	6.27	3.25	5.80
Proposed Absorber	Rogers RO3010	2.79 3.10	10.58 11.93	2.82 3.18	8.44 9.14
SRRlow		2.84	8.97	2.83	7.52
SRRup		3.19	9.12	3.17	8.12

In addition, for the proposed dual-band absorber and each SRRA, the change in the absorption frequency depending on five different dielectric constants and three different thickness values of the sensing layer have been computed in the simulation environment. The simulation results have been comparatively plotted in Fig. 11. It can be seen that the sensing performance of the proposed dual-band absorber is higher than the SRR$_{low}$ in the first band (see Fig. 11 (a)) and the SRR$_{up}$ in the second band (see Fig. 11 (b)) for all thickness and dielectric values of the sensing layer.

5 Conclusions

In this article, a novel absorber design based on an XSR has been introduced. The numerical and experimental results have shown the proposed design offers a single band performance for the case of the symmetrical conducting arms of the XSR and a dual-band operation for the asymmetrical resonator case. In addition, more than 90% of the absorption peaks and relatively narrow bandwidth characteristics have been achieved in the respective bands, as desired, especially for sensor applications. Moreover, It has been found the calculated values of the cross-polarized reflections at the relevant frequencies are smaller than 0.08. Besides, based on the simulated and measured results, it has been observed that the dual-band absorber is more sensitive in both bands than the SRRA designed in this study. On the other hand, by only scaling the design parameters of the proposed design, new absorber configurations exhibiting the same performance can be easily obtained for different frequency regions. Because of these prominent advantages, the proposed absorber structure is a good candidate for sensors and other microwave applications.

6 Acknowledgments

The authors acknowledge the Department of Electrical and Electronics Engineering, Suleyman Demirel University, for providing us the opportunity for the absorber S-parameter measurements in vector network analyzer. And also, the authors would like to thank Assoc.Prof. Dr. Evren Ekmekci, N. Karacan, K.C. Ayvaci, B. Ila, and N.K. Bulut for their help.

7 Conflict of interest

We declare that we do not have any commercial or associative interest that represents a conflict of interest in connection with the work submitted.

8 References

1. N. I. Landy, S. Sajuyigbe, J. J. Mock, D. R. Smith and W. J. Padilla, “A Perfect Metamaterial Absorber”, *Phys Rev Lett*, vol. 100, no. 20, pp. 207402, 2008. https://doi.org/10.1103/PhysRevLett.100.207402
2. E. Unal, F. Dincer, E. Tetik, M. Karaaslan, M. Bakir, and C. Sabah, “Tunable perfect metamaterial absorber design using the golden ratio and energy harvesting and sensor applications”, *J Mater Sci Mater El*, vol. 26, no.12, pp. 9735-9740, 2015. https://doi.org/10.1007/s10854-015-3642-7
3. K. S. Al-Badri, A. Cinar, U. Kose, O. Ertan, and E. Ekmekci, “Monochromatic tuning of absorption strength based on angle-dependent closed-ring resonator-type metamaterial absorber”, *IEEE Antennas Wirel Propag Lett*, vol. 16, pp. 1060-1063, 2016. https://doi.org/10.1109/LAWP.2016.2620599
4. E. Ekmekci, and E. Demir, “On/off switching of absorption spectra by layer shifting for double-layer metamaterial-based absorber”, *IEEE Antennas Wirel Propag Lett*, vol. 15, pp. 532-535, 2015. https://doi.org/10.1109/LAWP.2015.2457091
5. K. Ozden, O. M. Yucedag, and H. Kocer, “Metamaterial based broadband RF absorber at X-band”, *AEU-Int J Electron C*, vol. 70, no. 8, pp. 1062-1070, 2016. https://doi.org/10.1016/j.aeue.2016.05.002
6. S. Li, X Cao, T. Liu, and H. Yang, “Double-layer perfect metamaterial absorber and its application for RCS reduction of antenna”, *Radioengineering*, vol. 23, no. 1, pp. 222-229, 2014. radioeng.cz/papers/2014-1.htm
7. H. Wang, and L. Wang, “Perfect selective metamaterial solar absorbers”, *Opt Express*, vol. 21, no. 106, pp. A1078-A1093, 2013. https://doi.org/10.1364/OE.21.0A1078
8. N. Mishra, K. Kumari, and R. K. Chaudhary, “An ultra-thin polarization-independent quad-band microwave absorber based on compact metamaterial structures for EMI/EMC applications”, *Int J Microw Wirel T*, vol. 10, no. 4, pp. 422-429, 2018. https://doi.org/10.1017/S1759078718000491
9. A. Hoque, M. Tariqul Islam, A. F. Almutairi, T. Alam, M. Jit Singh, and N. A. Amin, “A polarization-independent quasi-TEM metamaterial absorber for X and Ku band sensing applications”, *Sensors*, vol. 18, no. 12, pp. 4209, 2018. https://doi.org/10.3390/s18124209
10. M. Bakir, M. Karaaslan, O. Akgol, O. Altintas, E. Unal and C. Sabah, “Sensory applications of resonator-based metamaterial absorber”, *Optik,* vol. 168, pp. 741-746, 2018. https://doi.org/10.1016/j.ijleo.2018.05.002

11. M. Bakır, M. Karaaslan, E. Unal, O. Akgol, and C. Sabah, “Microwave metamaterial absorber for sensing applications”, *Opto-Electron Rev*, vol. 25, no. 4, pp. 318-325, 2017. https://doi.org/10.1016/j.opelre.2017.10.002
12. M. L. Hakim, T. Alam, A. F. Almutairi, M. F. Mansor, and M. T. Islam, “Polarization insensitivity characterization of a dual-band perfect metamaterial absorber for K band sensing applications”, *Sci Rep*, vol. 11, no. 1, pp. 1-14, 2021. https://doi.org/10.1038/s41598-021-97395-0
13. A. Abdelsallam, A. Gaafar, and M. Abdalla, “Oblique and Polarization Independent Metasurface-Based Absorber for Bio-Sensing Applications”, *IETE J Res*, pp. 1-10, 2021. https://doi.org/10.1080/03772063.2021.1920853
14. X. Ling, Z. Xiao, and X. Zheng, “Tunable terahertz metamaterial absorber and the sensing application”, *J Mater Sci: Mater Electron*, vol. 29, no. 2, pp. 1497-1503, 2018. https://doi.org/10.1007/s10854-017-8058-0
15. M. R. Nickpay, M. Dannie, and A. Shahzadi, “Highly sensitive THz refractive index sensor based on folded split-ring metamaterial graphene resonators”, *Plasmonics*, pp. 1-12, 2021. https://doi.org/10.1007/s11468-021-01512-8
16. M. S. Sim, K. Y. You, F. Esa, M. N. Dimon, and N. H. Khamis, “Multiband metamaterial microwave absorbers using split ring and multi-width slot structure”, *Int J RF Microwave Comput Aided Eng*, vol. 28, no. 7, pp. e21473, 2018. https://doi.org/10.1002/mmce.21473
17. M. A. Shukoor, V. Kumar, and S. Dey, “Compact polarisation insensitive wide angular stable triple-band absorber for RF energy harvesting, RCS reduction, and sensor applications”, *Int J RF Microwave Comput Aided Eng*, vol. 31, no. 9, pp. e22763, 2021. https://doi.org/10.1002/mmce.22763
18. Y. I. Abdulkarim, L. Deng, O. Altıntaş, E. Ünal, and M. Karaaslan, “Metamaterial absorber sensor design by incorporating swastika-shaped resonator to the determination of the liquid chemicals depending on electrical characteristics”, *Physica E*, vol. 114, pp. 113593, 2019. https://doi.org/10.1016/j.physe.2019.113593
19. A. Hoque, M. T. Islam, A. F. Almutairi, M. E. H. Chowdhury, and Md. Samsuzzaman, “SNG and DNG meta-absorber with fractional absorption band for sensing application”, *Sci Rep*, vol. 10, no.1, pp. 1-17, 2020. https://doi.org/10.1038/s41598-020-69792-4
20. M. Amiri, M. Abolhasan, N. Shariati and J. Lipman, “Soil moisture remote sensing using SIW cavity-based metamaterial perfect absorber”, *Sci Rep*, vol. 11, no.1, pp. 1-17, 2021. https://doi.org/10.1038/s41598-021-86194-2
21. D. M. Pozar, “Microwave Resonators,” in Microwave Engineering, 4th ed. Hoboken, United States of America: John Wiley & Sons, Inc., 2012, ch. 6, sec. 2, pp. 283.
22. N. Karacan, E. Ekmekci, and G. Sayan, “Response to “Comment on ‘Sliding planar conjoined cut-wire-pairs: A novel approach for splitting and controlling the absorption spectra’” [J. Appl. Phys. 128, 126101 (2020)]”, *J Appl Phys*, vol. 128, pp. 126102, 2020. https://doi.org/10.1063/5.0018386
23. E. Ekmekci, and G. Turhan-Sayan, “Multi-functional metamaterial sensor based on a broad-side coupled SRR topology with a multi-layer substrate”, *Appl Phys A*, vol. 110, no. 1, pp. 189-197, 2013. https://doi.org/10.1007/s00339-012-7113-1
24. O. E. Mrabet, “High frequency structure simulator (HFSS) tutorial”, *IETR UMR CNRS 6164*, 2006.

Arrived: 14. 02. 2022
Accepted: 12. 07. 2022

Original scientific paper
https://doi.org/10.33180/InfMIDEM2022.303

Informacije MIDEM
Journal of Microelectronics,
Electronic Components and Materials
Vol. 52, No. 3(2022), 169 – 179

Novel Voltage-Mode PID Controller Using a Single CCTA and All Grounded Passive Components

Pratya Mongkolwai[1], Worapong Tangsrirat[2], Taweepol Suesut[2]*

[1]Department of Instrumentation Engineering, Faculty of Engineering, Rajamangala University of Technology Rattanakosin (RMUTR), Nakhon Pathom, Thailand
[2]Department of Instrumentation and Control Engineering, School of Engineering, King Mongkut's Institute of Technology Ladkrabang (KMITL), Bangkok Thailand

Abstract: A compact voltage-mode proportional-integral-derivative (PID) controller based on the utilization of a single current conveyor transconductance amplifier (CCTA) is presented in this paper. The presented active PID controller is made up of a single CCTA, and four truly grounded passive components, i.e. two resistors, and two capacitors. The design consideration of the controller parameters has been examined. Besides, the crucial sensitivity performances of the controller parameters for ideal and non-ideal conditions have also been discussed. An application on the closed-loop test system is demonstrated to validate the practicability of the proposed PID controller circuit. To confirm the theoretical behavior, the proposed circuit is simulated with the PSPICE program using TSMC 0.35-µm CMOS process technology. Experimental test results based on commercially available CFOA AD844 and OTA CA3080 integrated circuits are also provided to demonstrate the practicality of the proposed circuit.

Keywords: Current Conveyor Transconductance Amplifier (CCTA); proportional-integral-derivative (PID) controllers; feedback control system; voltage-mode circuit

Nov krmilnik PID v napetostnem načinu z uporabo enega CCTA in ozemljenih pasivnih komponent

Izvleček: V članku je predstavljen kompakten napetostni proporcionalno-integralno-derivativni (PID) krmilnik, ki temelji na uporabi enega samega tokovnega ojačevalnika (CCTA). Predstavljeni aktivni krmilnik PID je sestavljen iz enega CCTA in štirih ozemljenih pasivnih komponent, tj. dveh uporov in dveh kondenzatorjev. Preučena je bila zasnova parametrov krmilnika. Poleg tega so bile obravnavane tudi ključne občutljivosti parametrov regulatorja za idealne in neidealne pogoje. Za potrditev uporabnosti predlaganega vezja PID regulatorja je prikazana uporaba na zaprtem preskusnem sistemu. Za potrditev teoretičnega obnašanja je predlagano vezje simulirano s programom PSPICE z uporabo 0,35-m CMOS procesne tehnologije TSMC. Za dokazovanje praktičnosti predlaganega vezja so na voljo tudi rezultati eksperimentalnih preskusov, ki temeljijo na komercialno dostopnih integriranih vezjih CFOA AD844 in OTA CA3080.

Ključne besede: tokovni transkonduktančni ojačevalnik (CCTA); proporcionalno-integralno-derivativni krmilniki (PID); povratni krmilni sistem; napetostno vezje

---

** Corresponding Author's e-mail: worapong.ta@kmitl.ac.th*

1 Introduction

Proportional-Integral-Derivative (PID) controllers are the most commonly employed control actions in feedback control systems, and process industries [1]. They have been extensively utilized for several decades since they feature a variety of desired properties, including design simplicity, low cost, robustness, and broad application, as well as easy parameter tuning [2]. Their wide range of applications have stimulated and sustained the design and invention of various PID controller circuits and sophisticated hardware modules. Over the last two decades, the enormous literature on PID process controllers has featured a wide range of design techniques based on numerous active compo-

How to cite:
P. Mongkolwai et al., "Novel Voltage-Mode PID Controller Using a Single CCTA and All Grounded Passive Components", Inf. Midem-J. Microelectron. Electron. Compon. Mater., Vol. 52, No. 3(2022), pp. 169–179

nents, such as operational transconductance amplifiers (OTAs) [3], second generation current conveyors (CCIIs) [4]-[5], current feedback operational amplifiers (CFOAs) [6]-[9], current differencing buffered amplifiers (CDBAs) [10], differential voltage current conveyor transconductance amplifiers (DVCCTAs) [11], current follower transconductance amplifiers (CFTAs) [12]-13], voltage differencing transconductance amplifiers (VDTAs) [14], voltage differencing current conveyors (VDCCs) [15], and second generation voltage conveyors (VCIIs) [16]. In [3]-[4], [6], [9]-[10], the PID controllers designed with the signal-flow graph approach have been proposed. However, for the realizations in [3]-[4], [9]-[10], [16], at least four active components were required. Furthermore, PID controller realizations of [4]-[6], [9]-[11], [13]-[15] include a number of passive components, i.e., at least five passive components, some of which are also floating. Floating passive components were used to design single active element-based PID controller circuits in [7]-[8], [12]-[13], [15]-[16]. Active circuit structures with all grounded passive elements are well recognized to be useful for fully integrated circuit (IC) design as well as IC hybrid fabrication processes. This is due to the fact that the usage of grounded passive elements is helpful for the electronic adjustability and permits the elimination/accommodation of various parasitic effects for IC implementation. Another point to note is that the performance and application of the previously discussed controllers [3]-[7], [10]-[15] were evaluated solely through computer simulations. For acceptability purposes, experimental measurements are the important method to evaluate the practicability of the circuit.

The current conveyor transconductance amplifier (CCTA) is a contemporary versatile active circuit block that is a cascade of a CCII and an OTA [17]. The CCTA has been extensively used in the design of analog signal processing circuits and solutions like as analog filters [18]-[20], sinusoidal oscillators [21]-[22], resistor-less inductance simulator [23], and high-frequency active meminductor emulator [24].

Therefore, this work aims at proposing a CCTA-based voltage-mode PID controller with a canonic and low-component count. It is made up of only one CCTA as an active component and all grounded passive components, such as two resistors and two capacitors. There is no element-equality criteria required for the controller realization. Non-ideal gain effects on the controller performance and sensitivity analysis are also investigated. The functionality of the proposed PID controller is evaluated in a closed-loop system. As an example plant circuit, a second-order lowpass filter was built to design the closed-loop system. To test the behavior of the proposed PID controller circuit, some computer simulations using the PSPICE software and experimental measurement data using off-the-shelf integrated circuits AD844 and CA3080 are presented.

Table 1 illustrates the comparative analysis of all previously mentioned PID controllers as having the following desirable properties to substantiate the proposition of the proposed controller: (i) the number of active elements, (ii) the number of passive elements, (iii) the use of all grounded passive elements, (iv) electronic tunability, (v) simulation technology, (vi) simulation supply voltages, (vii) simulated total power consumption, (viii) experimental technology, and (ix) experimental supply voltages.

2 Circuit description

2.1 CCTA properties

Basically, the CCTA is a versatile active building block designed by the cascade connection of CCII followed by an OTA [17]. The schematic symbol of the CCTA is depicted in Fig.1. The voltage drop at terminal x follows the applied voltage at terminal y in magnitude. The output currents at terminals z and zc follow the current through terminal x in magnitude. The voltage drop at terminal z is converted to an output current at terminal o with the transconductance gain (g_m). The terminal relationship of the ideal CCTA can be described by the following set of equations:

$$\begin{bmatrix} i_y \\ v_x \\ i_z \\ i_{zc} \\ i_o \end{bmatrix} = \begin{bmatrix} 0 & 0 & 0 & 0 \\ 0 & 1 & 0 & 0 \\ 1 & 0 & 0 & 0 \\ 1 & 0 & 0 & 0 \\ 0 & 0 & g_m & 0 \end{bmatrix} \begin{bmatrix} i_x \\ v_y \\ v_z \\ v_o \end{bmatrix} \quad (1)$$

In general, the transconductance g_m can be modified electronically by adjusting the externally provided current I_B.

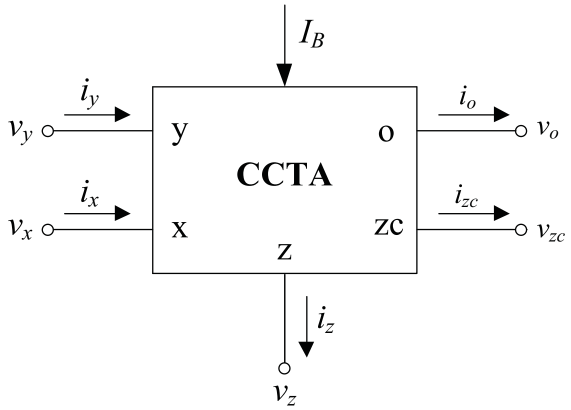

Figure 1: Schematic symbol for the CCTA

2.2 Proposed single CCTA-based PID controller circuit

In a general PID controller, three modes of controller with proportional, integral, and derivative actions must be incorporated. As a consequence, the transfer function of a standard voltage-mode PID controller is generally defined as follows: [25]

$$T(s)=\frac{V_{out}(s)}{V_{in}(s)}=K_P+\frac{K_I}{s}+sK_D \tag{2}$$

where $V_{in}(s)$ is the input voltage, $V_{out}(s)$ is the output voltage, K_P is the proportional coefficient, K_I is the integral coefficient, and K_D is the derivative coefficient.

Fig.2 shows the proposed voltage-mode PID controller based on CCTA as an active component. The controller comprises only a single CCTA, and all grounded passive components, i.e. two resistors and two capacitors. From the aspect of an integrated circuit, it is critical to employ all grounded passive components. The circuit analysis of the proposed PID controller in Fig.2 gives the following voltage transfer function.

$$G_c(s)=\frac{V_{oc}(s)}{V_{ic}(s)}=\frac{R_2}{R_1}\left(1+\frac{g_m R_1 C_1}{C_2}\right)+\frac{g_m R_2}{sR_1C_2}+sR_2C_1 \tag{3}$$

By comparing the above obtained function with the general equation of the PID controller given in equation (2), the various coefficients of the proposed controller are determined to be as follows:

$$K_P=\frac{R_2}{R_1}\left(1+\frac{g_m R_1 C_1}{C_2}\right) \tag{4}$$

Table 1: Comparative features of the proposed circuit with previously reported PID controllers

Circuit	(i)	(ii)	(iii)	(iv)	Simulation results			Experimental results	
					(v)	(vi)	(vii)	(viii)	(ix)
Ref. [3] in 2001	OTA = 8	C = 2	yes	yes	0.8-µm AMS	±5V	N/A	--	--
Ref. [4] in 2001	VB = 4, CCII+ = 4	R = 8, C = 2	no	no	AD844	±12V	N/A	--	--
Ref. [5] in 2006	CCII+ = 1, DO-CCII+ = 1	R = 3, C = 2	yes	no	0.35-µm TSMC	±1.5V, +0.5V	N/A	--	--
Ref. [6] in 2001	CFOA = 6	R = 12, C = 2	no	no	--	--	--	--	--
Ref. [7] in 2013	CFOA = 1	R = 2, C = 2	no	no	AD844	±12 V	N/A	--	--
Ref. [8] in 2018	CFOA = 1	R = 2, C = 2	no	no	0.18-µm TSMC	±2 V	N/A	AD844	±12 V
Ref. [9] in 2021	CFOA = 2	R = 3, C = 2	no	no	AD844	N/A	N/A	AD844	±12 V
Ref. [10] in 2006	CDBA = 4	R = 8, C = 2	no	no	0.8-µm AMS	±2.5V, ±1V	N/A	--	--
Ref. [11] in 2019	DVCCTA=1	R = 3, C = 2	no	yes	0.25-µm TSMC	±1.5 V, -1 V	N/A	--	--
Ref. [12] in 2015	ZC-CFTA = 1	R = 2, C = 2	no	yes	0.35-µm BiCMOS	±1 V	23.7 mW	--	--
Ref. [13] in 2021	CFTA = 2	R = 4, C = 2	no	yes	0.18-µm TSMC	±0.6 V	1.12 mW	--	--
Ref. [14] in 2016	VDTA = 2	R = 3, C = 2	no	yes	0.18-µm MOSIS	±0.9 V	N/A	--	--
Ref. [15] in 2021	VDCC = 1	R = 4, C = 2	no	yes	0.18-µm TSMC	±0.9 V	N/A	--	--
Ref. [16] in 2022	VCII = 1	R = 2, C = 2	no	no	0.18-µm TSMC	±0.9 V	N/A	AD844	±15 V
Proposed circuit	CCTA = 1	R = 2, C = 2	yes	yes	0.35-µm TSMC	±1.5 V	35.8 mW	AD844, CA3080	±5 V

N/A = not available, “ **--** ” = not provided
VB = voltage buffer, CCII+ = plus-type CCII, DO-CCII+ = dual-output plus-type CCII, ZC-CFTA = z-copy CFTA,

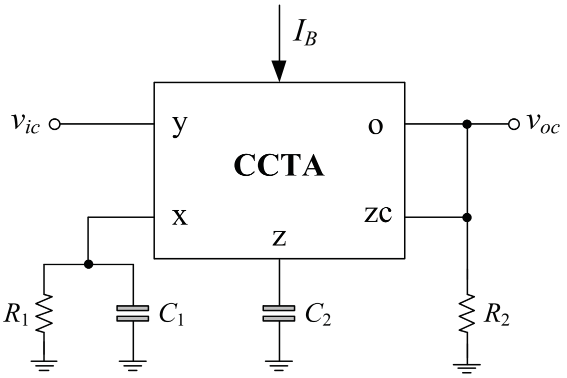

Figure 2: Proposed single CCTA-based PID controller using all grounded passive elements.

$$K_I = \frac{g_m R_2}{R_1 C_2} \tag{5}$$

and

$$K_D = R_2 C_1 \tag{6}$$

As seen from the above expressions, the various gain coefficients of the PID controller can be controlled electronically. The expressions also show that the three coefficients can be determined by appropriately setting the values of g_m, R_1, R_2, C_1 and C_2. The design considerations will be outlined in the following section. Because the primary contribution of this work is the design of a compact analog PID controller with a minimal number of active and passive components, independent tuning of the gain coefficients K_P, K_I and K_D is not expected. Due to the low component count, the circuit requires a small chip area. As a result, the production cost is lowered.

2.3 Practical design considerations

In order to realize the desired gain parameters of the proposed PID controller indicated in equations (4)-(6), the design procedure for setting the circuit components is described as follows.

From equations (5) and (6), the values of capacitors C_1 and C_2 so obtained are expressed as

$$C_1 = \frac{K_D}{R_2} \tag{7}$$

and

$$C_2 = \frac{g_m R_2}{R_1 K_I} \tag{8}$$

Therefore, substituting these relations into equation (4), we then obtain

$$K_P = \frac{R_2}{R_1} + \frac{g_m K_I K_D}{R_2} \tag{9}$$

According to the PID design criteria, the coefficients K_I and K_D are supposed to be arbitrarily determined parameters. By taking

$$R_2 = x R_1 \tag{10}$$

the gain K_P modifies to

$$K_P = x + \frac{g_m K_I K_D}{x R_1} \tag{11}$$

The minimum value of K_P derived from equation (11) is obtained at

$$x = \sqrt{\frac{g_m K_I K_D}{R_1}} \tag{12}$$

and its minimum value can be given below:

$$K_{P(\min)} = 2\sqrt{\frac{g_m K_I K_D}{R_1}} \tag{13}$$

It can be realized from equation (13) that the value of $K_{P(\min)}$ is determined by the given values of K_I and K_D. As a result, the useful value for the gain K_P should satisfy the following relationship:

$$K_P \geq 2\sqrt{\frac{g_m K_I K_D}{R_1}} \tag{14}$$

Rearranging equation (11), we found that

$$.x^2 + x K_P + \frac{g_m K_I K_D}{R_1} = 0 \tag{15}$$

Based on the condition of the K_P value specified in equation (14), equation (15) has two real roots, as illustrated below.

$$x_{1,2} = \frac{K_P}{2} \pm \sqrt{\frac{K_P^2}{4} - \frac{g_m K_I K_D}{R_1}} \tag{16}$$

Therefore, the basic steps in the sequel are followed to determine the required controller parameters, and satisfy the K_P value given in equation (14).
Step (1): Choose g_m and R_1 arbitrarily.
Step (2): Determine x from equation (16).
Step (3): Determine R_2 from equation (10).
Step (4): Determine C_1 from equation (7).
Step (5): Determine C_2 from equation (8).

2.4 Non-ideal effects

The non-ideal condition of the real CCTA is investigated in this section. The port relationship of the non-ideal

CCTA, including tracking errors, can be modeled by the following matrix equation:

$$\begin{bmatrix} i_y \\ v_x \\ i_z \\ i_{zc} \\ i_o \end{bmatrix} = \begin{bmatrix} 0 & 0 & 0 & 0 \\ 0 & \beta & 0 & 0 \\ \alpha & 0 & 0 & 0 \\ \alpha & 0 & 0 & 0 \\ 0 & 0 & \delta g_m & 0 \end{bmatrix} \begin{bmatrix} i_x \\ v_y \\ v_z \\ v_o \end{bmatrix} \tag{17}$$

where $\beta = 1 - \varepsilon_v$ and $\alpha = 1 - \varepsilon_i$ are the non-ideal gains. The parameters ε_v ($|\varepsilon_v| << 1$) and ε_i ($|\varepsilon_i| << 1$) represent the voltage and current tracking errors from the y to the x terminals and from the x to the z and zc terminals, respectively. The non-ideal gain $\delta = 1 - \varepsilon_{gm}$, where ε_{gm} ($|\varepsilon_{gm}| << 1$) is the transconductance tracking error between the z and o terminals.

By taking the non-ideal CCTA into effect, the voltage transfer function of the proposed PID controller in Fig.2 can be derived as:

$$G_c(s) = \frac{\alpha\beta R_2}{R_1}\left(1 + \frac{\delta g_m R_1 C_1}{C_2}\right) + \frac{\alpha\beta\delta g_m R_2}{s R_1 C_2} + s\alpha\beta R_2 C_1 \tag{18}$$

In this case, the non-ideal gain parameters of the PID controller can then be obtained as:

$$K_P = \frac{\alpha\beta R_2}{R_1}\left(1 + \frac{\delta g_m R_1 C_1}{C_2}\right) \tag{19}$$

$$K_I = \frac{\alpha\beta\delta g_m R_2}{R_1 C_2} \tag{20}$$

and

$$K_D = \alpha\beta R_2 C_1 \tag{21}$$

The above expressions clearly show that the non-ideal gains β, α and δ of the CCTA have a direct effect on the PID gain parameters K_P, K_I and K_D. The absolute coefficients of the active and passive sensitivity versus PID gain parameters are found to be less than or equal to unity, as shown by the following equations:

$$S_{g_m}^{K_P} = S_{\delta}^{K_P} = \frac{1}{\left(1 + \dfrac{C_2}{\delta g_m R_1 C_1}\right)} < 1 \tag{22}$$

$$S_{\alpha}^{K_P} = S_{\beta}^{K_P} = 1 \tag{23}$$

$$S_{R_1}^{K_P} = -\frac{1}{\left(1 + \dfrac{\delta g_m R_1 C_1}{C_2}\right)} < -1 \tag{24}$$

$$S_{R_2}^{K_P} = 1 \tag{25}$$

$$S_{C_1}^{K_P} = \frac{1}{\left(1 + \dfrac{C_2}{\delta g_m R_1 C_1}\right)} < 1 \tag{26}$$

$$S_{C_2}^{K_P} = -\frac{1}{\left(\dfrac{1}{\delta} + \dfrac{C_2}{\delta g_m R_1 C_1}\right)} < -1 \tag{27}$$

$$S_{g_m}^{K_I} = S_{\alpha}^{K_I} = S_{\beta}^{K_I} = S_{\delta}^{K_I} = 1 \tag{28}$$

$$S_{R_1}^{K_I} = -S_{R_2}^{K_I} = S_{C_2}^{K_I} = -1 \tag{29}$$

$$S_{\alpha}^{K_D} = S_{\beta}^{K_D} = 1 \tag{30}$$

and

$$S_{R_2}^{K_D} = S_{C_1}^{K_D} = 1 \tag{31}$$

3 Simulation results

The theoretical assumptions are validated through PSPICE simulation utilizing 0.35-μm CMOS process parameters provided by TSMC. For simulation, the CMOS implementation of the CCTA shown in Fig.3 was used with symmetrical supply voltages of ±1.5 V. Transistor aspect ratios are provided in Table 2. The transconductance of the CCTA is found as:

$$g_m = \sqrt{K I_B} \tag{32}$$

where $K = \mu C_{ox}(W/L)$. Here, the parameters μ, C_{ox}, W, and L denote electron mobility, oxide capacitance per unit gate area, effective channel width, and effective channel length, respectively. The transconductance g_m is dependent on the process parameter K, and the external bias current I_B, according to equation (32). The plot in Fig.4 also illustrates the variations in g_m for the CMOS CCTA in Fig.3, which are relatively dependent on variations in I_B. It has been analyzed that, when I_B is varied from 40 μA to 230 μA, the percentage inaccuracy in g_m is less than 9% compared to the theoretical g_m value.

Table 2: Aspect ratios of the transistors of CMOS CCTA in Fig.3

Transistor	W/L (μm/μm)
M_1-M_2, M_{12}-M_{13}	16/0.7
M_3-M_6, M_{16}	7/0.7
M_7-M_{11}, M_{19}-M_{20}	21/0.7
M_{14}-M_{15}	28/0.7
M_{17}-M_{18}	8.5/0.7

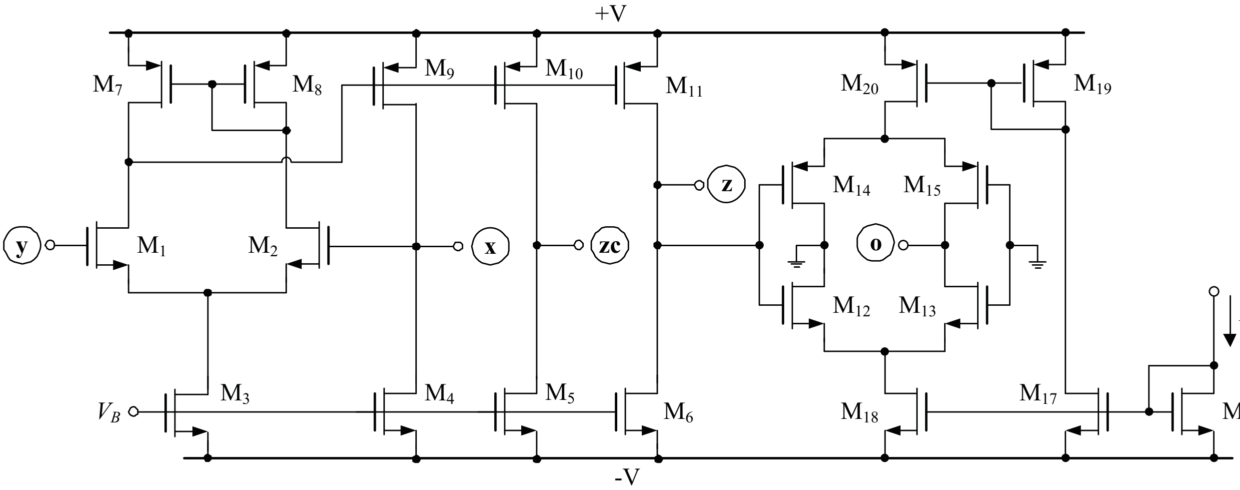

Figure 3: Possible CMOS realization of the CCTA used in simulations

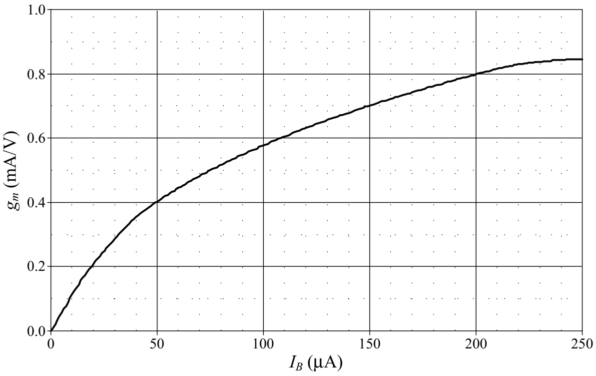

Figure 4: g_m plot for variations in I_B for the CMOS CCTA in Fig.3

Firstly, the proposed PID controller circuit in Fig.2 was designed with the following components: g_m = 0.61 mA/V (I_B = 100 μA), R_1 = 1 kΩ, R_2 = 5 kΩ, and C_1 = C_2 = 1 nF. The corresponding controller gains are obtained as: K_P = 8, K_I = 3 Ms, and K_D = 5 μs. The ideal and simulated transient responses of the proposed controller, for a 100-mV triangular input voltage with a frequency of 500 kHz, are shown in Fig.5. For frequency-domain performance analysis, the ideal and simulated responses with identical component values are shown in Fig.6. The total power consumption of the proposed PID controller is found as 35.8 mW.

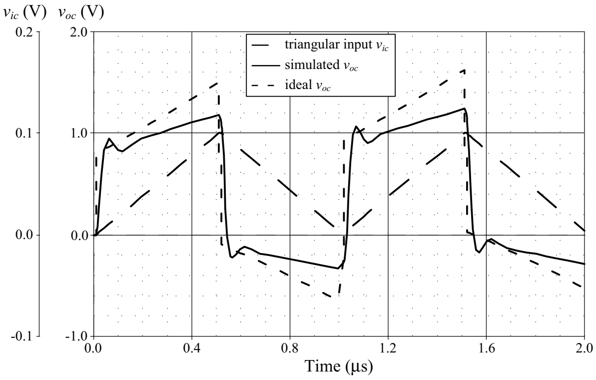

Figure 5: Time-domain responses of the proposed PID controller

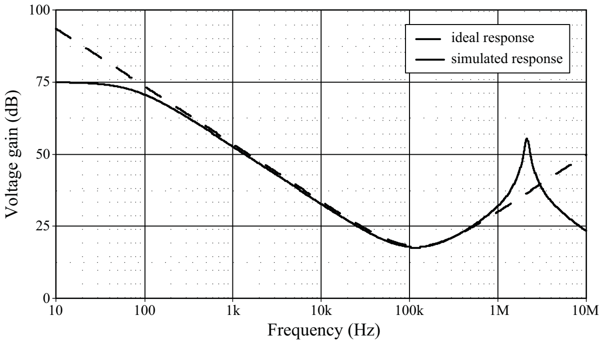

Figure 6: Frequency-domain responses of the proposed PID controller

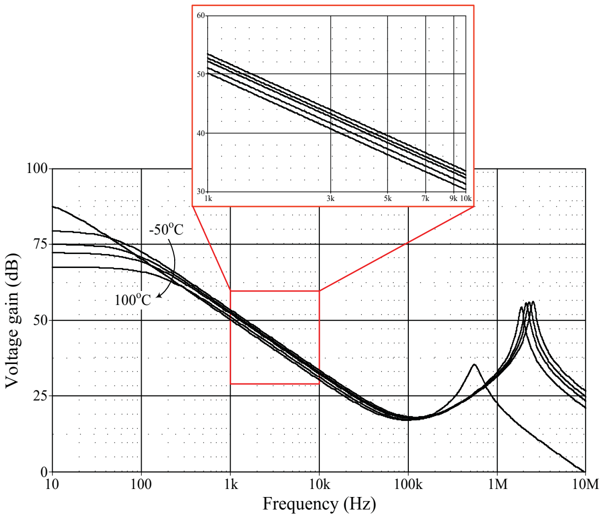

Figure 7: Frequency-domain responses of the proposed PID controller at temperature ranges -50°C, 0°C, 27°C, 50°C, and 100°C.

Additionally, the temperature-dependent variation of the frequency-domain responses of the proposed PID controller analysis was performed at industrial ranges T = -50°C, 0°C, 27°C, 50°C, and 100°C. The simulation results of the industrial temperature analysis are given in Fig.7, where it can be observed that the gain characteristic of the controller diminishes with increasing temperature.

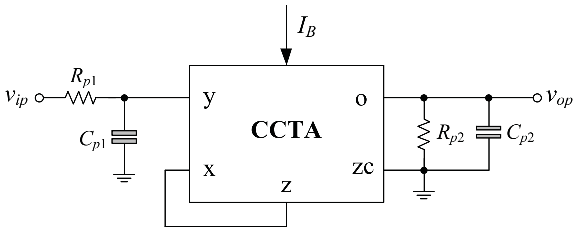

Figure 8: Single CCTA-based lowpass filter using only grounded capacitors

For the performance evaluation of the proposed PID controller circuit in Fig.2, a voltage-mode lowpass filter using a single CCTA and four passive elements is realized as shown in Fig. 8. The voltage transfer function of the filter with $R_{p2} = 1/g_m$ is given by

$$G_p(s) = \frac{V_{op}(s)}{V_{ip}(s)} = \frac{\left(\dfrac{g_m}{R_{p1}C_{p1}C_{p2}}\right)}{s^2 + s\left[\dfrac{g_m(R_{p1}C_{p1} + C_{p2})}{R_{p1}C_{p1}C_{p2}}\right] + \left(\dfrac{g_m}{R_{p1}C_{p1}C_{p2}}\right)} \tag{33}$$

where the pole frequency (ω_p) and the quality factor (Q) are derived as:

$$f_p = \frac{\omega_p}{2\pi} = \frac{1}{2\pi}\sqrt{\frac{g_m}{R_{p1}C_{p1}C_{p2}}} \tag{34}$$

and

$$Q = \left(\frac{1}{R_{p1}C_{p1} + C_{p2}}\right)\sqrt{\frac{R_{p1}C_{p1}C_{p2}}{g_m}} \tag{35}$$

The negative feedback system has been given to evaluate the practical ability of the proposed PID controller circuit. The block diagram of the closed-loop system is represented in Fig.9. In the study that follows, the step response of the system is analyzed to observe the effect of the proposed controller on this system. For the lowpass filter in Fig. 8, the component values were set as follows: g_m = 0.61 mA/V, R_{p1} = 1 kΩ, R_{p2} = 1.5 kΩ, and $C_{p1} = C_{p2}$ = 1 nF, giving f_p = 124.3 kHz and Q = 1.28. Fig.10 shows the ideal and simulated transient responses of $e(t)$ and $u(t)$ for the closed-loop system in Fig.9 with the ramp input voltage $v_{in}(t)$ rising time of 3 µs/100 mV. The overall power consumption of the closed-loop system in Fig.9 is estimated to be 108 mW predicated on simulations.

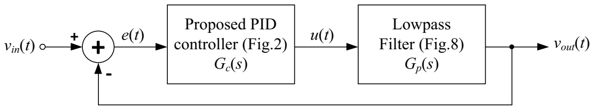

Figure 9: Feedback control system to evaluate the performance of the proposed PID controller.

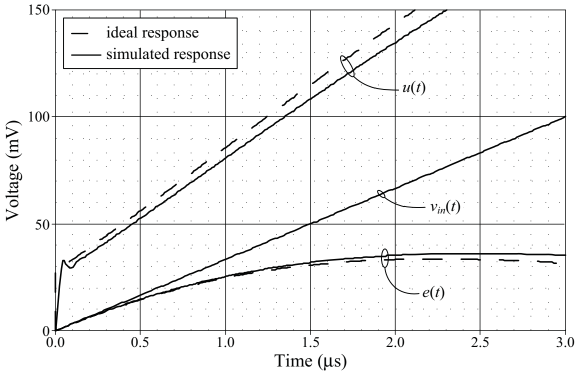

Figure 10: Ramp-input responses of $e(t)$ and $u(t)$ for the closed-loop system in Fig.9.

In addition to observing the step response of the system, a step input with amplitude of 100 mV was applied, and the obtained results are displayed in Fig.11. These results are provided to demonstrate the transient response characteristics of the system for four different values of the tuning controller gain parameters. The first set of gain parameters in Fig.11(a) for case 1 were K_P = 1.9, K_I = 0.86 Ms, and K_D = 1 µs with g_m = 0.86 mA/V, $R_1 = R_2$ = 5 kΩ, and $C_1 = C_2$ = 1 nF. The second parameters in Fig.11(b) were modified to K_P = 6.9, K_I = 1.9 Ms, and K_D = 5 µs by selecting g_m = 0.38 mA/V, R_1 = 1 kΩ, R_2 = 5 kΩ, and $C_1 = C_2$ = 1 nF for case 2. The gain parameters in case 3 of Fig.11(c) were K_P = 8, K_I = 3 Ms, and K_D = 5 µs with g_m = 0.61 mA/V, R_1 = 1 kΩ, R_2 = 5 kΩ, and $C_1 = C_2$ = 1 nF. For case 4, the gains in Fig.11(d) were K_P = 13.6, K_I = 8.6 Ms, and K_D = 5 µs by setting g_m = 0.86 mA/V, R_1 = 1 kΩ, R_2 = 5 kΩ, C_1 = 1 nF, and C_2 = 0.5 nF.

4 Experimental results

In experimental measurements, the CCTA has been practically constructed with commercially available ICs such as AD844s [26] and CA3080 [27], as depicted in Fig.12. In this case, the CCTA's transconductance gain (g_m) is proportional to the external bias current (I_B) and has the following relationship: $g_m = 20I_B$ [27]. The symmetrical bias voltages of the AD844s and CA3080 were set at ±5V. Also, for the laboratory testing circuit, the active and passive elements were chosen as g_m = 0.86 mA/V (I_B = 43 µA), $R_1 = R_2$ = 5 kΩ, and $C_1 = C_2$ = 1 nF,

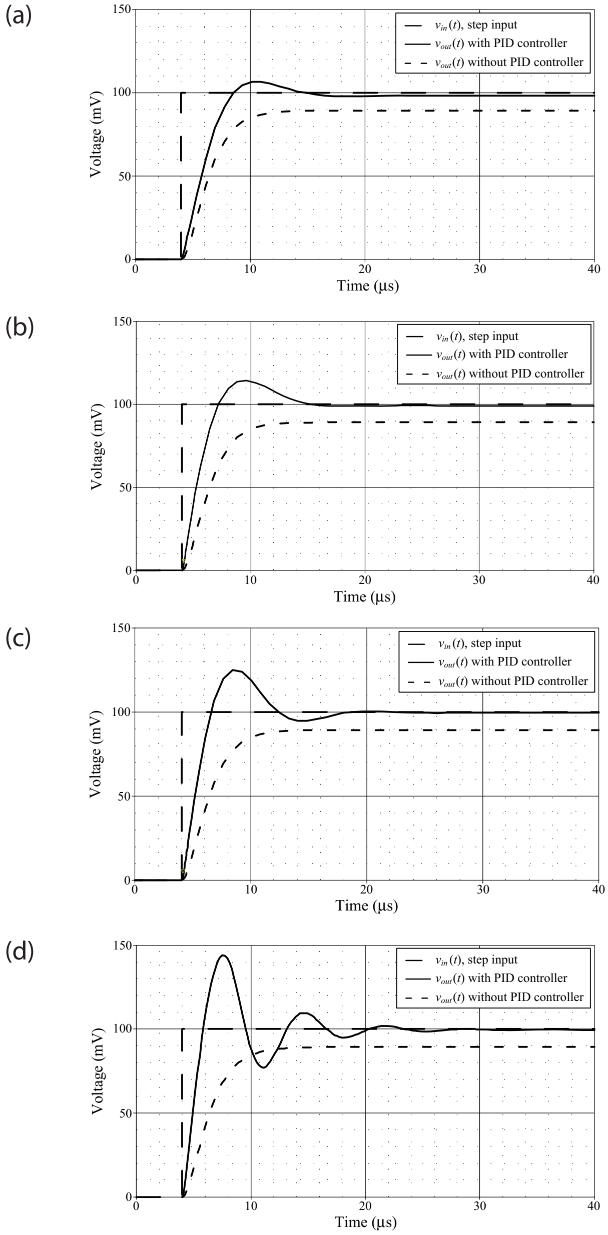

Figure 11: Simulated step-input response characteristics of the closed-loop system in Fig.9. (a) Case 1; (b) Case 2; (c) Case 3; (d) Case 4

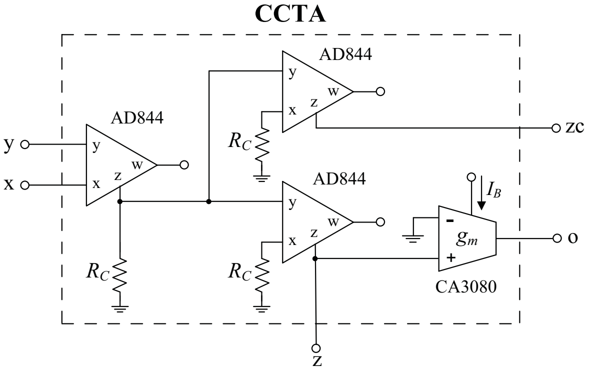

Figure 12: Practical CCTA implementation using readily available ICs AD844s and CA3080.

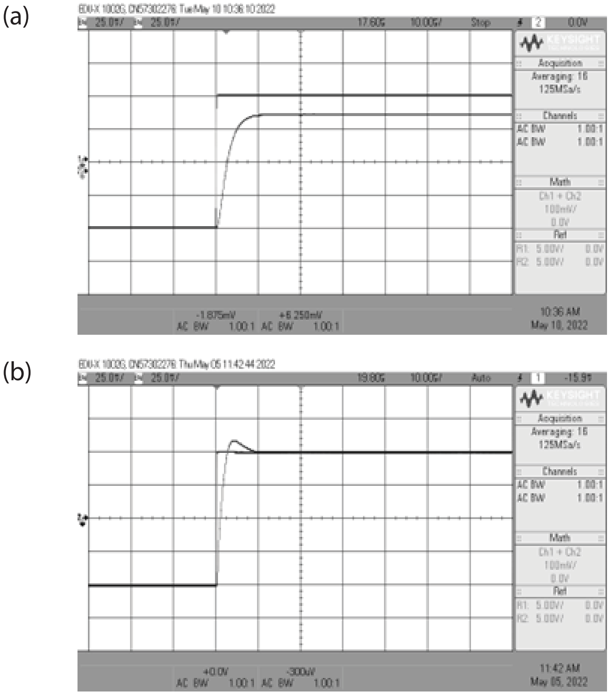

Figure 13: Measured step responses of the closed-loop system in Fig.9 for case 1. (a) without PID controller; (b) with PID controller

which leads to $K_P = 1.9$, $K_I = 0.86$ Ms, and $K_D = 1$ μs as in case 1. A step input voltage with amplitude of 100 mV was applied to the input of the experimental test circuit. Fig.13 shows the measured input voltage and associated output waveforms for the uncontrolled filter $v_{op}(t)$ and the controlled filter $v_{out}(t)$.

To evaluate the impact of the proposed PID controller on the step response of the closed-loop system in Fig.9, the measured transient responses for three different controller gains are given in Fig.14. The experimental test results were obtained using the same component settings as in simulation verification, namely case 2, case 3, and case 4. From Figs.13 and 14, the performance comparison in terms of delay time (t_d), rise time (t_r), peak time (t_p), peak output (p_o), maximum overshoot (M_p), and settling time (t_s) are also measured and summarized in Table 3. As observed in Table 3, the use of the proposed PID controller clearly improves the system's performance in the desired manner.

On the other hand, the ideal, simulated and measured frequency-domain responses of the closed-loop system in Fig.9 for the four mentioned cases of the controller gain values are given in Fig.15. The experimental results validate the ideal responses within the working range of the proposed PID controller. Nevertheless, the slight deviation in these responses is mostly due

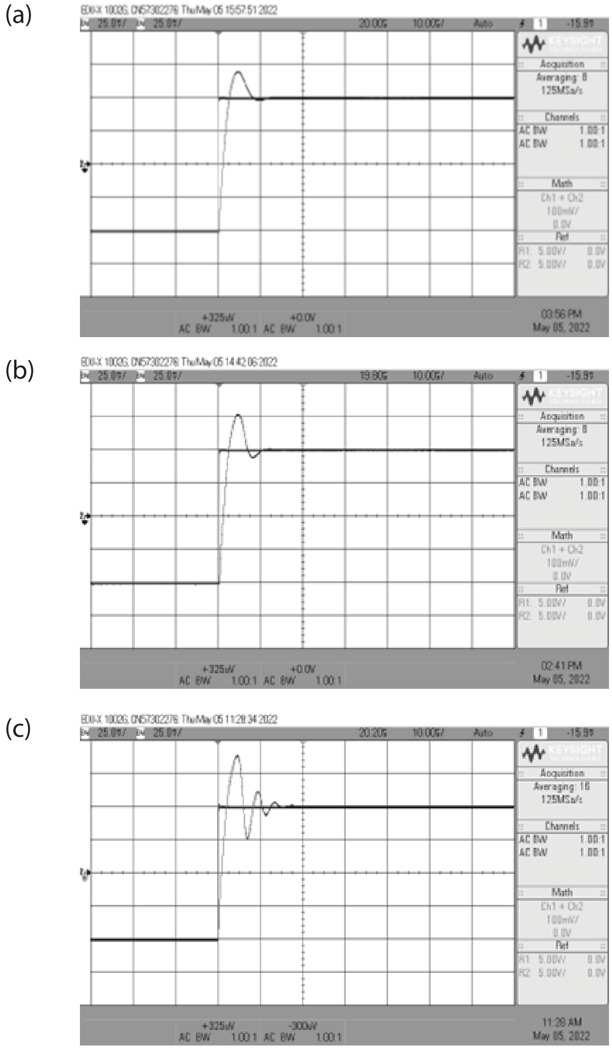

Figure 14: Measured step responses of the closed-loop system in Fig.9 with variable controller gains. (a) Case 2; (b) Case 3; (c) Case 4

to the non-ideal characteristics of AD844s and CA3080 in Fig.12, such as non-ideal transfer gains and parasitic impedances. Some techniques [28]-[29] that reduce non-ideal transfer gains and parasitic elements can be used to minimize the difference between ideal and measured responses.

5 Conclusions

This paper suggests a novel voltage-mode PID controller based on CCTA. A single CCTA, two resistors, and two capacitors are used in the suggested circuit. Because all of the passive components in this realization are grounded, it is ready for further integration. The implementation does not need element-matching requirements and can be simply accomplished using commercially available integrated circuits. The controller gain parameters K_P, K_I, and K_D are all adjustable. An application example of the proposed PID controller as the closed-loop system is included. The analysis of the theoretically proposed circuit has been validated through simulation findings and experimental test results.

6 Acknowledgments

This work was supported by Rajamangala University of Technology Rattanakosin (RMUTR). The support by School of Engineering, King Mongkut's Institute of Technology Ladkrabang (KMITL), is also gratefully acknowledged.

7 Conflict of Interest

The authors confirm that this article content has no conflict of interest.

Table 3: Comparison of the performance of the uncontrolled filter and the controlled filter

Parameter	Uncontrolled filter	Controlled filter with proposed PID controller			
		Case 1: $K_P = 1.9$, $K_I = 0.86$ Ms, $K_D = 1$ μs	Case 2: $K_P = 6.9$, $K_I = 1.90$ Ms, $K_D = 5$ μs	Case 3: $K_P = 8$, $K_I = 3$ Ms, $K_D = 5$ μs	Case 4: $K_P = 13$, $K_I = 8.6$ Ms, $K_D = 5$ μs
t_d (μs)	2.6	1.0	1.2	1.0	1.2
t_r (ns)	12.4	2.4	2.6	2.2	2.2
t_p (μs)	12.4	4.0	4.6	4.4	4.4
p_o (mV)	87	107.8	118.75	125.95	137.82
M_p (%)	0	7.8	18.75	25.95	37.82
t_s at 2% (μs)	10	7.0	9.8	9.4	13.6
t_s at 5% (μs)	8.2	5.6	7.0	8.4	11.6

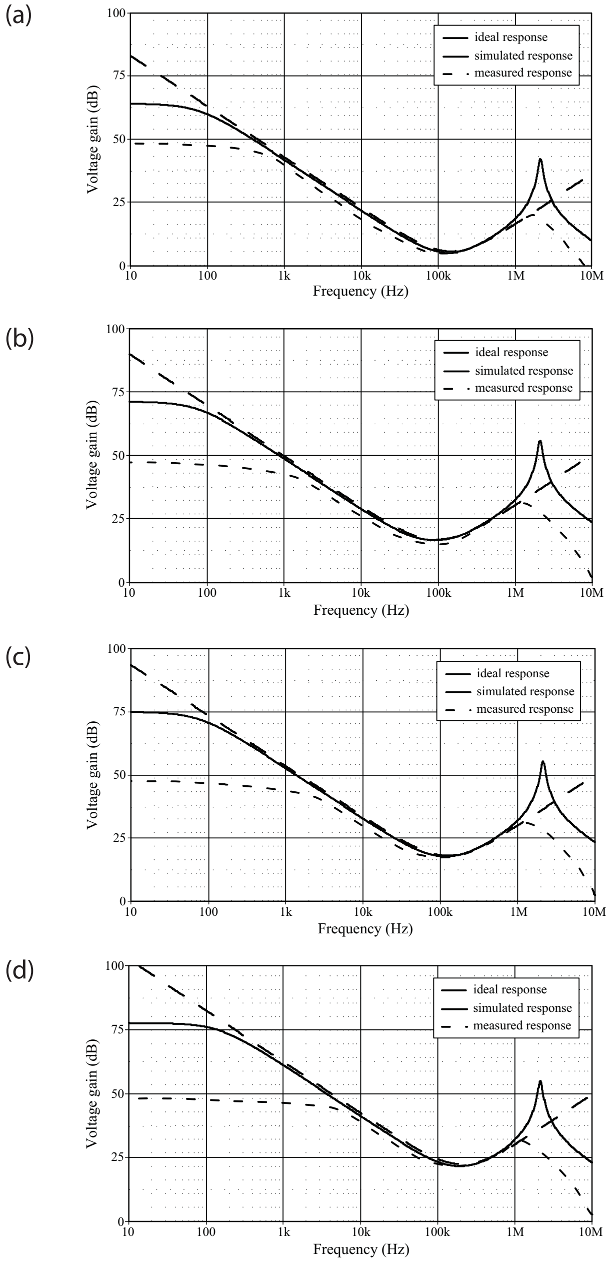

Figure 15: Frequency-domain performance of the closed-loop system in Fig.9 with variable controller gains. (a) Case 1; (b) Case 2; (c) Case 3; (d) Case 4

8 References

1. K. Astrom, and T. Hagglund, "PID controllers: theory, design and tuning, 2nd edition," North Carolina, Instrument Society of America, 1995.
2. S. Bennette, "Development of the PID controller," *IEEE Control Syst.*, vol. 13, no. 6, pp. 58–62, 1993, https://doi.org/10.1109/37.248006
3. C. Erdal, A. Toker, and C. Acar, "OTA-C based proportional-integral-derivative (PID) controller and calculating optimum parameter tolerances," *Turk. J. Elec. Eng. Comp. Sci.*, vol. 9, no. 2, pp. 189-198, 2001.
4. C. Erdal, A. Toker, and C. Acar, "A new proportional-integral-derivative (PID) controller realization by using current conveyors and calculating optimum parameter tolerances," *Istanb. Univ.-J. Electr. Electron. Eng.*, vol. 1, pp. 267-273, 2001.
5. E. Yuce, S. Tokat, A. Kizilkaya, and O. Cicekoglu, "CCII-based PID controllers employing grounded passive components," *Int. J. Electron. Commun. (AEU)*, vol. 60, no. 5, pp. 399–403, 2006, https://doi.org/10.1016/j.aeue.2005.03.017
6. C. Erdal, "A Proportional-Integral-Derivative (PID) controller realization by using current feedback amplifiers (CFAs) and calculating optimum parameter tolerances," *Pak. J. Appl. Sci.*, vol. 2, no. 1, pp. 56–59, 2001, https://doi.org/10.3923/jas.2002.56.59
7. M. Sagbas, M. Koksal, and U. E. Ayten, "Design of dominantly proportional PID controller using a single commercially available active component," in *Proc. Int. Conf. Telecom. Signal Process.*, Italy, 2013, pp. 427–430, https://doi.org/10.1109/TSP.2013.6613967
8. U. E. Ayten, E. Yuce, and S. Minaei, "A voltage-mode PID controller using a single CFOA and only grounded capacitors," *Microelectron. J.*, vol. 81, pp. 84–93, 2018, https://doi.org/10.1016/j.mejo.2018.09.010
9. Z. G. C. Taskiran, H. Sedef, and F. Anday, "A new PID controller circuit design using CFOAs," *Circ. Syst. Sig. Process.*, vol. 40, no. 3, pp. 1166–1182, 2021, https://doi.org/10.1007/s00034-020-010540-5
10. A. U. Keskin, "Design of a PID controller design employing CDBAs," *Int. J. Electr. Eng. Educ.*, vol. 43, no. 1, pp. 48–56, 2006, https://doi.org/10.7227/ijeee.43.1.5
11. P. Shrivastava, S. Surendra, R. K. Ranjan, A. Shrivastav, and B. Priyadarshini, "PI, PD and PID controllers using single DVCCTA," *Iranian J. Sci. Tech. Trans. Electr. Eng.*, vol. 43, no. 3, pp. 673–685, 2019, https://doi.org/10.1007/s40998-019-00180-z
12. W. Tangsrirat, "Voltage-mode analog PID controller using a single z-copy current follower transconductance amplifier (ZC-CFTA)," *Informacije MIDEM*, vol. 45, no. 3, pp. 175–179, 2015.
13. E. Ozer, "Design of voltage-mode PID controller based on current follower transconductance amplifiers," in *Proc. Global Conf. Eng. Research*, Turkey, 2021, pp. 165–178.
14. D. Prasad, M. Srivastava, Laxya, F. Jabin, G. Fatima, S. A. Khan, and S. Tanzeem, "Novel active PID controller employing VDTA," in *Proc. 2016 IEEE Int. Symp. Sig. Process. Inform. Tech. (ISSPIT)*, Limassol, Cyprus, 2016, pp. 286–289, https://doi.org/10.1109/ISSPIT.2016.7886050

15. E. Ozer, and F. Kacar, "Design of voltage-mode PID controller using a single voltage differencing current conveyor (VDCC)," *Analog Inte. Circ. Sig. Process.*, vol.109, no. 1, pp. 11-27, 2021, https://doi.org/10.1007/s10470-021-01880-5
16. E. Ozer, A. Sayin and F. Kacar, "Voltage-mode PID controller design employing canonical number of active and passive elements," *Analog Inte. Circ. Sig. Process.*, 2022, https://doi.org/10.1007/s10470-022-02057-4
17. R. Prokop, and V. Musil, "New modern circuit block CCTA and some its applications," in *Proc. 14th Int. Scientific Appl. Sci. Conf. – Electronics, Book 5, Sofia*, 2005, pp. 93–98.
18. J. Budboonchu, T. Pukkalanun, and W. Tangsrirat, "Resistorless voltage-mode first-order allpass section using single current-controlled conveyor transconductance amplifier," *Indian J. Pure & Appl. Phys.*, vol. 53, no. 5, pp. 335–340, 2015.
19. N. Herencsar, J. Koton, and K. Vrba, "Single CCTA-based universal biquadratic filters employing minimum components," *Int. J. Comp. Electr. Eng.*, vol. 1, no. 3, pp. 307–310, 2009, https://doi.org/10.7763/ijcee.2009.v1.48
20. N. Pandey, S. Kapur, P. Arora, and S. Malhotra, "Novel voltage mode multifunction filter based on current conveyor transconductance amplifier," *ACEEE Int. J. Contr. Syst. Instrum.*, vol. 2, no. 1, pp. 42–45, 2011.
21. W. Tangsrirat, O. Chunnumsin, and T. Pukkalanun, "Single-current-controlled sinusoidal oscillator with current and voltage outputs using single current-controlled conveyor transconductance amplifier and grounded passive elements," *Rev. Roum. Des Sci. Techn.-Électrotechn. et Énerg*, vol. 60, no. 2, pp. 175–184, 2015.
22. W. Tangsrirat, "Dual-mode sinusoidal quadrature oscillator with single CCTA and grounded capacitors," *Informacije MIDEM*, vol. 46, no. 3, pp. 130–135, 2016.
23. W. Tangsrirat, "Simple BiCMOS CCCTA design and resistorless analog function realization," *The Scientific World Journal*, vol. 2014, Article ID 423979, 7 pages, 2014, https://doi.org/10.1155/2014/423979
24. A. Verma, S. K. Rai, and M. Gupta, "High frequency meminductor emulator using current conveyor transconductance amplifier and memristor," in *Proc. 2021 8th Int. Conf. Sig. Process. Integr. Network (SPIN)*, 2021, pp. 720–725, https://doi.org/10.1109/SPIN52536.2021.9566098
25. K. Ogata, *Modern Control Engineering*, 5th ed. Prentice-Hall, New Jersey, 2010.
26. Analog Devices, "60 MHz, 2000 V/μs, monolithic op amp with quad low noise," AD844 datasheet, 1992.
27. Harris Semiconductor. 2 MHz, Operational Transconductance Amplifier (OTA). CA3080 datasheet; 1996.
28. E. Yuce, "Negative impedance converter with reduced non-ideal gain and parasitic impedance effects," *IEEE Trans. Circuits Syst. I- Reg. Paper*, vol. 55, no. 1, pp. 276–283, 2008. https://doi.org/10.1109/tcsi.2007.913702
29. S. Minaei, and E. Yuce, "A simple CMOS-based inductor simulator and frequency performance improvement techniques," *Int. J. Electron. Commun. (AEU)*, vol. 66, no. 11, pp. 884–891, 2012. https://doi.org/10.1016/j.aeue.2012.03.005

Arrived: 21. 05. 2022
Accepted: 03. 09. 2022

Original scientific paper
https://doi.org/10.33180/InfMIDEM2022.304

Informacije MIDEM
Journal of Microelectronics,
Electronic Components and Materials
Vol. 52, No. 3(2022), 181 – 189

Energy Efficient and Low dynamic power Consumption TCAM on FPGA

Sridhar Raj Sankara Vadivel, Shantha Selvakumari Ramapackiam

Department of ECE, Mepco Schlenk Engineering College, Sivakasi, Tamilnadu, India

Abstract: Ternary Content Addressable Memories [TCAM] based on Field Programmable Gate Arrays [FPGA] are widely used in artificial intelligence [AI] and networking applications. TCAM macros are unavailable within the FPGA; therefore, they must be emulated using SRAM-based memories, which require FPGA resources. Compared to state-of-the-art designs, the proposed FPGA-based TCAM implementation will save significant resources. This methodology makes use of the Lookup Table RAMS (LUTRAMs), slice carry-chains, and flip-flops (FF) allowing simultaneous mapping of rules and deeper pipelining respectively. The TCAM implementation results in lower power consumption, fewer delays and lower resource utilization. It outperforms conventional FPGA-based TCAMs in terms of energy efficiency (EE) and performance per area (PA) by at least 3.34 and 8.4 times respectively, and 56% better than existing FPGA designs. The proposed method outperforms all previous approaches due to its low dynamic power consumption when considering the huge size of TCAM emulation on SRAM-based FPGAs.

Keywords: TCAM; Software Defined Networking; Artificial intelligence; Networking; Quality of Service (QoS)

Energetsko učinkovit TCAM na FPGA z nizko dinamično porabo energije

Izvleček: Ternarni vsebinsko naslovljivi pomnilniki [TCAM], ki temeljijo na poljskih programirljivih matrikah [FPGA], se pogosto uporabljajo v aplikacijah umetne inteligence [AI] in omrežnih aplikacijah. Makroji TCAM niso na voljo v FPGA, zato jih je treba emulirati s pomnilniki na osnovi SRAM, ki zahtevajo vire FPGA. V primerjavi z najsodobnejšimi zasnovami bo predlagana implementacija TCAM na osnovi FPGA prihranila precej virov. Ta metodologija uporablja pomnilnike RAM s preglednicami za iskanje (LUTRAM), prenosne verige in flip-flope (FF), ki omogočajo hkratno preslikavo pravil oziroma poglobljeno vodenje. Izvedba TCAM omogoča manjšo porabo energije, manjše zakasnitve in manjšo izkoriščenost virov. V smislu energetske učinkovitosti (EE) in zmogljivosti na površino (PA) presega običajne TCAM-e na osnovi FPGA za vsaj 3,34- oziroma 8,4-krat in je za 56 % boljša od obstoječih zasnov FPGA. Predlagana metoda presega vse prejšnje pristope zaradi nizke dinamične porabe energije ob upoštevanju ogromne velikosti emulacije TCAM na FPGA na osnovi SRAM

Ključne besede: TCAM; programsko definirano omrežje; umetna inteligenca; omrežje; kakovost storitev (QoS)

** Corresponding Author's e-mail: sridhars@mepcoeng.ac.in, rshantha@mepcoeng.ac.in*

1 Introduction

Artificial intelligence (AI) is speeding up and becoming more accurate and reliable. The centralized server is used to connect applications from the edge to the cloud. Due to the rapid growth of internet-connected devices and an increase in internet traffic, today's systems require very fast searches. For IP routing and Internet Protocol (IP) forwarding, routers are key components of networking equipment. Routers receive a packet of data and decide where to route it. They must provide fast packet routing by searching through large amounts of data. High-speed searches are also required in CPUs, database engines, and neural networks.

The latest Xilinx and Intel FPGA chips are increasingly being used as data plane accelerators for Software Defined Networking (SDN) [1]. The FPGA industry continually launches software development toolkits to process and classify packets quickly and efficiently [2]. Ethernet/IP forwarding, firewalls, and QoS (Quality of Service) require packet processing and classification. There are three types of matching techniques used in

How to cite:
S. R. S. Vadivel et al., "Energy Efficient and Low dynamic power Consumption TCAM on FPGA", Inf. Midem-J. Microelectron. Electron. Compon. Mater., Vol. 52, No. 3(2022), pp. 181–189

classification. They are Longest Prefix Matching (LPM) [3], Matching with Wildcards [4], and Exact Matching (EM) [5]. Matching with wildcards is the most challenging task.

Switching, Routing, QoS tables and Access Control List (ACL) are all stored in a high-speed memory to allow for forwarding decisions and limits. These memories (lookups) contain information about results, such as whether a packet with a particular destination IP address should be dropped according to an ACL. Cisco Catalyst switches use specialized memory architectures, called CAMs and TCAMs, to store these memory tables.

2 Related works

Content Addressable Memories (CAM) [6] deal only with the binary digits (0's and 1's), whereas the Ternary Content Addressable Memories (TCAM) deal with (0's, 1's, and x), where "x" represents Don't care. TCAMs are not available inside the FPGAs as they must be emulated using memory and logic resources and this leads to a significant resource overhead. Researchers have consequently been working on reducing the resource consumption of FPGA-based TCAMs. TCAMs are made up of three basic parts: storage memory, a priority encoder, and match logic. A major cost component of FPGAs based on SRAM is their storage memories, which comprise the actual TCAM contents to be searched. Bosshart et al. [7] optimize the storage memory needs of TCAMs by combining dual-output LUTs and partial reconfiguration. This saves many storage memory resources.

Match logic generates a flag for each incoming key, and this consumes a significant amount of resources because it must be done simultaneously for all memory locations at high speed. Ullah et al. [8] propose a novel idea for efficiently mapping the matching logic in Xilinx FPGAs by exploiting the built-in carry-chain resources. As the size of the key and rules to be stored in the TCAM increases, the storage and matching logic requirements increase as well. As a result, it is worth looking into optimizing both storage and matching logic resources at the same time.

TCAM emulation on SRAM-based FPGAs has been examined using four types of resources: block RAMs (BRAMs), LUT RAMs (LUTRAMs), lookup tables (LUTs), and flip-flops (FFs). Slice FFs is used as TCAM storage memory in FF-based TCAMs [9] – [12]. Because each FF holds a single bit of data and the architectural limitations require the use of a LUT–FF pair, many of the LUTs will be used as pass-through, wasting resources. Researchers [13], [14], and [15–21] have extensively investigated BRAM-based TCAM emulation using SRAM-based FPGA. However, the efficient use of BRAM for TCAM emulation is restricted by theoretical limits, which require at least an SRAM/TCAM bit ratio of $2^9/9$ and, when contrasted to LUTRAM or LUTs based TCAMs, which requires $2^6/6$ [22], or 5 × more.

Reviriego et al. [23] used 5 × 2 LUTs to emulate TCAMs as well as modern SRAM-based FPGAs with their reconfiguration capabilities for storing and updating TCAM rules. Compared to PR-TCAM [23], BPR-TCAM [8] uses a slice built-in carry-chain to reduce matching logic in TCAMs. Both approaches rely on partial reconfiguration for updating TCAM stored rules. Another resource for TCAM-emulation, in addition to LUTRAM, is distributed RAM [22], [24], [25]. Ullah et al. [21] used distributed RAMs in a 6 × 1 configuration for resource allocation in the same slice to obtain greater performance per area (PA), in addition to using carry chains for the match-logic reduction.

The D-TCAM [26] structure uses LUTRAMs on a 6 × 1 Xilinx template to store TCAMs and pipeline fine-grain by using its built-in slice register to gain higher throughput (TP). The previous work using the LUTRAMS in the 5 x 2 configuration and all of the FFs in the SLICEM were used to improve the throughput and performance per area.

To implement broader TCAM words, the partial match results must be transferred from the current slice's carry chain to the next slice's carry chain [24]. By utilizing the TCAM ANDing logic in the carry-chain, it is possible to achieve the desired TCAM bit density while saving a significant amount of LUT resources. It increases area performance by at least 67 percent and energy efficiency by at least 2.5 times. Frac-TCAM [27] utilizes RAM32M to construct the 8 × 5 TCAM compared to 4 × 6 TCAM used in DURE, thus almost doubling the utilization density. Moreover, LUTRAM outputs can be pipelined via in-slice registers. In comparison to existing approaches, logic utilization and TP can be enhanced, resulting in improved PAs.

By combining BRAM and LUTRAM, Comp-TCAM [28] can implement the TCAM architecture regardless of the type of memory and can be adapted to meet the system requirements. A decrease of 41.6% in hardware resource utilisation has no effect on the functionality.

In this paper, a TCAM emulation on Xilinx SRAM-based FPGAs to achieve a storage reduction in LUTRAMs and a match reduction in logic resources is presented. To accelerate the arithmetic operations, the match bits from the distributed RAMs are efficiently AND-cascaded using the FPGA's built-in carry chains. Ullah et al. [8] used only one built-in carry-logic for matching one of the rules. The proposed work used only one built-in carry logic for matching two of the rules (i.e)., dual-output LUTs are connected to the two built-in carry logic compared to LH-CAM [10]. It is capable of mapping a single output LUTRAM matching logic. This makes the delay time shorter and the design clock rate faster because it doesn't use any logic or routing resources.

The main contributions of the paper are listed below:

1. An FPGA resource-saving TCAM emulation scheme has been proposed that significantly reduces the resources needed to emulate an individual TCAM.
2. The mapping of two rules using dual-output LUTs and then using the built-in carry-chain to implement the match logic. Thus, additional logic or routing resources are not required for the matching logic. This reduces the delay time and achieves a high clock speed.
3. TCAM is designed to be scalable in terms of lookup rate, power consumption, device utilization, and energy-efficiency.

3 Proposed TCAM architecture

Consider the TCAM emulation on SRAM-based FPGAs. For example, N = 4 and W = 4, i.e., a 4 × 4 TCAM, where W denotes the key size or width, and depth is denoted by N. The key size is 4, and each 4 × 1 SRAM has two input address lines. The TCAM can be divided into two blocks, as shown in Fig.1 and each of the four rules r0, r1, r2, and r3 is mapped to a 4 × 1 SRAM. The top block is indexed by b0 and b1, whereas the bottom block is indexed by b2 and b3. The outputs of the SRAM are combined using AND gates known as match logic. The choice of SRAM implementation primitives, as well as its width and depth extension, is essential to the efficient TCAM designs on FPGA.

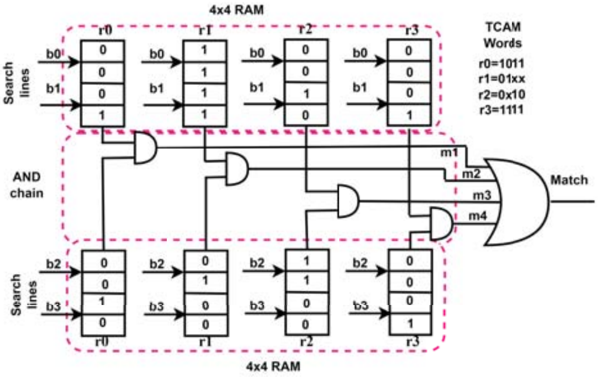

Figure 1: TCAM emulation using SRAMs.

The proposed TCAM makes use of the distributed LUTRAM and carry-chain logic present in the SLICEM of Xilinx FPGAs. Consider a 2 × 5 LUT and carry chain as shown in Fig. 2, which has a key width of five and two rules, i.e., O5 and O6.

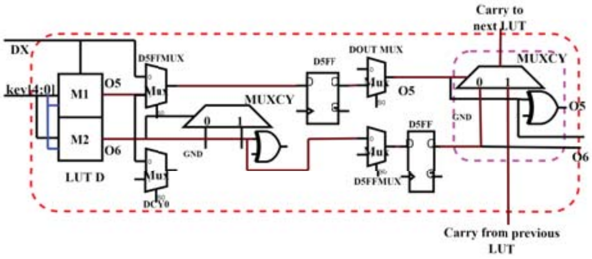

Figure 2: An architecture for mapping a LUT to a carry chain

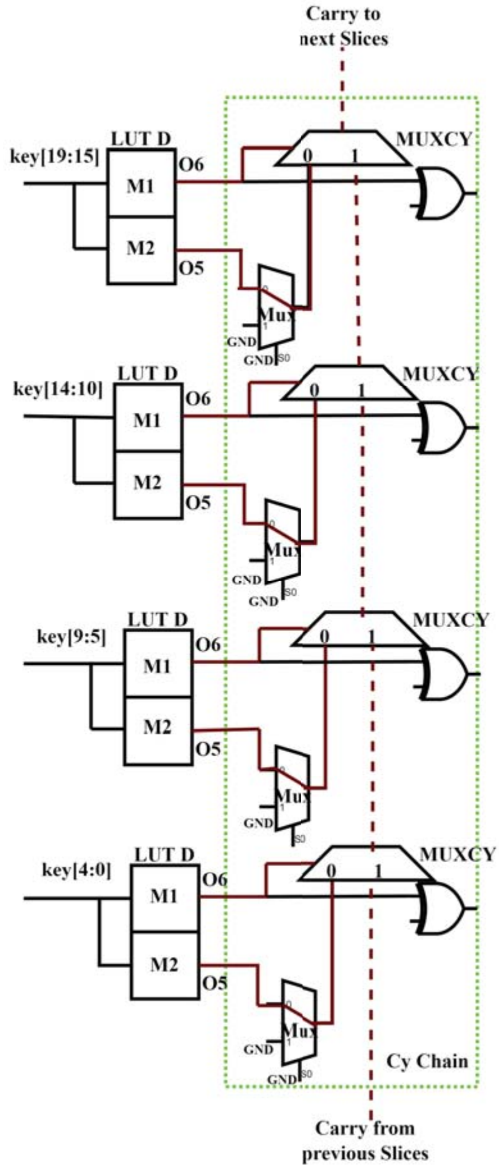

Figure 3: A 1 × 20 TCAM was mapped to from 5 × 2 LUTs

Two rules (Rule 6 and Rule 7) are read from O5 and O6 as the keyword and connected to the 5-bit LUT input (A4:A0). Rule 6 is stored in memory M1, and Rule 7 is stored in memory M2. The rules are updated using the write address inputs as shown in Fig. 2. This LUT output is connected to the built-in carry-chain for implementing the match logic. Note that this is worth mentioning as the proposed TCAM utilized the one carry-chain to reduce the routing resources and extra logic needed, resulting in a higher design clock rate and less delay time.

To implement 1×20 TCAM as shown in Fig.3, LUTs (LUTA, LUTB, LUTC, and LUTD) are stacked with different keywords [19:0] and have eight different rules through O5 and O6. These eight rules are connected to the single carry chain logics i.e., LUT output O6 is connected to the select line of carry-chain logic, and the LUT output O5 is connected to the input of the same carry-chain logic. With the proposed TCAM, six input LUTs in a dual-output mode are combined with eight flip-flops as well as the carry chain in a single slice to provide an 8 × 5 configuration (compared to 4 × 6 for single output LUTs). As shown in Fig. 2, O5 is connected to the select signal of the carry chain through D5FFMUX, D5FF, DOUTMUX and LUT output O6 is connected to the data inputs of the carry chain via DCY0, MUXCY, D5FFMUX and D5FF. In this manner, a fully pipelined TCAM structure is designed, resulting in improved performance such as TP and EDP, while resource utilization is the same as in a non-pipelined structure.

TCAMs with large dimensions can combine multiple basic blocks. To increase the depth of a TCAM, more basic blocks have to be stacked vertically, where each basic block implements a 1 × 20 TCAM. All the basic blocks have the same keyword. As shown in Fig. 4(c), TCAM's width can also be extended by configuring multiple basic blocks with the same depth simultaneously to produce the final match signals.

Fig. 5 shows the proposed TCAM update logic (highlighted in blue dots). The Write Enable "WE" line is short and connected to all the LUTRAM blocks. In the current write cycle, "WE" lines are demultiplexed with the row ID to determine which row needs to be updated. For columns with the same key lines, column update logic takes care of blocks in the same column. Serial shift registers are implemented as SRL32 in SLICEM for column update logic. For the depth varying from 64 to 1024 × 20 columns, only 32 SRL32 is required for implementation. Similarly, for the depth varying from 64 to 1024 × 40 columns, only 64 SRL32 is required for implementation. It is noted that, when the key size is increased from 20 to 40, the SRL32 utilization is doubled. An incoming key value is compared with the 5-bit global counter and the binary value is written into the SRL32. A 3-bit counter is present inside the SRL fill logic that controls the demultiplexer, and it increments once every 33 times the global 5-bit counter.

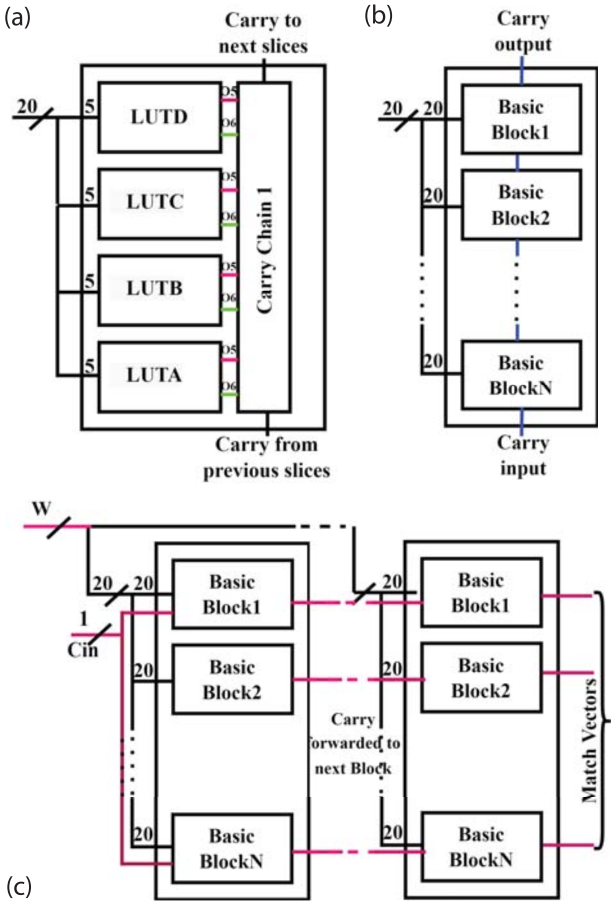

Figure 4: a Architecture of Basic Block combining four LUTs and carry chain into 1 × 20 TCAM; b Depth Extension; c Width Extension

4 Results and discussion

The Xilinx Virtex-7, 28-nm, XC7V2000TFHG1761-2L FPGA device is used to implement the proposed TCAM architecture with a −2 speed grade. There are 1,221,600 LUTs, 344,800 LUTRAMs, 2,443,200 FFs, and 305,400 SLICEs on this device. Performance evaluations of different TCAM sizes are also done using the Vivado HLx 2017.3 design suite. TCAM has a key size of 20 to 160 bits and several rules ranging from 64 to 1024 bits. A SLICE capable of implementing an 8 × 5 TCAM is the fundamental building block. As a result, keys multiply by 5 and rules multiply by 8. The results are based on the implementation of post-place and post-route.

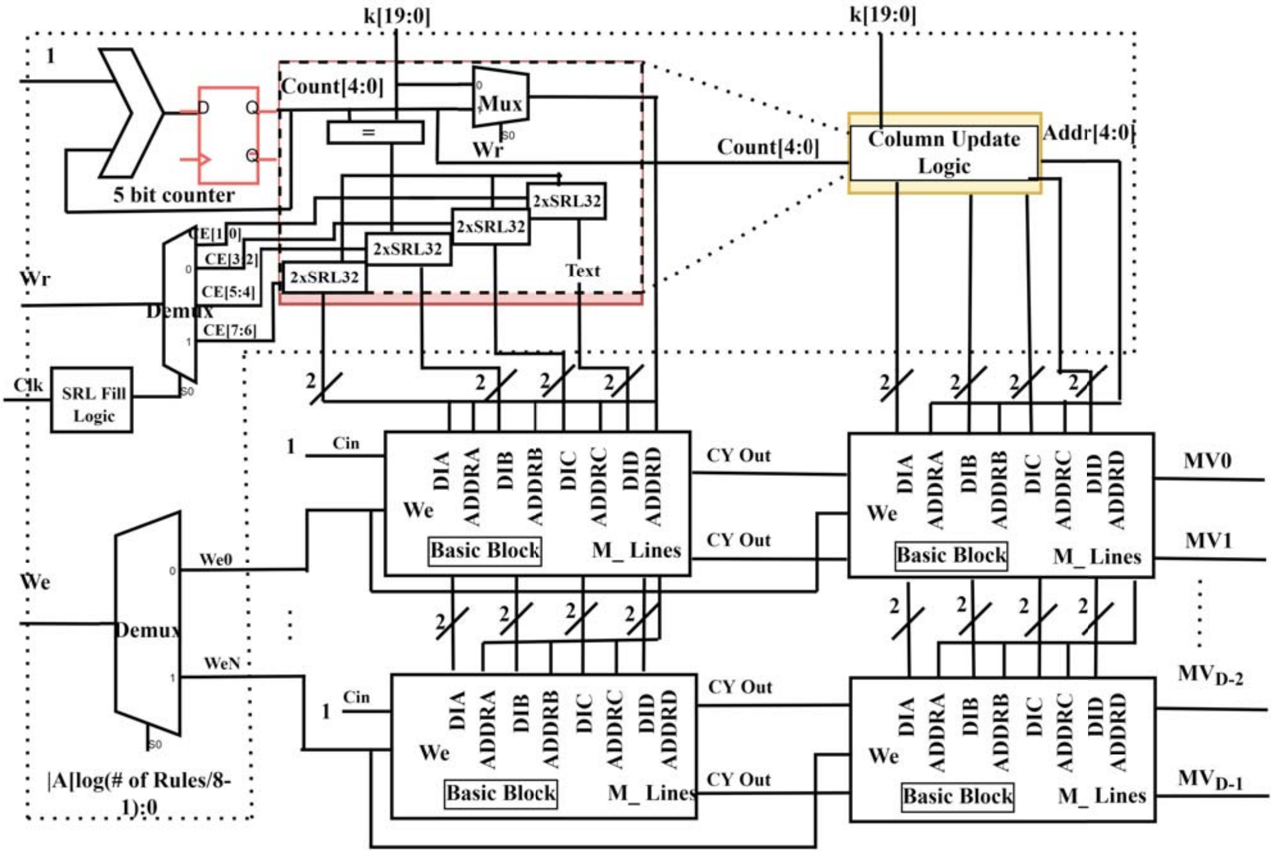

Figure 5: Architecture of the proposed TCAM with update logic.

TCAM storage and update logic resources are required for different configurations, that is, 512 × 20, 512 × 40, 512 × 80, 512 × 160, and 1024 × 160 as mentioned in Table 1. The table shows that the storage part of TCAMs uses a lot more resources than the update logic.

Table 1: Resource Utilization for the proposed TCAM

TCAM Size(D x W)		512 × 20	512 × 40	512 × 80	512 × 160	1024 × 160
TCAM	LUT as logic	0				
	LUT RAM	1024	2048	4096	8192	16384
	FFs	2048	4096	8192	16384	32768
Update Logic	LUT as logic	84	104	144	224	382
	LUT RAM	32	64	128	256	256
	FFs	23	23	23	23	23

Resources utilized for the different TCAM sizes are listed in Table 2, which does not contain a priority encoder or match reduction. The proposed TCAM architecture only utilizes three FPGA resources: LUTRAMs for storing TCAM rules, FFs registers for deeper pipelining, and slice carry chain for match logic. It is important to note that no logic LUTs are needed to implement AND gates since the rules are linked to LUT Carry-chains. Resource utilization can be observed to be directly related to the TCAM's size. It should be noted that the LUT as logic for the entire TCAM will be zero since Match logic can be implemented with the help of the LUT carry chain. As an example, the 64 × 20 TCAM requires 128 LUTRAMs and 256 FF for pipelining, in addition to 32 CARRY4 for data transfer. In the proposed TCAM, FFs and carry chains are used within the same SLICE. FFs are utilized by multiplying the number of blocks by the depth of TCAM. The Virtex-7 FPGA from Xilinx can support eight FFs within a single SLICE. To maximize the utilization of SLICE resources, the proposed TCAM fully exploits the FF available in the SLICE. With this approach, a pipelined TCAM architecture can be implemented without the use of additional SLICEs.

Table 2: Resource Utilization for different Configurations of proposed TCAM

Width	Parameters	Depth			
		64	128	256	512
20	LUT RAM	128	256	512	1024
	FFs	256	512	1024	2048
	Speed(MHz)	888.4	872.8	815.5	752.6
	Power(mW)	4	9	18	34
40	LUT RAM	256	512	1024	2048
	FFs	512	1024	2048	4096
	Speed(MHz)	685.6	680.2	662.5	597.8
	Power(mW)	9	18	34	60
80	LUT RAM	512	1024	2048	4096
	FFs	1024	2048	4096	8192
	Speed(MHz)	642	628	607	584
	Power(mW)	18	34	60	109
160	LUT RAM	1024	2048	4096	8192
	FFs	2048	4096	8192	16384
	Speed(MHz)	567.8	532.8	395.4	372.5
	Power(mW)	34	60	109	122

The speed and dynamic power consumption achieved by the proposed TCAMs shown in Table 2 for the different TCAM configurations. The TCAM inserts registers between the input and the TCAM module, as well as between the TCAM module and the reduction logic. The proposed TCAM achieves speeds from 372 to 888 MHz for different sizes. However, the proposed TCAM degrades minimally as its size increases, and the degradation does not double as the TCAM's size increases. For example, when moving from 64 × 20 to 128 × 20 and from 64 × 160 to 128 × 160, the speed decreases by 15.16 and 35MHz respectively. Similarly, when moving from 64 × 20 to 64 × 40 and from 64 × 80 to 64 × 160, the speed decreases by 202 and 75.1 MHz respectively. In Table 2, TCAMs proposed in this paper scale well with size, when analysing FPGA resource utilization and clock speed. Vivado's power analyser reports these values for default switching activity, after the post-implementation. From the above table it is evident that, as the TCAM size increases, the power consumption also increases. A 64 × 20 configuration consumes 7mW of power dynamically, while a 512 × 160 configuration consumes 122mW.

Table 3 compares the proposed TCAM architecture's in terms of parameters like the normalized slices, normalized speed, PA, TP, update rate, energy per bit, and EDP with state-of-the-art FPGA TCAMs. By using the following equation, the number of normalized slices can be found:

Normalized slices =# of FPGA Slices +
*(# of 36 KBitsBRAMs * 24)* (1)

The normalized speed is calculated to provide a good comparison between different FPGA technology nodes:

$$N\text{speed} = \text{Speed} * \frac{\text{Technology(nm)}}{40\ \text{(nm)}} * \frac{1.0}{VDD} \qquad (2)$$

Throughput (TP), which is another important factor in TCAMs, is calculated with the help of the following equation:

$$\text{TP}\left(\frac{\text{Gbit}}{\text{s}}\right) = F(\text{MHz}) * \text{TCAM Width} \qquad (3)$$

The proposed work has a throughput of 26.64, 50, and 83 Gbit/sec, which is better than the existing work for the TCAM sizes of 512 × 40, 512 × 80, and 512 × 160, as seen in Table 3.

The update rate is defined as the ratio of clock rate (MHz) to the clock cycles, and its unit is a million updates per second (MUPS) as follows:

$$\text{Update rate (MUPS)} = \frac{\text{Clockrate (MHz)}}{\text{clockcycles}} \qquad (4)$$

In the literature, Performance per area (PA), represented mathematically is

$$\text{PA}\left(\frac{\frac{\text{Mbit}}{\text{s}}}{\text{slices}}\right) = \frac{\text{TP(Mbit/s)}}{\frac{N_{Slices}}{TCAM_{\text{Depth}}}} \qquad (5)$$

Table 3: Performance Comparison with the state of the art FPGAs

Architecture	TCAM Size (D×W)	LUTRAMS (#)	Slice Registers (#)	BRAM (36K)	FPGA slices Usage	Speed (MHz)	Tp (Gbits / s)	Search cycles	Delay (ns)	Update rate	PA (/1K)	P (W)	Ebs (fJ/ bit/ search)	EDP (ns.fJ /bit/ search)
Jiang[22]	1024×150^1	20480	37556	0	20526	199	20.9	6	5.03	4.21	1.04	1.9	180	1290
REST [18]	72×28^1	8	390	1	77	50	0.98	5	20	0.07	0.998	0.11	798	22817
HP-TCAM [14]	512×36^2	0	2670	56	1637	118	4.25	5	8.47	0.23	1.045	0.19	102.2	865
G-AETCAM[9]	512×36^2	NA	NA	NA	NA	358	NC	-	2.79	1/358	NC	NC	-	-
RPE-TCAM [29]	512×36^2	NA	NA	NA	NA	319	NC	-	3.13	1/319	NC	NC	-	-
UE-TCAM [17]	512×36^2	0	1758	32	913	202	7.26	2	4.95	0.4	3.16	0.08	42.3	210
Xilinx Locke [30]	256×32^3	4096	341	0	1406	100	5.2	1	10	9.6	1.05	0.09	68	413
Comp-TCAM [28]	512×36^1	1536	-	16	541	525	-	-	-	-	10.8	-	-	-
D-TCAM[26]	512×36^1	NA	NA	0	968	460	16.56	-	2.17	NA	8.76	NA	NA	NA
	512×72^1	NA	NA	0	2357	214	15.41	-	4.67	NA	3.35	NA	NA	NA
	512×144^1	NA	NA	0	4835	259	37.3	-	3.86	NA	3.95	NA	NA	NA
DURE [24]	512×36^2	4096	1174	0	1668	335	12.06	1	2.99	5.15	3.7	0.05	28	84
	$1024 \times 1\,44^2$	32768	2700	0	9654	175	25.2	1	5.72	2.7	2.67	0.48	32.8	187
BPR-TCAM [8]	512×40^1	0	1105	0	768	360	10.08	1	2.78	-	6.72	-	-	-
	512×80^1	0	1185	0	1280	188	12.77	1	5.32	-	2.55	-	-	-
	512×160^1	0	1345	0	2560	114	12.768	1	8.77	-	2.55	-	-	-
	1024×144^2	0	3029	0	4608	111.49	16.05	1	8.97	-	3.57	-	-	-
Frac-TCAM [27]	512×40^1	2048	4096	0	768	588	16.46	1	1.7	15.47	10.98	0.065	-	-
	512×80^1	4096	8192	0	1408	473.9	37.91	1	2.11	17.11	13.79	0.12	-	-
	512×160^1	8192	16384	0	2944	254.8	40.77	1	3.92	9.58	7.09	0.15	-	-
	1024×160^1	16384	32786	0	5888	250	39.95	1	4	9.4	6.95	0.19	-	-
Proposed work	512×40^2	2048	4096	0	598	666	26.64	1	1.5	20.18	22.81	0.034	16.60	24.9
	512×80^2	4096	8192	0	1105	635	50.8	1	1.57	19.24	22.86	0.065	15.87	24.92
	512×160^2	8192	16384	0	2222	524	83.84	1	1.91	15.88	19.32	0.110	13.43	25.65
	1024×40^2	4096	8192	0	1374	563	22.52	1	1.78	17.06	16.78	0.070	17.09	30.42
	1024×80^2	8192	16384	0	2428	532	42.56	1	1.88	16.12	17.95	0.120	15.87	29.84
	1024×160^2	16384	32786	0	4315	421	67.36	1	2.38	12.76	15.99	0.160	11.60	27.60

[1] Virtex-7 (28 nm), [2] Virtex-6 (40 nm), [3] Virtex-5 (65 nm)

PA results in Table 3 show that the suggested TCAM implementation outperforms prior work by a narrow margin. The lower resource usage is due to the search and matching logic. Then, using equation 6, the energy/bit/search (Ebs) is calculated.

$$Energy = \frac{Power\ (W)}{Frequency\ (Hz)\ *\ Depth\ *\ Width} \tag{6}$$

Another important parameter for comparing TCAMs is Energy Delay Product (EDP), which is determined using the following equation:

*Energy Delay Product (EDP)=Energy*Delay* *(7)*

It is observed that the proposed TCAM is 22%, 21%, 24%, and 26% more efficient than Frac-TCAM respectively, for the different TCAM sizes in slice resource utilizations. Compared to state-of-the-art designs, the proposed TCAM has less slice utilization due to slice carry chain utilization. Compared with Frac-TCAM, BPR-TCAM, DURE, D-TCAM, and Comp-TCAM, the proposed TCAM achieves higher clock speed due to inbuilt slice carry chain utilization, SLICEM registers, and RAM32M for the different TCAM sizes.

TCAM size 512 × 40 has a dynamic power consumption of 34mW and a delay time of 1.5 ns. Thus, the energy consumption is 16.60 fJ/bit/search and the EDP is 24.9 ns.fJ/bit/search. The EDP achieved in the proposed work is 3.37 and 8.4 times lower than that of DURE [24] and UE-TCAM [17] respectively, and is the lowest among the various FPGA-based TCAM architectures. TCAM size 1024 × 160 is a larger TCAM that uses 190mW of dynamic power and has a delay time of 2.38ns. Therefore, its EDP is 27.60 ns.fJ/bit/search, almost 46 times less than that of the 150-kbit TCAM implementation in [22]. Thus, the proposed work is also a very energy-efficient TCAM architecture.

5 Conclusion

An FPGA implementation of a TCAM that uses SRAM for higher energy efficiency and resource efficiency is presented. By leveraging the architecture of Xilinx FPGAs, TCAMs can be emulated efficiently. Utilizing LUTRAMs with dual outputs within the latest seven series FPGAs, as well as built-in slice registers and carry chains, a scalable TCAM architecture is proposed. When compared to the conventional 8 × 5 TCAM, the suggested design can map an 8 × 1 TCAM, virtually doubling the utilization density. In addition, the use of in-slice registers to pipeline LUTRAM outputs allows for high-speed operation, and the utilization of carry-chain logic for match reduction archives lower slice utilization. Hence, both logic utilization and TP are enhanced, resulting in a better PA compared with the existing approaches. It achieved an EE and PA that were at least 3.34 and 8.4 times and 56% better than those of the other FPGA-based TCAM solutions, respectively. The large size of TCAM emulation on SRAM-based FPGAs, this solution outperforms the existing solutions with its low dynamic power consumption.

6 Conflict of Interest

The authors declare no conflict of interest.

7 References

1. Zilberman, N. Audzevich, Y. Covington, G.A. Moore, A.W. "NetFPGA SUME: Toward 100 Gbps as Res for the different TCAM sizes in slice resource utilization search Commodity". IEEE Micro 2014, vol. 34, 32–41.
2. Xilinx. "SDNet Packet Processor User Guide UG1012 (v2018.1)", Xilinx: San Jose, CA, USA, 2018.
3. Reviriego, P. Pontarelli, S. Levy, G. "CuCoTrack: Cuckoo filter based connection tracking". Inf. Process. Lett. 2019, vol.147, 55–60.
4. Sundstron, M. Larzon, L. Åke "High-performance longest prefix matching supporting high-speed incremental updates and guaranteed compression". In Proceedings of the 24th Annual Joint Conference of the IEEE Computer and Communications Societies, Miami, FL, USA, 13–17 March 2005 Vol.3, pp. 1641–1652.
5. Yu, F. Katz, R. Lakshman, T. "Efficient Multimatch Packet Classification and Lookup with TCAM". IEEE Micro 2005, vol.25, 50–59.
6. Pagiamtzis, K. Sheikholeslami, A. "Content-Addressable Memory (CAM) Circuits and Architectures: A Tutorial and Survey." IEEE J. Solid-state Circuits 2006, vol.41, 712–727.
7. Bosshart, P. Gibb, G. Kim, S.H. Varghese, G. McKeown, N. Izzard, M. Mujica, F. Horowitz, M. "Forwarding metamorphosis: Fast programmable match-action processing in hardware for SDN". In Proceedings of the Conference of the ACM Special Interest Group on Data Communication (SIGCOMM '13), Hong Kong, China, 12–16 August 2013.
8. A. Ullah, A. Zahir, N. A. Khan, W. Ahmad, A. Ramos, and P. Reviriego, "BPR-TCAM—Block and partial reconfiguration based TCAM on Xilinx FPGAs," Electronics, vol. 9, no. 2, p. 353, 2020.
9. M. Irfan and Z. Ullah, "G-AETCAM: Gate-based area-efficient ternary content-addressable memory on FPGA," IEEE Access, vol. 5, pp. 20785–20790, 2017.
10. Z. Ullah, "LH-CAM: Logic-based higher performance binary CAM architecture on FPGA," IEEE Embedded Syst. Lett., vol. 9, no. 2, pp. 29–32, Jun. 2017.
11. M. Irfan and A. Ahmad, "Impact of initialization on gate-based area efficient ternary content-addressable memory," in Proc. Int. Conf. Comput., Electron. Commun. Eng. (iCCECE), Southend, U.K., Aug. 2018, pp. 328–332
12. H. Mahmood, Z. Ullah, O. Mujahid, I. Ullah, and A. Hafeez, "Beyond the limits of typical strategies: Resources efficient FPGAbased TCAM," IEEE Embedded Syst. Lett., vol. 11, no. 3, pp. 89–92, Sep. 2019.
13. M. Somasundaram, "Circuits to generate a sequential index for an input number in a pre-defined list of numbers," U.S. Patent 7 155 563 B1, Dec. 26, 2006.
14. Z. Ullah, K. Ilgon, and S. Baeg, "Hybrid partitioned SRAM-based ternary content addressable memory," IEEE Trans. Circuits Syst. I, Reg. Papers, vol. 59, no. 12, pp. 2969–2979, Dec. 2012.
15. Z. Ullah, M. K. Jaiswal, and R. C. C. Cheung, "Z-TCAM: An SRAMbased architecture for TCAM," IEEE Trans. Very Large Scale Integr. (VLSI) Syst., vol. 23, no. 2, pp. 402–406, Feb. 2015.

16. Z. Ullah, M. K. Jaiswal, and R. C. C. Cheung, "E-TCAM: An efficient SRAM-based architecture for TCAM," Circuits, Syst., Signal Process., vol. 33, no. 10, pp. 3123–3144, Oct. 2014.
17. Z. Ullah, M. K. Jaiswal, R. C. C. Cheung, and H. K. H. So, "UE-TCAM: An ultra-efficient SRAM-based TCAM," in Proc. TENCON-IEEE Region 10 Conf., Macao, China, Nov. 2015, pp. 1–6.
18. A. Ahmed, K. Park, and S. Baeg, "Resource-efficient SRAM based ternary content addressable memory," IEEE Trans. Very Large Scale Integr. (VLSI) Syst., vol. 25, no. 4, pp. 1583–1587, Apr. 2017.
19. I. Ullah, Z. Ullah, and J.-A. Lee, "Efficient TCAM design based on multipumping-enabled multiported SRAM on FPGA," IEEE Access, vol. 6, pp. 19940–19947, 2018.
20. F. Syed, Z. Ullah, and M. K. Jaiswal, "Fast content updating algorithm for an SRAM-based TCAM on FPGA," IEEE Embedded Syst. Lett., vol. 10, no. 3, pp. 73–76, Sep. 2018.
21. I. Ullah, Z. Ullah, and J.-A. Lee, "EE-TCAM: An energy-efficient SRAM-based TCAM on FPGA," Electronics, vol. 7, no. 9, p. 186, Sep. 2018, https://doi.org/10.3390/electronics7090186
22. W. Jiang, "Scalable ternary content addressable memory implementation using FPGAs," in Proc. Architectures Netw. Commun. Syst., Oct. 2013, pp. 71–82.
23. Reviriego, P. Ullah, A. Pontarelli, S. "PR-TCAM: Efficient TCAM Emulation on Xilinx FPGAs Using Partial Reconfiguration". IEEE Trans. Very Large Scale Integr. Syst. 2019, 27, 1952–1956.
24. Ullah, I. Ullah, Z. Afzaal, U. Lee, J.-A. "DURE: An Energy- and Resource-Efficient TCAM Architecture for FPGAs With Dynamic Updates". IEEE Trans. Very Large Scale Integr. Syst. 2019,vol. 27, 1–10.
25. P. Maidee, "Multiplexer-based ternary content addressable memory," U.S. Patent 9 653 165, May 16, 2017.
26. Irfan, Z. Ullah, and R. C. C. Cheung, "D-TCAM: A high performance distributed RAM based TCAM architecture on FPGAs," IEEE Access, vol. 7, pp. 96060–96069, 2019.
27. Ali Zahir, Shadan Khan Khattak, Anees Ullah , Pedro Reviriego , Fahad Bin Muslim, and Waleed Ahmad "FracTCAM: Fracturable LUTRAM-Based TCAM Emulation on Xilinx FPGAs," IEEE Trans. Very Large Scale Integr. (VLSI) Syst., vol. 28, no. 12, pp. 2726-2730, DEC. 2020
28. Muhammad Irfan, Hasan Erdem Yantır, Zahid Ullah, and Ray C. C. Cheung, "Comp-TCAM: An adaptable composite Ternary content-addressable Memory on FPGAs," IEEE Embedded Systems Letters, Nov. 2021.
29. Irfan, Z. Ullah, M. H. Chowdhury, and R. C. C. Cheung, "RPETCAM: Reconfigurable power-efficient ternary content-addressable memory on FPGAs," IEEE Trans. Very Large Scale Integr. (VLSI) Syst., vol. 28, no. 8, pp. 1925–1929, Aug. 2020.
30. K. Locke, Parameterizable Content-Addressable Memory, Xilinx, San Jose, CA, USA, 2011.
31. TCAM Source Code. Accessed: Aug. 23, 2023. [Online]. Available: https://github.com/sridharraj240/TCAM

Received: 08. 06. 2022
Accepted: 03. 09. 2022

Original scientific paper

https://doi.org/10.33180/InfMIDEM2022.305

Informacije MIDEM
Journal of Microelectronics,
Electronic Components and Materials
Vol. 52, No. 3(2022), 191 – 202

Estimation of Traffic Influence on Energy Saving at GSM Channels with Reallocation

Vladimir Milovanović[1], Juan Antonio López Martín[2], Djuradj Budimir[3], Mladen Mileusnić[4], Vladimir Matić[4], Bojana Jovanović-Lazić[4], Aleksandar Lebl[4], Dragan Mitić[4], Žarko Markov[4]

[1]Faculty of Engineering, University of Kragujevac, Kragujevac, Serbia
[2]Departamento de Ingenieria Electrónica, ETSI Telecomunicación, Univeridad Politécnica, Madrid, Spain
[3]Wireless Communications Research Group, University of Westminster, London,United Kingdom and School of Electrical Engineering, University of Belgrade, Belgrade, Serbia
[4]Radiocommunications department, IRITEL a.d., Belgrade, Serbia

Abstract: This paper presents an innovative procedure for base station emission power calculation in the case of traffic channels reallocation implementation in GSM mobile systems. The main idea of active traffic channels reallocation is to place the connections which require higher emission power due to higher mutual distance between base station and mobile station to the first frequency carrier because these channels have to be always in active mode due to the applied discipline of traffic service in GSM mobile systems. The principle of connections reallocation on the base of distance values sequence determination is novelty comparing to the much more applied principle of connections arrangement according to the propagation conditions. Power saving as the result of this method usage is compared to the necessary power when the sequential hunting with homing method of idle channel looking for is applied. Two special cases are analyzed: 1. the case of low offered traffic (when not more than 6 traffic channels are busy on average) and 2. the case when offered traffic is increased. It is proved that the achieved relative energy saving when the offered traffic is increased over 6Erl rapidly grows at first and then begins to fall. It is important that the absolute value of power saving continuously increases when the offered traffic is increased. One typical example of base station emission power save daily profile is presented on the base of the obtained results. All results in the paper are verified by traffic process simulation.

Keywords: energy saving; base station emission power; sequential hunting with homing method of idle channel seizure; channel reallocation; daily traffic profile

Ocena vpliva prometa na varčevanje z energijo v kanalih GSM s prerazporeditvijo

Izvleček: V članku je predstavljen inovativen postopek za izračun emisijske moči bazne postaje v primeru prerazporeditve prometnih kanalov v mobilnih sistemih GSM. Glavna ideja prerazporeditve aktivnih prometnih kanalov je, da se povezave, ki zaradi večje medsebojne razdalje med bazno in mobilno postajo zahtevajo večjo moč oddajanja, prenesejo na prvo nosilno frekvenco, saj morajo biti ti kanali zaradi uporabljene discipline prometnih storitev v mobilnih sistemih GSM vedno v aktivnem načinu. Načelo prerazporeditve povezav na podlagi določitve zaporedja vrednosti razdalj je novost v primerjavi z veliko bolj uporabljenim načelom razporejanja povezav glede na pogoje razširjanja. Prihranek energije zaradi uporabe te metode je primerljiv s potrebno močjo pri uporabi zaporednega lovljenja z metodo iskanja praznega kanala. Analizirana sta dva posebna primera: 1. primer nizkega ponujenega prometa (ko je v povprečju zasedenih največ 6 prometnih kanalov) in primer, ko se ponujeni promet poveča. Dokazano je, da doseženi relativni prihranek energije pri povečanju ponujenega prometa nad 6Erl najprej hitro narašča, nato pa začne padati. Pomembno je, da se absolutna vrednost prihranka energije nenehno povečuje, ko se poveča ponujeni promet. Na podlagi dobljenih rezultatov je predstavljen en tipičen primer dnevnega profila prihranka energije emisij bazne postaje. Vsi rezultati v članku so preverjeni s simulacijo prometnega procesa.

Ključne besede: varčevanje z energijo; oddajna moč bazne postaje; zaporedni lov z metodo iskanja domačega kanala v mirovanju; prerazporeditev kanala; dnevni prometni profil

---

* *Corresponding Author's e-mail: vlada@kg.ac.rs, email2@server.com*

How to cite:
V. Milovanović et al., "Estimation of Traffic Influence on Energy Saving at GSM Channels with Reallocation", Inf. Midem-J. Microelectron. Electron. Compon. Mater., Vol. 52, No. 3(2022), pp. 191–202

1 Introduction

Last five decades are characterised by the rapid development of mobile communications. Starting from the first generation (1G) of mobile systems between 1970s and 1980s, achievable communication rate and data capacities were constantly increased [1]. The first generation systems (also known as Advanced Mobile Phone Systems – AMPS) were used only for analog voice communication and their maximum rate was 2.4kb/s [2]. These performances were improved in the second generation systems (2G) which started in 1990s. The applied digital Global System for Mobile (GSM) technology allowed communication rate of 1Mbps. Although still devoted mainly to voice communication, these systems introduced services as text messages, picture messages and multimedia messages (MMS) [2].

The third generation systems (3G) in Code-Division Multiple Access (CDMA) technology and Universal Mobile Telecommunication System (UMTS) framework further improved communication rate to 2Mbps maximum [2] and allowed services as video calls and conferencing, video with some multimedia, mobile television, Global Positioning System (GPS). 3G technics was first introduced at the beginning of 21st century. The new applied principles are based on packet switching to achieve fast data transmission.

The fourth generation (4G) systems started in 2010. The applied technologies are Long Term Evaluation (LTE) and Worldwide Interoperability for Microwave Access (WiMAX). The communication rate is increased to 60Mbps and even 100Mbps [1], [2]. The new services in 4G systems are mobile web access, gaming, 3D television. The spectral efficiency is approximately doubled comparing to 3G systems [3]. The achieved improvements are based on the combined application of Frequency-Division-Duplex (FDD) and Time-Division-Duplex (TDD) principles [3].

The most modern systems are designated as the fifth generation (5G). The significantly increased data rates comparing to 4G (up to 20Gbps down-link) allow application of services as Internet of Things (IoT), Machine Learning (ML), UltraHD streaming videos, virtual reality media and so on [1]. This technology is at high level of development today.

Energy (power) consumption decrease is one of the primary goals today. It is important to consider possibilities to save power in each system type from 2G to 5G. When speaking about the necessary energy for base station (BTS) operation in GSM systems, traffic channels reallocation is one of the methods. It is proved in [4] that reallocation decreases this objective in two ways: by seizing traffic channels in the first carrier in the beginning and then by allocation of these channels to the users who need the maximum emission power. The price paid for this saving is the reallocation of busy traffic channels in such a way that the channels which require maximum emission power are placed in the first 6 traffic channels (TCH) which have always the maximum emission power [5]. The procedure for channels reallocation is not more complex than the simplest handover. (All channels at the first carrier in all BTSs have the maximum emission power and are used to determine the nearest BTS to some mobile station, MS). It is proved in [4] that energy and power saving depends on the number of carriers, i.e., number of channels, on the environment characteristics and on the users surface distribution in the mobile cell. This paper considers process of power saving in more detail and the accent in this paper is on the traffic analysis for all traffic values. Power saving as the function of the offered traffic is determined in all cases, i.e., also at small traffic values. It is proved that power saving exists even at such low traffic level. The additional value of this paper in relation to [4] is that it considers power saving according to the daily traffic profile. The significant level of relative power saving comparing to the systems without reallocation during the day is proved, because approximately half a day time the offered traffic is not high and may be served by the traffic channels on the first carrier. The modifications in the paper comparing to [4] are related also to some important aspects of simulation process: for example, simulation now supports conclusions making not only on the base of offered traffic but also on the base of instantaneous realized connections number.

The existing methods and solutions for power saving in mobile GSM systems are presented in the section 2. The two models of traffic channels seizure, which are later analyzed in this paper - the sequential hunting model with homing procedure of looking for idle channel and the model with channel reallocation are described in the section 3. All variables used in this paper are also defined in this section. These two models in the case of small traffic, (i.e., when less than 7 connections are realized), are compared in the section 4. The calculation of base station emission power in the case of low offered traffic – (approximately) up to about 7E is presented in the section 5. The section 6 is related to the emission power calculation and, consequently, to the power saving when the second model is applied in the case that the value of offered traffic is increased. The section 7 presents one example of daily traffic profile and base station emission power saving in the case of the second model application. The section 8 gives retrospective view to the number of mobile stations in GSM technology which are still going to be used in the world. The obtained analytical results are verified by traffic process simulation as described in the section 9. The conclusion is, finally, given in the section 10.

2 Existing solutions for power saving in mobile GSM systems

There are three main approaches for energy saving in mobile communications networks. The first one is application of advanced dynamic algorithms for traffic resources reallocation in mobile network. The second one is application of sleep mode on some groups of channels for which there is no need to carry traffic. And, finally, the third one is implementation of more energy-efficient network elements [6]. The first two groups of solutions request only software tools for their realization while changes of hardware elements are necessary to perform modifications according to the third group. Thus this third group is, obviously, more demanding and more expensive and it is not considered in this paper. The solution presented in this paper fall into the first group of approaches and this solution is considered in comparison to some other, existing approaches belonging to the first two groups.

Existing solutions for traffic resources reallocation are mainly related to the connections displacement between different subbands [7]. When considering GSM systems, this is between channels at 900MHz and 1800MHz which exist at the same location. There are three reasons for such reallocation: 1. In the case of lower traffic load when different subbands are only partially busy, it is possible to collect all connections on one (or a less number) frequency carrier and thus to free the other frequency carrier. The idle carrier then may be put to sleep mode to lower total power consumption; 2. Attenuation at 900MHz subbands is less than at 1800MHz, so connections may be realized over channels at 900MHz subbands to allow lower power consumption; 3. The best effect in emission power consumption reduction may be sometimes achieved when traffic over all frequency subbands is equalized.

The second approach which supposes application of sleep mode is the logical consequence of traffic channels release on some frequency carriers after implementing reallocation according to points 1. and 2. in the previous paragraph. Generally, this second approach leads to higher values of power consumption than the solutions from the first approach. The second approach is widely used in all types of mobile systems mainly in the time of low traffic. When implemented in GSM systems, sleep mode supposes that some minimum signal transmission (for example pilot signal, channels on the first carrier) should remain [8]. It means that complete base station power supply turn-off could not be achieved to easily recover to operation mode when the traffic level increases again. The simulation of GSM system with activated sleep mode is presented in [9]. The performed Monte Carlo simulation is based on data collected on real BTS locations. The goal of simulation is to determine the value of total BTS power if sleep mode is applied.

The goal in modern mobile networks is to reduce power consumption of GSM systems by improved methodology for BTS or only frequency carriers' turn-off and turn-on [10]. The threshold parameters for activating and deactivating sleep mode are adjusted by the implementation of machine learning algorithms [11]. Such access additionally decreases the mean number of active frequency carriers and thus reduces power consumption comparing to classical switching parameters control. In the case that GSM base station exist at the same location with some 3G or 4G base station, decreasing power consumption in GSM mobile system may leave more power for 3G or 4G system. It means that reallocation of traffic resources in GSM system thus leads to power consumption reallocation [12] which allows more traffic to be realized over more applied 3G or 4G systems.

3 Models of traffic channels groups, designations and assumptions

Our access in power saving pertain to the first approach according to the division from the previous section. It is based on an innovative principle of traffic channels reallocation according to the distance between the base station and each active user station.

Let us consider the circular GSM cell with the radius R. The number of traffic channels in the cell is $N=6+8\cdot(n-1)$, where n is the number of frequency carriers. The surface user density in the cell is uniform. The number of users in one cell, M, is supposed to be significantly greater than the number of traffic channels. It is also supposed that telephone calls are generated randomly. The emission power in the first 6 traffic channels is maximal and in the remaining channels power control is performed, i.e., it is adjusted according to the user needs. The necessary power mainly depends on the user distance from BTS.

The designation for the power will be w, the mean and the maximum power of one channel will be designated by w_m and w_{max}, respectively. The power of the i^{th} ($i = 1, 2,\ldots, N$) channel will be designated by w_i, the mean and the maximum power of the i^{th} channel will be designated by w_{im} and w_{imax}, respectively. The user distance from BTS, d, affects the necessary emission power according to the law $w=a \cdot d^{\gamma}$, where a is the coefficient of proportionality and γ is the environment attenuation factor [5]. The state when i traffic channels are busy will be designated by {i}. The offered traffic is designated by A and served traffic by Y. The designation P(i, A, N) means the probability that i channels (i = 0, 1,…, N-1, N) are busy in the group of N channels if the offered traffic is A Erl. This probability is called the probability of state {i}. Each call may seize idle channel, so this channel group comes to Erlang model. The probability that all channels are busy is called the probability of traffic loss and designated by E(N, A) = P(N, N, A), the so called Erlang B formula.

Power saving is achieved in two ways: at lower traffic all connections are realized over the channels in the first carrier which always have (maximum) power and at the higher traffic users who need higher power are connected over the TCH of the first carrier. That's why two cell models are going to be analyzed.

The first model (MC1) is the standard one applied in the cells without reallocation. The main property of this model in this paper is the channel selection for the new call. The idle channel for each new call is selected by sequential hunting with homing [13], section 4. This procedure of channel selection for the new call allows that the first 6 channels which have the highest emission power do not remain idle. The first cell model is presented in the Fig. 1 which is taken over from [4].

The second GSM cell model (MC2) satisfies two conditions. The first one is that all connections should be realized over the first 6 traffic channels when the number of connections, i.e., busy channels is less than 7 ($i<7$). The second condition is the following one: if it is $i>6$, six connections which request the higher emission power than the remaining connections should be realized over the first 6 channels. We need to have a ranking list of realized connections with the data about the necessary emission power (i.e., distance BTS - MS) in order to compare this power to the necessary power for the new call.

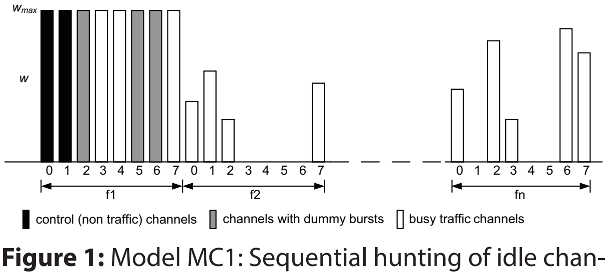

Figure 1: Model MC1: Sequential hunting of idle channel with homing from the first channel on the first carrier (taken over from [4]).

Filling, i.e., seizing of the first 6 traffic channels is performed using the so called channel reallocation which is presented in the Fig. 2 (taken over also from [4]). The necessary power for the channel is symbolically designated by asterisk and for some channel *i* this value is w_i.

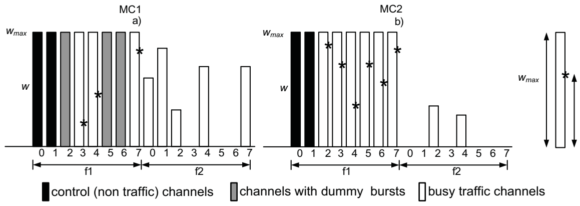

Figure 2: Model MC2: Channel reallocation such that 6 channels with the highest necessary power take traffic channels of the first carrier (taken over from [4]).

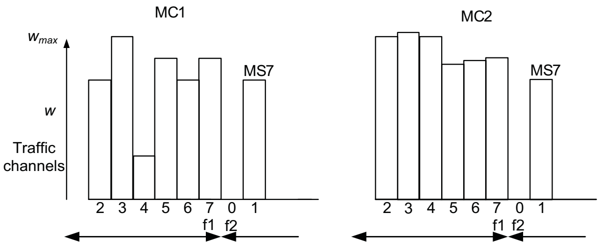

Figure 3: Models MC1 and MC2 in the moment when 7 connections are realized.

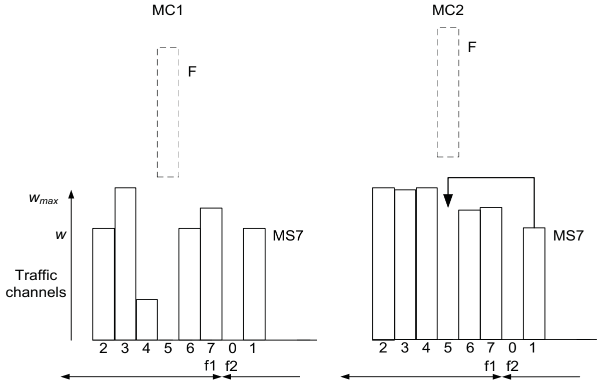

Figure 4: Processes in the models MC1 and MC2 in the moment of finishing one of 7 existing connections (the connection realized on the first carrier).

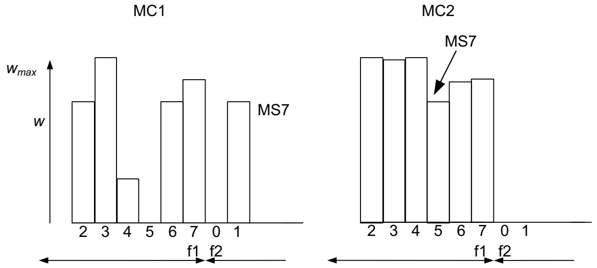

Figure 5: Allocation of 6 remaining channels in the models MC1 and MC2 after the connection end.

4 The characteristics of considered cells at low traffic load

It has been already emphasized that at low traffic load (i<7) when the model MC2 is applied all connections are realized over the first 6 channels while it is not the case when the model MC1 is applied. Let us now consider a simple example with 7 realized connections. All connections except the connection of the seventh user (MS7) are realized over the channels on the first carrier f1. The connection of MS7 is realized in the channel of the second carrier f2, Fig. 3.

Let us suppose that connection over the channel 5 ends in the moment *t1* (connection F) and that this channel releases. In this moment nothing happens in the cell MC1. The channel 5 on the first carrier remains idle until the moment when the new call arrives. Owing to the sequential method of idle channel looking for starting from the first channel, the new call which is initiated in the moment *t2* will seize the channel 5.

The connection reallocation is performed in the cell MC2: the connection of the user MS7 continues over the released channel 5 on the first carrier instead over the channel 1 on the second carrier, figures 3, 4 and 5. It is clear that the power in MC1 equals: $w_{MC1} = 6 \cdot w_{max} + w_m$ where w_m is the mean power in the channel 1 of the second carrier. The emission power in MC2, under the same conditions, equals $w_{MC2} = 6 \cdot w_{max}$. It is obvious that it is

$$w_{\mathrm{MC1}} > w_{\mathrm{MC2}} \tag{1}$$

It may be concluded that at low traffic values, besides emission of maximum power in all 6 TCHs of the first carrier, power is also generated in some other channels when considering MC1 cell. This is impossible in MC2 cell: if the number of connections is less than 7, emission power is the same as if there is no traffic. It has to be noted that an example, presented by the figures 4 and 5, is the simplest one. Similar to this example, it may happen releasing of several channels on the first carrier in the MC1 cell, which even more increases the difference of emission energy in MC1 and MC2, but the probability of such an event is significantly lower.

5 Emission power calculation at low traffic value

Let us consider an example of two cell models when they are in the state *{6}*, i.e., there are 6 connections. The offered traffic is *A*. The served traffic by channel *i* is Y_i, (i = 1, 2, 3, 4, 5, 6). According to [13], equation 4.14, when sequential looking for idle channel with homing is applied, the served traffic by the i^{th} channel is

$$Y_{\mathrm{i}} = A \cdot \left(E(i-1, i-1, A) - E(i, i, A)\right) \quad i = 1,2,\ldots,6 \tag{2}$$

for the MC1 cell. It is the part of time when channel *i* is busy. In other words, it is the difference of overflow traffic on channels *i-1* and *i*.

The characteristic of served traffic on one channel, *i*, is that it is $Y_i < 1$. That's why the probability that all 6 traffic channels on the first carrier are busy is $Y_1 \cdot Y_2 \cdot Y_3 \cdot Y_4 \cdot Y_5 \cdot Y_6 < 1$. This, further, means that idle channels may exist on the first carrier in the state *{6}* in MC1 cell. The traffic process simulation program for such cell is made to determine probability of idle channel on the first carrier as a function of the offered traffic (see section 8). The obtained results are presented in the Table 1.

The difference 1 - Y_i, (i = 1, 2……6) represents the part of time when the i^{th} channel is idle.

$$S = \sum_{i=1}^{6} \left(1 - Y_{\mathrm{i}}\right) \tag{3}$$

The sum represents the mean number of idle channels in the state *{6}* on the first carrier in the cell. Therefore, there are 6 connections in the state *{6}* and it is clear that this number *S* will represent the mean number of busy channels in the other carriers.

The dependence of mean number of busy channels in carriers 2, 3,... in the state *{6}* on the offered traffic *A* in the cell MC1 is presented in the Table 2. The results in the Table 2 are obtained by simulation.

Therefore, the mean number of busy channels on other carriers is *S* in the state {6} at the offered traffic *A* and the power is generated in these channels in MC1 and not in MC2. These values are obtained by traffic process simulation in the MC1 cell whereby the total number of traffic channels is *N*=14. It is clear that possible power saving in the MC2 cell is proportional to the number of channels which are busy on the second carrier in the MC1 cell.

Example: If the offered traffic is *A* = 5 Erl in the state {6}, nearly all measurements will show that between first 6 channels exists, on average, one idle channel in the MC1 cell, i.e., that one channel is busy in other channels. The higher emission power in MC1 comparing to MC2 is the phenomenon which exists also at low values of offered traffic.

It may be concluded that power saving at lower traffic values is realized only by using the channels of the first carrier.

Table 1: The probability of at least one idle channel existence on the first carrier as a function of offered traffic in the model MC1 when there are 6 realized traffic connections, *N=14*.

Offered traffic (Erl)	2	3	4	5	6	7
Probability 1-$Y_1Y_2Y_3Y_4Y_5Y_6$ that there is an idle cannel on the carrier 1, in the state {6}	0.2957	0.4457	0.5659	0.6505	0.7271	0.7698

Table 2: The number of busy channels on the carriers 2, 3, as a function of offered traffic in the MC1 cell when there are 6 realized connections.

Offered traffic (Erl)	2	3	4	5	6	7
The number of busy channels on the carriers 2, 3,… in the state {6}, N=14	0.3098	0.5586	0.7726	0.9505	1.1475	1.2791

It has to be noted that the Table 2 is related only to the state *{6}* whose probability is changed when offered traffic is changed. The second important fact is that channel seizure in carriers 2, 3,… in MC1 cell happens also in other states.

6 Power saving at traffic increase

Let us consider now the case when the offered traffic increases, i.e., the number of connections is greater than 6. The first 6 traffic channels in the MC1 cell serve user connections which have been initiated in random moments. The other connections, which have also started in random moments, are served in the following channels. The necessary emission power in all channels including the ones outside the first 6 traffic channels is in principle different, but may be considered as equal to the mean channels power. The mean channel power for the uniform user surface density distribution is $w_m = 0.5 \cdot w_{max}$, where it is $w_{max} = a \cdot R^2$ because it is analyzed the case for the value $\gamma = 2$ [14].

Sectors, i.e., rings which separate areas with different necessary users' power are presented in the Fig. 6. As an example the situation of mild traffic increase is considered i.e., when the number of connections is 8 and the number of sectors is 16. (According to [15], the power control is realized in 15 steps of 2dB each step, here are considered 16 steps to easier reference explanation supported by examples). The probability that the call is generated in some sector is proportional to the number of traffic sources, i.e., to the number of users in that sector (or, in other words, to the sector area) in relation to the total number of users. (It is clear that the number of users increases when the sector radius increases at uniform distribution of surface users' density. The other reason of sectors' area increase when these sectors are more distant from BTS is that emission power decreases according to the exponential law). The question from this example is: if the total number of connections is 8, from which sectors come 6 connections which request the maximum power? From all sectors (100% of surface, i.e., users) come 8 (100%) calls and 6 (75%) calls are generated from the sectors which represent 75% of surface/users. In our example these are 3 sectors with the maximum radius and their border is at about $R2 \approx 0.5 \cdot R$.

The mean power of active channels is $w_m = 0.5 \cdot w_{max}$. The channels on the first carrier are seized by 6 users and two users seize two channels on the second carrier. The way how these calls are arranged in the channels of MC1 and MC2 cell is presented in the Fig. 6. In the MC1 cell the channels are seized according to the order of their arrivals. Therefore, the connections in the first carrier request power according to the random selection. That's why, besides the mandatory power of the channels on the first carrier (w_{max}), the emission power is in MC1 cell increased by the value of mean power of two channels in the second carrier, i.e., $2 \cdot w_m = w_{max}$.

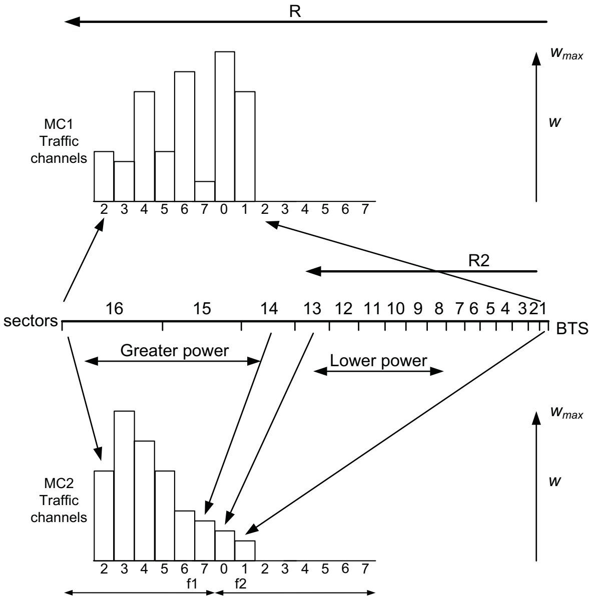

Figure 6: Spatial layout wherefrom calls are initiated on average in models MC1 and MC2 when 8 connections are realized.

The MC2 cell is now considered under the same conditions. Due to reallocation implementation, the first 6 channels are seized by the users who request maximum emission power. The calls of remaining two users originate from 13 sectors which are located nearest to BTS. The mean necessary power of these users is $w_{m2} = 0.5\cdot w_{max2}$, where w_{max2} is the highest power of one channel in the circle of the radius $R2$ which contains 13 sectors nearest to BTS, $R2=(0.5\cdot R)$, i.e., $w_{max2} = (1/4)\cdot w_{max}$. The mean emission power per a channel of the second carrier in MC2 is $w_{m2} = (1/2)\cdot w_{max2}$. The ratio of emission power per a channel of the second carrier in MC1 and MC2 cell at 8 connections, $\gamma = 2$ and uniform distribution of surface users distribution is 4.

The consequence of further offered traffic increase is the increase of the number of calls coming from the greater number of sectors. This process should be presented in the Fig. 6 by the greater number of calls, i.e., busy channels. The users in MC1 would continue to seize channels according to the random principle. In MC2 the first 6 channels would be seized by users from the sectors which are more distant from BTS. The remaining channels would be seized by users from the group of sectors with the radius $R3$ which is greater than the one from the Fig. 6, i.e., $R3 > R2$. That is why the ratio of emission power in MC1 and MC2 decreases with the traffic increase.

Example: Let us suppose that the number of channels is N=14, the number of connections is 10, $\gamma = 2$ and that distribution of users' surface density is uniform. As in the previous example, the call arrival is proportional to the sector area. We are interested from which sectors come 6 of total 10 instantaneous calls if these 6 calls request maximum power. It is clear that these 6 calls come from the distant sectors from BTS and this is 60% of surface/users. These are, on average, two sectors with the greatest radii. The sectors are limited by the radius $R3$ at the distance approximately $R3 \approx 0.63\cdot R$ from BTS. Each channel of the second carrier in MC1 requests $0.5\cdot w_{max}$ on average. The mean power of 4 channels in the second carrier of MC2 is determined by the mean power in the part of cell with the radius $0.63\cdot R$, i.e., it is now $w_{max2} = 0.63^2\cdot w_{max} = 0.397\cdot w_{max}$. The ratio of mean emission power in the channels of the second carrier in MC1 and MC2 is $w_m/w_{m2} = 0.5\cdot w_{max}/0.5\cdot w_{max2} = 1/0.397 \approx 2.5$.

The ratio of mean power per channel in MC1 and MC2 cells (w_m/w_{m2}) as a function of the number of connections is presented in the Fig. 7. The other data is the same as in the previous two examples.

Figure 7 presents that the relative ratio of emission power per channel in MC1 and MC2 decreases when traffic (i.e., the number of realized connections) is increased. However, the absolute amount of power save is higher for the higher traffic values, because the power is saved on each active channel.

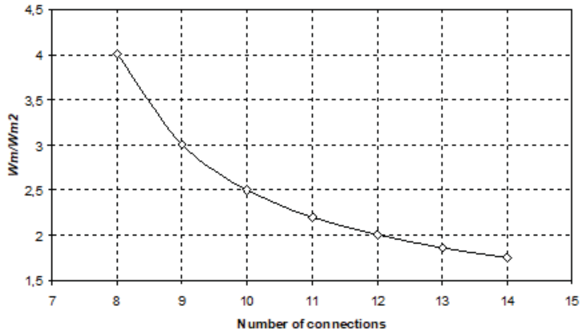

Figure 7: The ratio of mean power per channel at models MC1 and MC2 as a function of the number of connections, $N=14$, $\gamma = 2$.

Example: The saved power when 8 connections exist is $2\cdot w_m - 2\cdot w_{m2} = w_{max} - 0.25\cdot w_{max} = 0.75\cdot w_{max}$. If the number of connections is higher, i.e., 12, the power save on the second carrier is

$$6\cdot w_m - 6\cdot w_{m2} = 3\cdot w_{\max} - \frac{3}{2.11}\cdot w_{\max} = 1.58\cdot w_{\max} \qquad (4)$$

which is the higher saving in absolute values of power.

7 Daily profile of emission power

It is clear that channel reallocation allows emission power saving, but the level of saving depends on the number of busy channels, i.e., on the offered traffic A. As the offered traffic is changed during a day according to the so-called daily traffic profile, the level of emission power saving in the cell with reallocation according to MC2 will be also changed. Figure 8 presents daily traffic profile, i.e., the number of connections for the case of a cell with two carriers. After that, daily profile of emission power for the MC1 cells (black line) and for MC2 (red line) is presented in the Fig. 9. The other conditions are: surface user density is uniformly distributed, there are two carriers and environment coefficient $\gamma = 2$.

The power unit on the y-axis of the Fig. 9 is the maximum power, i.e., $w_{max}=a\cdot R^2$. It is clear that the difference between the black and red line represents the emission power save in this case and that the similar daily profile of the emitted (and saved) power may be obtained for each specific case.

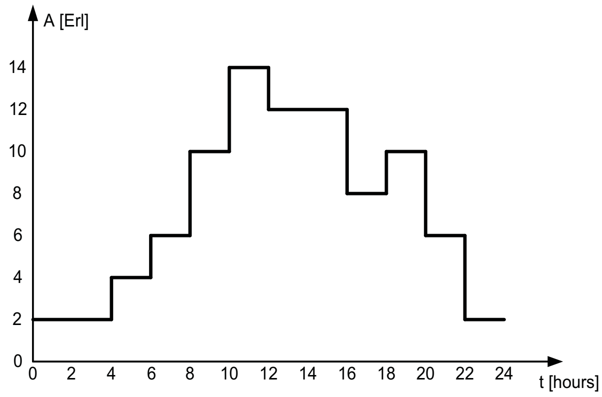

Figure 8: Daily traffic profile (the mean number of connections) in the considered cells according to the models MC1 and MC2.

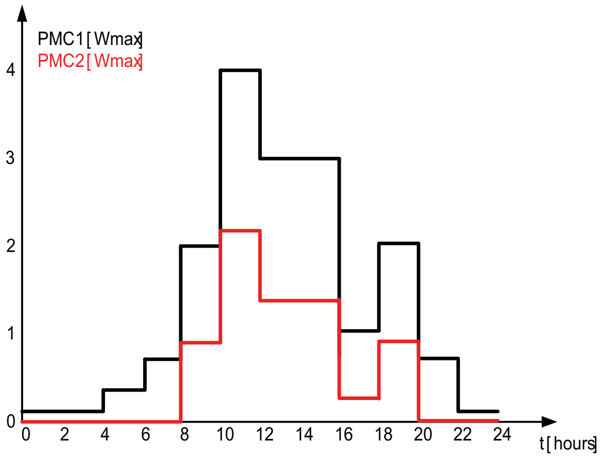

Figure 9: Daily profile of the emission power variation for channels 7, 8, ..., etc., MC1 (black) and MC2 (red) for the supposed daily traffic profile from the Fig. 8.

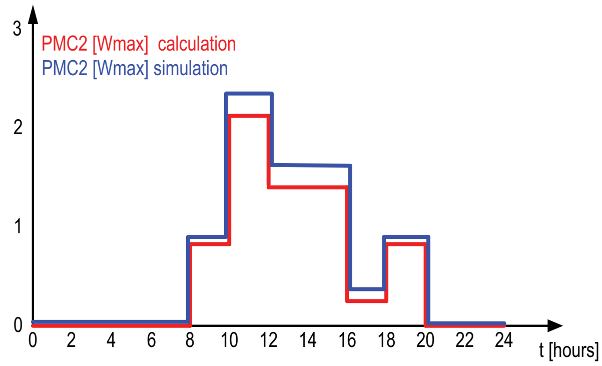

Figure 10: Daily profile of the emission power change for the channels 7, 8, …, etc. in the cell MC2 determined analytically (red) and by simulation (blue) for the supposed daily traffic profile from the Fig. 8.

The total daily power consumption saving when our method is applied comparing to the pure sequential hunting with homing procedure of looking for idle channel may be calculated as the surface value between the black and red line in the Fig. 9. This value is about 21W. This value in absolute sense is not high. But, relatively to the total daily emission power value, the contribution of our solution is about 60%. Namely, the total emission power consumption without our solution implementation, calculated as the surface between the black line and *x*-axis in the Fig. 9, is about 35W. This is important if possible interference to the other system, which perhaps operates in the same frequency band as the considered GSM system, is analyzed. Lower emission power on the GSM system allows that the signal on this other system has better quality.

The value of energy save is verified by simulation and the comparison of calculation and simulation values is presented in the Fig. 10. Quite a small difference of these values results from the difference in computation (the power determined by the sector ordinal number) and simulation (continual power directly dependents on distance).

8 A look at reducing number of GSM users in the world and to the comparison with other approaches for power saving

In this paper it is presented how channel reallocation affects emission power saving in mobile network 2G, i.e., GSM. The question of the relevance of this research and time limitation of the results can with good reason be asked. However, the predictions of the study [16] suggest that hundreds of millions of GSM network users will exist in the world for a long time. This is especially true for some developing countries with many inhabitants where still 99% users use mobile phones in GSM technology [17]. There are even areas where only GSM mobile systems are implemented [11]. Generally speaking, successive suspension of GSM connections is planned in the developed countries (in Italy till 2029. year), but in undeveloped countries such connections will continue to exist after this period [18]. It is the reason why we think that power saving in GSM network could not be neglected.

Comparing to other approaches belonging to the first group of solutions emphasized in the section 2, our method for channels reallocation does not request to have available carriers from both 900MHz and 1800MHz in the same BTS, because power saving is realized on different principles. The necessary software tools in both cases (existing solutions and our method) request the similar software tools: implementation of handover for channels rearrangement.

Comparing to the solutions from the second group which are related to the sleep mode activation, our method for power saving is applied regardless of the traffic value. In the section 7 we have already illustrated its implementation by the daily profile, i.e. during the whole day. On the contrary, sleep mode is implemented only at low traffic values, which usually means at night. The additional problem when turn-on or turn-off of sleep mode is performed is to determine the threshold values for these two actions [10], [11]. In principle, power saving achieved by sleep mode activation is significantly higher than when our method is applied. But, when traffic values are not low (for example during the day time at the great majority of BTSs), sleep mode may not be activated and there is no power consumption decrease due to its application. In such a case the power saving would be achieved only by the implementation of our method, as it is applicable regardless of the traffic value.

The main subject of the paper is to compare the characteristics of our solution for improved power consumption to the power consumption in the classical GSM system with sequential hunting with homing looking for idle channel and the majority results are related to this subject.

9 Simulation

All simulations in this paper are performed in C++/C programming language. It is performed using simple, commercially easily available software packs installed on home-version PC. There is no need for special, expensive software programs or advanced computer systems. The main input parameters in simulation are the number of applied traffic channels (*N*), the offered traffic (*A*) and the environment attenuation factor (γ) which may be in the range 2-5. One more element which is important for simulation is the type of users' distribution (we consider uniform distribution). The main output parameters are the mean values of emission power in the original system with sequential hunting with homing and in the system with reallocation. Traffic loss probability and the values of offered and served traffic are determined in the simulation in order to validate simulation process correctness. Simulation is based on roulette (Monte Carlo) traffic simulations used in classical telephone techniques long ago [19]. These traffic simulations are upgraded in a whole series of papers by a component to determine base station emission power on the base of distance between the base station and the mobile user. This distance is also calculated starting from the randomly generated number [20], [21].

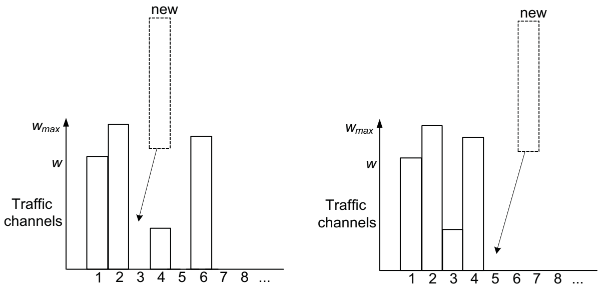

a) b)

Figure 11: Channel seizure in a homing system: a) earlier seized channels are not one after the other; b) earlier seized channels are one after the other.

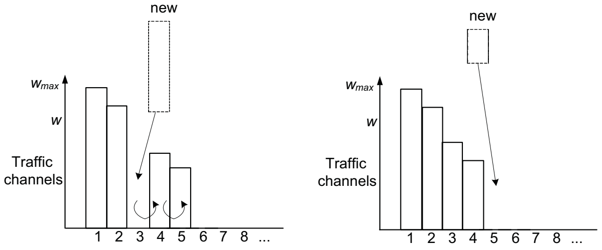

a) b)

Figure 12: Channel seizure in the system with reallocation: a) earlier seized channels are not one after the other; b) earlier seized channels are one after the other.

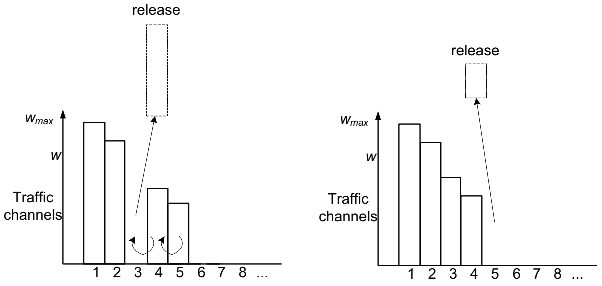

a) b)

Figure 13: Channel release in the system with reallocation: a) the released channel is not the last in the series of busy channels; b) the released channel is the last in the series of busy channels.

Simulation program from [20] is further upgraded for the analysis purposes. In the part for traffic analysis this upgrade includes specific discipline of traffic channels seizure in the first case of systems with homing procedure for idle channel looking for and in the second case of homing seizure with channel reallocation. The part of upgrade is also the specific procedure of channel release at systems with homing seizure with channel reallocation.

The algorithm of traffic channels seizure at each new connection initialization is based in both cases on homing procedure of idle channel looking for starting from the first traffic channel. The goal is in the case of systems with homing seizure to find the first idle traffic channel, as it is presented in the Fig. 11. It may be, for example, channel number 3 according to the Fig. 11a) given that channels 1 and 2 have been busy from earlier. In the case that all busy channels are sequenced one after the other in the considered moment of new connection initialization, the first channel after them is seized (in an example in the Fig. 11b) channels 1-4 are busy and the new connection will take the channel 5). In the case of systems with reallocation all busy channels are arranged one after the other according to their decreasing necessary power, i.e., decreasing mutual distance between base station and mobile user. The value of necessary emission power for the new connection is compared successively from the first channel for all already realized connections until it is found the connection with the power lower than the necessary power for the new connection. When such a connections is found, the channels for all connections starting from it onwards are shifted for one channel towards the higher ordinal number, and the new connection is placed on the released place (according to the Fig. 12a), the connections on the channels 3 and 4 are shifted to channels 4 and 5, while the new connection takes the channel 3). If all existing connections have the higher power than the new initiated connection, this new connection is placed at the end of the row on the first idle place (in the channel 5 after 4 already realized connections in the example in the Fig. 12b)).

The procedure for channel release in a system with reallocation is presented in the Fig. 13. There are 5 busy channels before release in the Fig. 13a) and the connection at the channel 3 has to be terminated. In this case the channels with the higher ordinal number than the ordinal number of the connection which has to be released are shifted for 1 channel towards the lower channel ordinal number (channels 4 and 5 to the positions 3 and 4), and the channel on the position 5 is released (w=0). If it is necessary to terminate the connection on the last in the series of busy channels, it is only released without reallocation of busy channels (Fig. 13b)).

The principle of base station emission power definition is the same as in [21] for uniform user surface distribution and for γ=2. The more complicate case of emission power calculation for non-uniform user surface distribution and $\gamma\neq2$ is analyzed in [20].

The simulation program, which is realized according to the described algorithm, is freely available at the address [22]. Besides the program code, also is available the file obtained by the simulation with the data used to verify the analytically defined characteristic in the Fig. 7.

Simulation is very powerful method for systems operation modelling. It allows very fast verification because simulation program execution is significantly less time consuming than measurement in real world operation. The verification is also simpler and cheaper than testing on the polygon. The procedure which is described in this paper is supported by the authors' long year experience in simulation program development [23].

10 Conclusions

It may be concluded from this paper that channel reallocation always contributes to emission power saving. Even at low traffic values power saving (of lower extent) exists as presented in the section 4. When the number of simultaneous connections overcomes 6, relative emission power saving rapidly increases if channel reallocation is applied. Relative power saving slightly decreases with the further traffic increase.

Emission power saving in absolute amount increases with the traffic increase.

Everything that is concluded about the dependence of emission power saving as a function of the type of surface user distribution, number of the users and environment coefficient γ from [4] is valid also here with respect of dependence on traffic value.

The results obtained in this paper are verified by our original simulation program. There is a small difference between the results obtained analytically and by simulation as illustrated in the Fig. 10. The reason has been already explained at the end of the section 7: in reality the BS power is changed in discrete steps according to the ordinal number of the sector where the MS is situated and in simulation this power is varied continually according to the distance between BS and MS. But, difference in the obtained results due to these two approaches is negligible as proved by the Fig. 10.

When considering dependence of emission power saving on the number of connections as a function of γ or number of users (i.e. frequency carriers), the quantitative relations would be established in the future work as the result of simulations after minor modifications of our verified simulation program [22].

The second aim in the future development is to compare in the quantitative sense performances of our solution to the existing solutions from the area of emission power saving in GSM systems. This comparison is related to the traffic analysis and to the necessary power level.

The last and even the most important aim is to study possibilities to adapt our solution for the implementation in newer generation networks – first of all in 4G (LTE) systems. Besides the possible effect to the emission power decrease in LTE systems, such an improvement would decrease interference to "5G under 6GHz" mobile systems (i.e. when they operate in a frequency band about 700MHz where LTE and 5G systems may coexist.

The importance of the study presented in this paper may be summarized in the following several main points according to the whole study presented in this paper: 1. GSM BTS emission power is decreased in absolute and, specially, relative amount; 2. it is possible to decrease this power regardless of the instantaneous emission power value and regardless of the frequency band where GSM system operates; 3. interference to other systems operating in the same frequency band is decreased; 4. for the future, our solution may be adapted for the application in other modern mobile systems, such as LTE.

All results in the paper are verified by traffic process simulation. Unfortunately, we are not able to realize verification of an idea presented in the paper by experimental implementation of real traffic in a live network but we would be glad if some mobile devices supplier or provider accepts to do it. We would like to contribute ourselves in such experimental verification.

11 Conflict of Interest

The authors declare no conflict of interest.

12 References

1. R. Dangi, P. Lalwani, G. Choudhary, I. You, G. Pau, "Study and Investigation on 5G Technology: A Systematic Review," *Sensors* 2022, Vol. 22, No. 26, pp. 1-32, 2021, ISSN: 1424-8220, https://doi.org/10.3390/s22010026.
2. A. S. Meril, M. Basthikodi, A. R. Faiyabadi, "Review: Comprehensive study of 5G and 6G Communication Network," *Journal of Emerging Technologies and Innovative Research (JETIR)*, Vol. 6, Issue 5, 2019, pp. 715-719, ISSN: 2349-5162.
3. F. Ivanek, "4G: Where are We Going?," *Informacije MIDEM*, Vol. 38, No.3, pp. 170-174, 2008, UDK621.3:(54+54+621+66), ISSN: 0352-9045, http://www.midem-drustvo.si/Journal%20papers/MIDEM_38(2008)3p170.pdf.
4. V. Kosjer, D. Mitić, A. Lebl, V. Matić, Ž. Markov, "Power saving technique based on traffic channels reallocation in gsm mobile network," *Journal of Electrical Engineering*, Vol. 71, No. 2, 2020., pp. 103-109, ISSN 1335-3632, https://doi.org/10.2478/jee-2020-0015.
5. G. Heine, *GSM Networks: Protocols, Terminology and Implementation*, Artech House, 1999., [Online] Available at: http://ik4hdq.net/doc/testi/gsm_networks.pdf, ISBN: 0-89006-471-7.
6. B. I. Bakare, T. C. Oguichen, "Appraisal of Green Communication Technology in GSM," *International Journal of Electronics Communication and Computer Engineering*, Vol. 9, Issue 3, pp. 89-92, 2018., [Online] Available at: https://ijecce.org/administrator/components/com_jresearch/files/publications/IJECCE_4265_FINAL.pdf, ISSN: 2249-071X.
7. A. Ailaz, O. Holland, Pangalos, et al., "Energy Savings for Mobile Communication Networks through Dynamic Spectrum and Traffic Load Management," Section 15 in J. Wu, S. Rangan, H. Zhang, *Green Communications: Theoretical Fundamentals, Algorithms, and Applications*, CRC Press and Taylor & Francis Group, 1st Edition 2013., 2nd Edition, 2016., ISBN: 978-1466501072, [Online] Available at: https://books.google.rs/books?id=wbvMBQAAQBAJ&pg=PA411&lpg=PA411&dq=gsm+reallocation+power+saving&source=bl&ots=05AHivQU6s&sig=ACfU3U1YAF0U5m8Je4EBXRF7sREmQUeMNw&hl=hr&sa=X&ved=2ahUKEwiy3Fn632AhVChqQKHVv9AKsQ6AF6BAgMEAM#v=onepage&q=gsm%20reallocation%20power%20saving&f=false
8. J. Wu, Y. Zhang, M. Zukerman, E. K.-N. Yung, "Energy-Efficient Base Stations Sleep Model Techniques in Green Cellular Networks: A Survey," *IEEE Communications Surveys & Tutorials*, Vol. 17, Issue 2, 2015, pp. 803-826, https://doi.org/10.1109/COMST.2015.2403395.
9. A. Spagnuolo, A. Petraglia, C. Vetromile, A. D'Onoftio, C. Lubritto, "Simulation Studies of the Power Consumption of a Base Transceiver Station," *Far East Journal of Electronics and Communications*, 2016, pp. 147-165, ISSN: 0973-7006, https://doi.org/10.17654/EC016010147.
10. A. Gaber, M. M. Zaki, A. M. Mohamed, M. A. Beshara, "Cellular Network Power Control Optimization Using Unsupervised Machine Learnings," *2019 International Conference on Innovative Trends in Computer Engineering (ITCE)*, 2019., Aswan, Egypt. https://doi.org/10.1109/ITCE.2019.8646611,
11. T. Sahmoud, W. Ashor, "Assign Hysteresis Parameter for Ericsson BTS Power Saving Algorithm Using Unsupervised Learning," 2021, pp. 1-7, https://doi.org/10.48550/arXiv2107.07412.

12. M. Ericson, A. Simonsson, “Method and Arrangement for Power Sharing in a Base Station,“ Patent No. US 9,398,547 B2, 2016., [Online] Available at: https://patents.google.com/patent/US20130225227.
13. W. B. Iversen, *Teletraffic Engineering and Network Planning*, DTU Course 34342, Technical University of Denmark, 2015., [Online] Available at: http://orbit.dtu.dk/files/118473571/Teletraffic_34342_V_B_Iversen_2015.pdf.
14. P. Jovanović, M. Mileusnić, A. Lebl, D. Mitić, Ž. Markov, “Calculation of the Mean Output Power of Base Transceiver Station in GSM,“ *Automatika*, ISSN 0005-1144, Vol. 55, No. 2, pp. 182-187, 2014., https://doi.org/10.7305/automatika.2014.06.373.
15. 3rd Generation Partnership Project, “Technical Specification Group Radio Access Network, GSM/EDGE Radio subsystem link control (Release 15),“ 3GPP TS45.008 v15.0.0., 2018, [Online] Available at: https://portal.3gpp.org/desktopmodules/Specifications/SpecificationDetails.aspx?specificationId=2710.
16. “Ericsson Mobility Report,“ EAB-21.010887 Uen, 2021., [Online] Available at: https://www.ericsson.com/4ad7e9/assets/local/reports-papers/mobility-report/documents/2021/ericsson-mobility-report-november-2021.pdf.
17. “Nigerian Communications Comission 2018 Subscriber/Network Data Report, Policy competition and Economic Analysis Department, [Online] Available at: https://www.ncc.gov.ng/docman-main/industry-statistics/policies-reports/832-2018-year-end-subscriber-network-data-report/file.
18. European Commision, “Study on the current and prospective use of the 900MHz band by GSM as a technology of reference, considering present and future Union policies,“ SMART 2019/0006, ISBN: 978-92-76-21071-9, https://doi.org/10.2759/002578.
19. L. Kosten, “Simulation in teletraffic theory,“ *6th ITC*, Münich, 1970.
20. M. Mileusnić, M. Popović, A. Lebl, D. Mitić, Ž. Markov, “Influence of Users’ Density on the Mean Base Station Output Power,“ *Elektronika ir Elektrotechnika*, ISSN: 1392-1215, Vol. 20, No. 9, pp. 74-79, 2014., http://doi.org/10.5755/j01.eee.20.9.5418.
21. M. Mileusnić, P. Jovanović, M. Popović, A. Lebl, D. Mitić, Ž. Markov, “Influence of Intra-cell Traffic on the Output Power of base Station in GSM,“ *Radioengineering*, ISSN 1210-2512, Vol. 23, No. 2, pp. 601-608, 2014., http://www.radioeng.cz/fulltexts/2014/14_02_0601_0608.pdf.
22. Program for GSM reallocation simulation, [Online] Available at: http://www.iritel.com/index.php/en/design-services/712-gsm-reallocation-simulation.
23. A. Lebl, D. Mitić, Ž. Markov, T. Šuh, M. Mileusnić, P. Jovanović, V. Matić, B. Trenkić, M. Popović, Ž. Tomić, P. Daković, I. Vidaković, B. Mitrović, “Development of Methods for Traffic Simulation of Telecommunication Processes in IRITEL over last 45 years,“ *Technics, Electrical Engineering*, special edition, pp. 78-87, 2017., ISSN: 0040-2176, UDC: 621.396:519.876.5, https://doi.org/10.5937/tehnika1703383L.

Arrived: 03. 05. 2022
Accepted: 08. 09. 2022

Boards of MIDEM *Society* | *Organi društva* MIDEM

MIDEM *Executive Board* | *Izvršilni odbor* MIDEM

President of the MIDEM Society | Predsednik društva MIDEM
Prof. Dr. Barbara Malič, Jožef Stefan Institute, Ljubljana, Slovenia

Vice-presidents | Podpredsednika
Prof. Dr. Janez Krč, UL, Faculty of Electrical Engineering, Ljubljana, Slovenia
Dr. Iztok Šorli, Mikroiks d.o.o., Ljubljana, Slovenia

Secretary | Tajnik
Olga Zakrajšek, UL, Faculty of Electrical Engineering, Ljubljana, Slovenia

MIDEM Executive Board Members | Člani izvršilnega odbora MIDEM
Prof. Dr. Slavko Bernik, Jožef Stefan Institute, Slovenia
Assoc. Prof. Dr. Miha Čekada, Jožef Stefan Institute, Ljubljana, Slovenia
Prof. DDr. Denis Đonlagić, UM, Faculty of Electrical Engineering and Computer Science, Maribor, Slovenia
Prof. Dr. Leszek J. Golonka, Technical University, Wroclaw, Poljska
Prof. Dr. Vera Gradišnik, Tehnički fakultet Sveučilišta u Rijeci, Rijeka, Croatia
Mag. Leopold Knez, Iskra TELA, d.d., Ljubljana, Slovenia
Mag. Mitja Koprivšek, ETI Elektroelementi, Izlake, Slovenia
Asst. Prof. Dr. Gregor Primc, Jožef Stefan Institute, Ljubljana, Slovenia
Prof. Dr. Janez Trontelj, UL, Faculty of Electrical Engineering, Ljubljana, Slovenia
Asst. Prof. Dr. Hana Uršič Nemevšek, Jožef Stefan Institute, Ljubljana, Slovenia
Dr. Danilo Vrtačnik, UL, Faculty of Electrical Engineering, Ljubljana, Slovenia

Supervisory Board | *Nadzorni odbor*

Prof. Dr. Franc Smole, retired
Prof. Dr. Drago Strle, UL, Faculty of Electrical Engineering, Ljubljana, Slovenia
Igor Pompe, retired

Court of honour | *Častno razsodišče*

Darko Belavič, retired
Dr. Miloš Komac, retired
Dr. Hana Uršič Nemevšek, Jožef Stefan Institute, Ljubljana, Slovenia

Informacije MIDEM
Journal of Microelectronics, Electronic Components and Materials
ISSN 0352-9045

Publisher / Založnik:
MIDEM Society / Društvo MIDEM
Society for Microelectronics, Electronic Components and Materials, Ljubljana, Slovenia
Strokovno društvo za mikroelektroniko, elektronske sestavne dele in materiale, Ljubljana, Slovenija

www.midem-drustvo.si